

April 2000  
111-2-1  
15133  
P.130

---

# Algorithm and Code Development for Unsteady Three-Dimensional Navier-Stokes Equations

---

Dr. Shigeru Obayashi

---

(NASA-CR-185039) ALGORITHM AND CODE  
DEVELOPMENT FOR UNSTEADY THREE-DIMENSIONAL  
NAVIER-STOKES EQUATIONS Annual Report, 1  
Apr. 1987 - 20 Mar. 1991 (MCAT Inst.)  
170 p.

N91-28503

Unclass

CSCL 200 63/54 001513

June 1991

NCC2-605

---

# **Algorithm and Code Development for Unsteady Three-Dimensional Navier-Stokes Equations**

---

Dr. Shigeru Obayashi

---

June 1991

NCC2-605

# Algorithm and Code Development for Unsteady Three-Dimensional Navier-Stokes Equations

Shigeru Obayashi

## Introduction

Research in aeroelasticity with computational methods, including the numerical prediction of flutter boundaries, requires a sophisticated algorithm and computer code to simulate unsteady flow phenomena in three dimensions. The purpose of this research is to develop an improved algorithm and computer code for solving the unsteady three-dimensional Euler and Navier-Stokes equations. These equations accurately describe the flow phenomena for aeroelastic applications.

An algorithm that uses central differencing has been used in the computer code, ENSAERO, for aeroelasticity at the NASA Ames Research Center. However, modern upwind algorithms can produce more accurate solutions for the Euler and Navier-Stokes equations. Among upwind algorithms, a streamwise upwind algorithm has recently been developed by Obayashi and Goorjian (see Appendix A). Most multidimensional upwind algorithms are first constructed in one dimension and then extended to multiple dimensions by applying the one-dimensional procedure in each coordinate direction. On the other hand, the present method follows the flow physics more closely than the coordinate upwind methods. The steady-state computations confirmed the higher resolution of the present algorithm over the central-difference method as well as over other upwind methods.

The objective of this research is to update Ames's aeroelasticity code, ENSAERO, by using the improved streamwise upwind algorithm. This report summarizes briefly the work performed during the period, April 1, 1989

through March 30, 1991. Additional details on the various aspects of the study are given in Appendices.

## Research Efforts

The following specific objectives have been performed:

- The algorithm was extended to handle the moving grid system. The finite-volume concept is essential to extend the algorithm. The resulting algorithm is conservative for any motion of the coordinate system.
- Two extensions to an implicit method were considered. The implicit extension that makes the algorithm computationally efficient is implemented into ENSAERO.
- The new flow solver has been validated through the solution of test problems. The test cases include three-dimensional problems with fixed and moving grids.
- Finally, the new flow solver has been implemented into NASA Ames's aeroelasticity code, ENSAERO.

## Results

In this work, only the first-order time-accurate methods are considered because of computational efficiency. However, time accuracy is an essential requirement for aeroelastic computations. Numerical schemes used for flow calculations in aeroelasticity must guarantee the correct calculation of amplitude and phase of unsteady pressures. In order to verify the time accuracy of the present code, unsteady flows over various wings undergoing prescribed oscillatory and ramp motions have been computed.

### F-5 Wing

The first test case shown here is an unsteady viscous flow over the F-5 wing which has an aspect ratio of 2.98, a taper ratio of 0.31 and a leading edge sweep angle of  $31.92^\circ$ . The test case is chosen at  $M_\infty = 0.9$ ,  $Re = 9 \times 10^6$

and the angle of attack of  $0^\circ$ . Since the airfoil section is supercritical, the flow is shock-free on the most of the wing surface at this flow condition. In the unsteady case, the wing is pitching with a pitch amplitude of  $0.11^\circ$  at a reduced frequency of 0.55 as illustrated in Fig. 1. The experimental data show that the shock wave appears on the wing surface due to the pitching motion. Figure 2 shows the comparison of the computed instantaneous pressure coefficient contours using the upwind and central-difference methods at  $\alpha = 0^\circ$  during pitch down motion. The upwind result shows the shock wave moving forward, which is captured within the two grid points here. In contrast, the central-difference result does not show any concentration of contours throughout the cycle. The result confirms that the upwind method predicts the shock motion more accurately than the central-difference method does.

## Clipped Delta Wing

The second test considers the motion of the leading-edge vortex as well as the motion of the shock wave. Figure 3 illustrate the planform of a clipped delta wing and a typical flow field to be computed. Since the leading edge is sharp and swept, a leading-edge vortex is formed at moderate angles of attack. A shock wave is also formed at transonic speeds. They interact with each other at certain flow conditions.

Figure 4 shows the comparisons of unsteady pressures between the computed and measured data at  $M_\infty = 0.9$ ,  $Re = 18 \times 10^6$ , the mean angle of attack of  $4^\circ$ , the pitch amplitude of  $0.5^\circ$  and the reduced frequency of 0.6. Two peaks in the  $C_p$  magnitude and the corresponding jumps in the phase angle are observed. The first peak near the leading edge is due to the motion of the leading-edge vortex and the second peak is due to the motion of the shock wave. The results indicate that the computation captures the main structure of the flow field with the modified Baldwin-Lomax turbulence model.

To check the aeroelastic option of the code, the flexibility of the wing is next considered. Figure 5 shows the first four mode shapes of the clipped delta wing. Figure 6 shows the pressure responses on the wing upper surface in the  $10^\circ$  ramp motion from 0 angle of attack at  $M_\infty = 0.9$ . At first, the leading-edge vortex and shock wave develop. At the inboard section, they remain without an interaction. At the outer sections, they have a strong

interaction, which leads to a vortex breakdown. Figure 7 shows stream line patterns before and after the breakdown. At 1500 time steps ( $t = 0.1 \text{ sec}$ ), the angle of attack reaches  $10^\circ$  and the wing is deformed in the nearly maximum displacement. Then, the breakdown proceeds from the wing tip to the middle of the wing span. At 2400 time steps ( $t = 0.16 \text{ sec}$ ), the wing is less deformed because of the reduction of the local lift due to the breakdown. The results successfully demonstrate the capability of the upwind version of ENSAERO.

For the aeroelastic case, the upwind computation requires  $19 \mu\text{sec}$  per grid point per time step at a speed of 160MFLOPS on a CRAY-YMP computer using a single processor, while the central-difference computation requires  $17 \mu\text{sec}$  at a speed of 150 MFLOPS.

## Concluding Remarks

In the present study, a streamwise upwind algorithm has been extended and validated for solving the unsteady three-dimensional Navier-Stokes equations. The resulting algorithm has been implemented into Ames's aeroelasticity code, ENSAERO. The upwind version leads to higher accuracy in both steady and unsteady computations than the previously used central-difference method does, while the increase in the computational time is small.

The future research plan is to continue the algorithm enhancements of ENSAERO and to apply the code to complicated geometries, such as a wing-body combination and a wing with a control surface. ENSAERO inherits the zonal grid capability developed for the Transonic Navier-Stokes code to handle complicated geometries, such as wing-body and complete aircraft configurations. The key development of the algorithm is integration of the upwind and zonal techniques. This includes an interface treatment between moving zones for a control surface. The other key development is an improvement in turbulence modelling. So far the Baldwin-Lomax model has been used. Applicability of more accurate models to unsteady transonic flows is to be investigated.

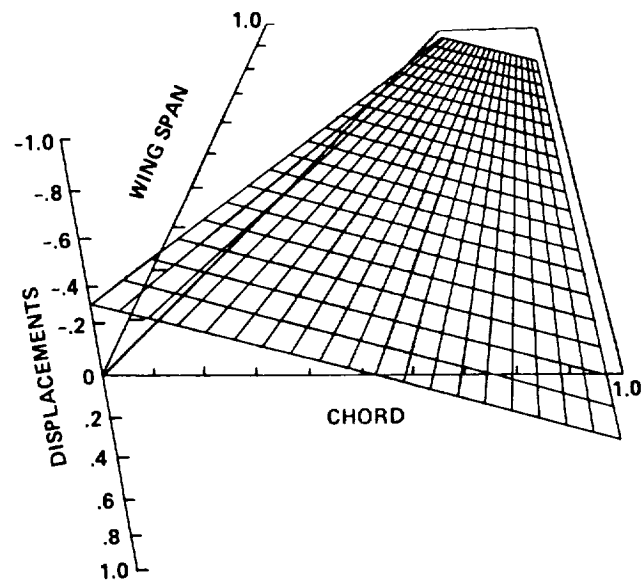
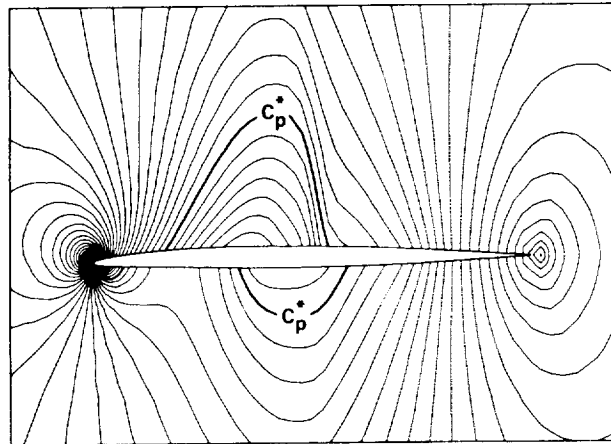
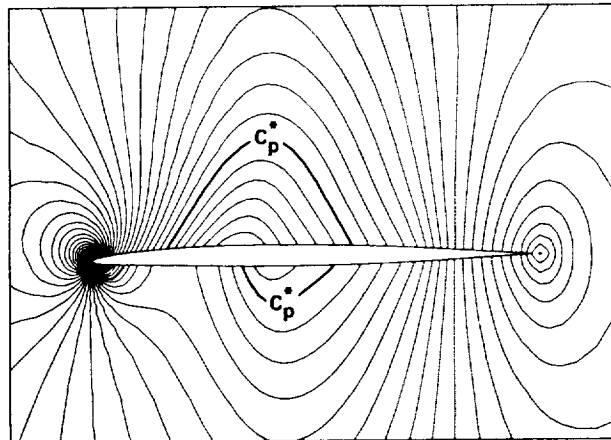


Fig. 1 Unsteady modal motion of F-5 wing.

F-5 wing  
 $M_\infty = 0.896$   
 $\alpha = 0^\circ$  (pitching down)  
 $k = 0.550$   
 $Re = 9 \times 10^6$   
 Grid:  $151 \times 25 \times 30$   
 70% semispan



a)



b)

Fig. 2 Comparison of computed instantaneous pressure contours between the upwind and central-difference methods. a) Upwind result, b) Central-difference result.



**Circular-arc airfoil**

**t/c = 0.06**

**L.E. sweep angle =  $50.4^\circ$**

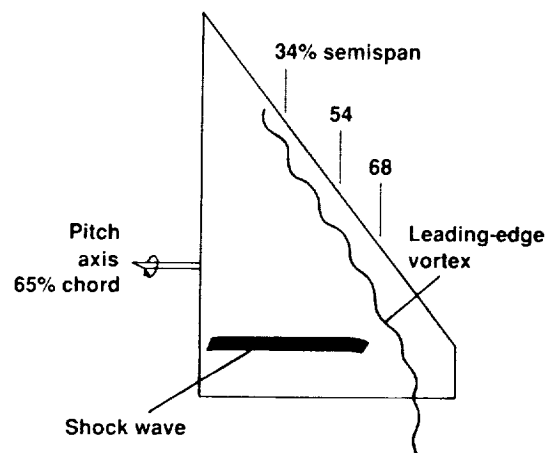
**Area =  $1635.88 \text{ in}^2$**

**Span = 45.08 in.**

**Root chord = 63.55 in.**

**Tip chord = 9.03 in.**

**Taper ratio = 0.1421**



Obayashi

**Fig. 3 Planform geometry of clipped delta wing and typical flow structure.**

**Clipped Delta Wing**

$M_\infty = 0.90$ ,  $Re = 18 \times 10^6$ ,  $\alpha_m = 4^\circ$

$\bar{\alpha} = 0.5^\circ$ ,  $k = 0.6$

— Modified  
 - - - Unmodified  
 □ Experiment,  
 NASA TP-2594

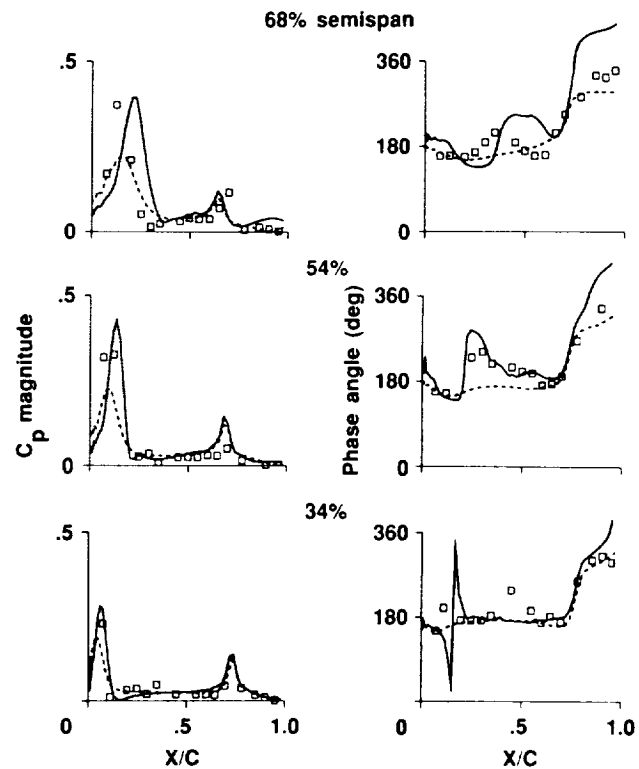
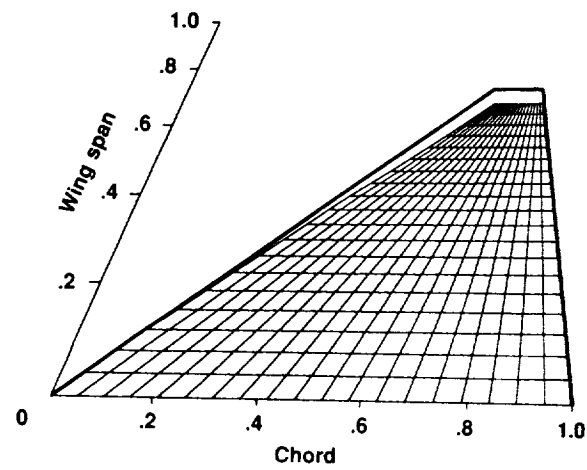
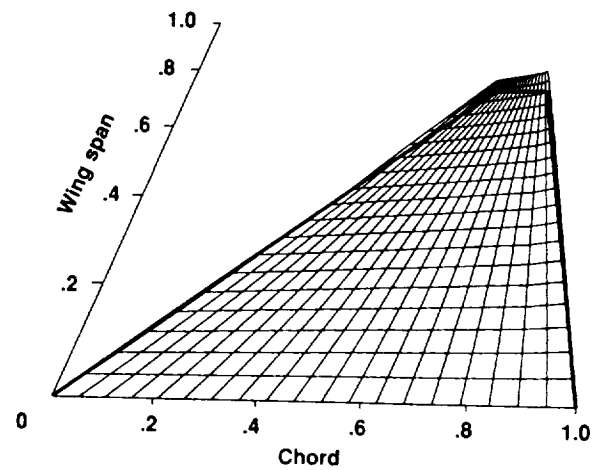


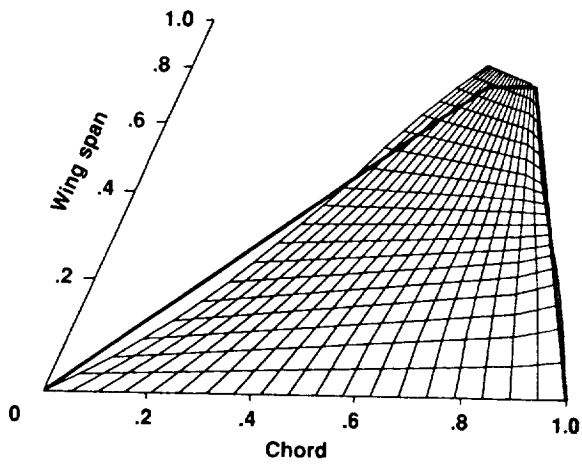
Fig. 4 Comparison of computed unsteady pressures using the standard and modified Baldwin-Lomax turbulence models with experiment,  $M_\infty = 0.90$ ,  $\alpha_m = 3.97$ ,  $\bar{\alpha} = 0.46$ ,  $Re_c = 17.6 \times 10^6$ ,  $k = 0.5919$ .



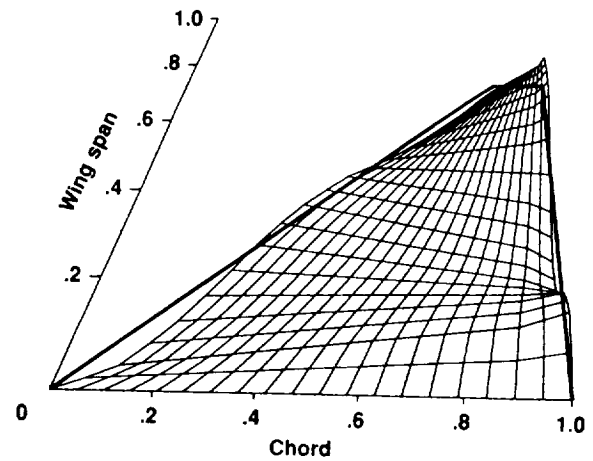
(a) Mode 1: Frequency = 6 Hz



(b) Mode 2: Frequency = 8 Hz



(c) Mode 3: Frequency = 18 Hz



(d) Mode 4: Frequency = 28 Hz

Fig. 5 First four mode shapes and frequencies of clipped delta wing.

Clipped Delta Wing (Flexible),  $M_\infty = 0.9$ ,  $Re = 15 \times 10^6$ ,  $A = 0.04$

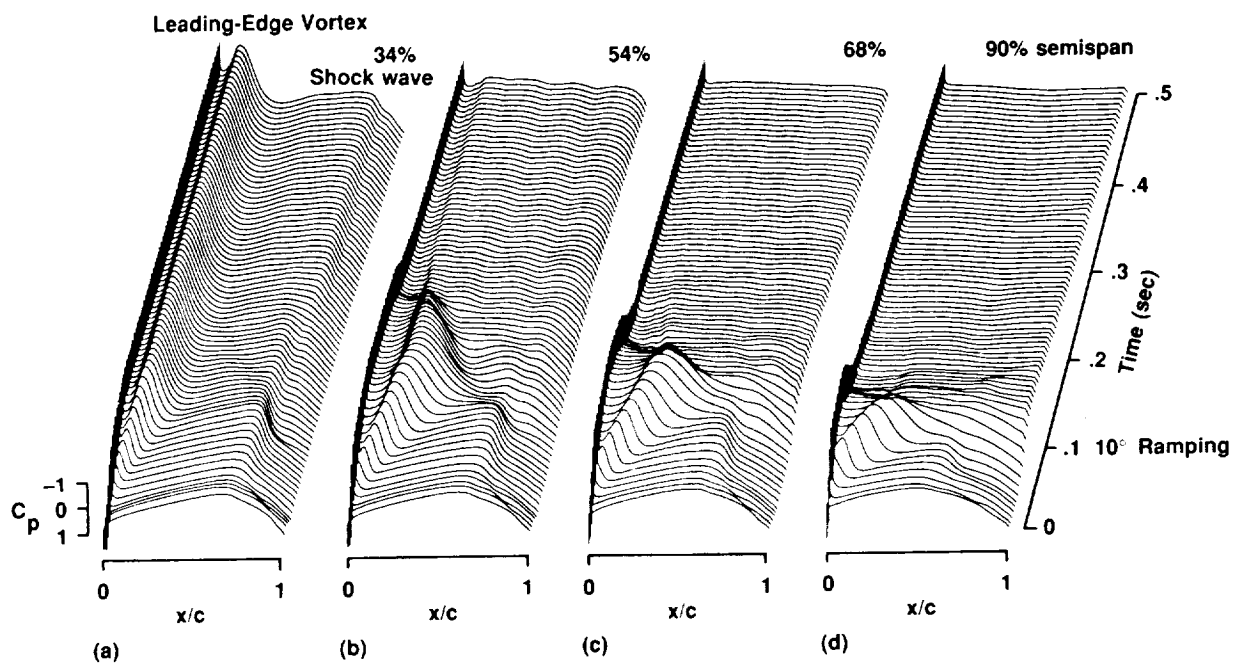


Fig. 6 Unsteady upper surface pressure responses of flexible wing,  $M_\infty = 0.90$ ,  $10^\circ$  ramping up,  $Re_c = 15.0 \times 10^6$ ,  $A = 0.04$ .

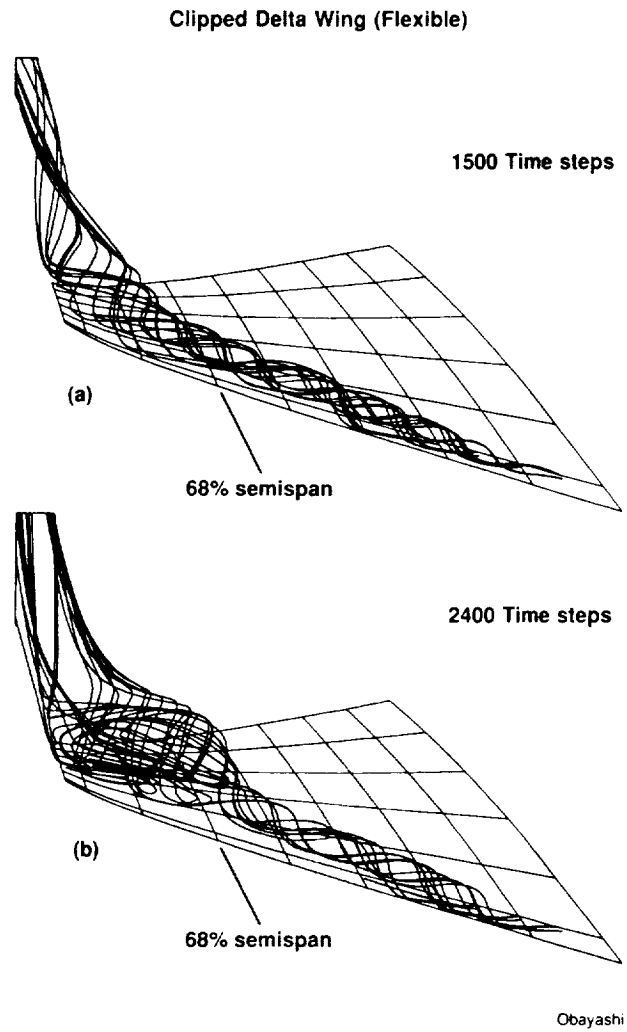


Fig. 7 Streamline pattern over the upper surface of flexible wing,  $M_\infty = 0.90$ ,  $10^\circ$  ramping up,  $Re_c = 15.0 \times 10^6$ ,  $A = 0.04$ . a) 1500 time steps; b) 2400 time steps.

# **APPENDIX A**



**AIAA-89-1957-CP**

**IMPROVEMENTS AND APPLICATIONS OF A  
STREAMWISE UPWIND ALGORITHM**

**S. Obayashi and P. M. Goorjian**

**NASA Ames Research Center**

**Moffett Field, CA**

**AIAA 9th Computational Fluid  
Dynamics Conference**

**Buffalo, New York / June 13-15, 1989**

as follows:

$$\partial_r \hat{Q} + \partial_\xi \hat{E} + \partial_\eta \hat{F} + \partial_\zeta \hat{G} = \frac{1}{Re} \partial_\zeta \hat{G}^v \quad (1)$$

The vector of conserved quantities  $\hat{Q}$  and the inviscid flux vector  $\hat{F}$  are

$$\hat{Q} = \frac{1}{J} \begin{bmatrix} \rho \\ \rho u \\ \rho v \\ \rho w \\ e \end{bmatrix}, \quad \hat{F} = \frac{1}{J} \begin{bmatrix} \rho \hat{U} \\ \rho u \hat{U} + \eta_x p \\ \rho v \hat{U} + \eta_y p \\ \rho w \hat{U} + \eta_z p \\ \rho h \hat{U} \end{bmatrix}$$

where  $h$  is the total enthalpy and the contravariant velocity component,  $\hat{U}$ , is defined as  $\hat{U} = \eta_x u + \eta_y v + \eta_z w$ . For the  $\xi$  and  $\zeta$  directions,  $\hat{E}$  and  $\hat{G}$  can be defined similarly. The viscous flux vector  $\hat{G}^v$  is given by

$$\hat{G}^v = \frac{1}{J} \begin{bmatrix} 0 \\ \mu m_1 u_\zeta + \frac{\mu}{3} m_2 \zeta_x \\ \mu m_1 v_\zeta + \frac{\mu}{3} m_2 \zeta_y \\ \mu m_1 w_\zeta + \frac{\mu}{3} m_2 \zeta_z \\ \mu m_1 m_3 + \frac{\mu}{3} m_2 (\zeta_x u + \zeta_y v + \zeta_z w) \end{bmatrix}$$

with

$$\begin{aligned} m_1 &= \zeta_x^2 + \zeta_y^2 + \zeta_z^2 \\ m_2 &= \zeta_x u_\zeta + \zeta_y v_\zeta + \zeta_z w_\zeta \\ m_3 &= \frac{1}{2}(u^2 + v^2 + w^2)_\zeta + \frac{1}{Pr(\gamma - 1)}(c^2)_\zeta \end{aligned}$$

where  $Re$  is the Reynolds number,  $Pr$  is the Prandtl number,  $c$  is the speed of sound, and  $J$  is the transformation Jacobian. Pressure is related to the conservative flow variables,  $\hat{Q}$ , through the equation of state for a perfect gas:

$$p = (\gamma - 1) \left\{ e - \frac{\rho}{2}(u^2 + v^2 + w^2) \right\} \quad (2)$$

where  $\rho$  is the fluid density and  $e$  is total energy per unit of volume of the fluid.

Assuming conical symmetry, Eq. (1) can be rewritten as

$$\partial_r \hat{Q} + \partial_\eta \hat{F} + \partial_\zeta \hat{G} = -2\hat{E} + \frac{1}{Re} \partial_\zeta \hat{G}^v \quad (3)$$

where  $\xi$  is the conical direction and  $(\eta, \zeta)$  are the generalized coordinates on the conical surface. The conical transformation can be described as<sup>9</sup>  $\xi = x\lambda$ ,  $\eta = \eta(Y, Z)$ ,  $\zeta = \zeta(Y, Z)$  where  $\lambda = (1 + Y^2 + Z^2)^{1/2}$ ,  $Y = y/x$ ,  $Z = z/x$ . The metrics are expressed as

$$\begin{aligned} \xi_x &= \frac{1}{\lambda}, \quad \xi_y = \frac{Y}{\lambda}, \quad \xi_z = \frac{Z}{\lambda} \\ \eta_x &= -\lambda(Y\hat{\eta}_Y + Z\hat{\eta}_Z), \quad \eta_y = \lambda\hat{\eta}_Y, \quad \eta_z = \lambda\hat{\eta}_Z \\ \zeta_x &= -\lambda(Y\hat{\zeta}_Y + Z\hat{\zeta}_Z), \quad \zeta_y = \lambda\hat{\zeta}_Y, \quad \zeta_z = \lambda\hat{\zeta}_Z \\ J &= \lambda^3 \hat{J} \end{aligned} \quad (4)$$

where  $\hat{\eta}_Y$ ,  $\hat{\zeta}_Y$ , and so on, are the two-dimensional metrics on the conical surface  $(Y, Z)$ .

## Numerical Algorithm

### FVS and FDS Algorithm

The space-discretized form of Eq. (3) can be written as

$$\partial_r \hat{Q} + \frac{\hat{F}_{j+\frac{1}{2}} - \hat{F}_{j-\frac{1}{2}}}{\Delta \eta} + \frac{\hat{G}_{k+\frac{1}{2}} - \hat{G}_{k-\frac{1}{2}}}{\Delta \zeta} = -2\hat{E}_i + \frac{1}{Re} \frac{\hat{G}_{k+\frac{1}{2}}^v - \hat{G}_{k-\frac{1}{2}}^v}{\Delta \zeta} \quad (5)$$

where a second-order central-difference evaluation is applied to the viscous term. Now the streamwise upwind algorithm is described for the inviscid fluxes at cell interfaces.

For subsonic flows, Goorjian's FVS algorithm<sup>4</sup> can be written as

$$\hat{F}(Q_l, Q_r, S_{j+\frac{1}{2}}) = \frac{1}{2} \frac{|\nabla \eta|}{J} \left\{ F_r + F_l - \int_{Q_l}^{Q_r} \frac{\partial^* F}{\partial Q} dQ \right\} \quad (6)$$

where  $Q_l$  and  $Q_r$  are left and right states, respectively, and the metric terms,  $\eta_x, \eta_y$  and  $\eta_z$ , are normalized by  $|\nabla \eta|$  as  $k_x = \frac{\eta_x}{|\nabla \eta|}$ , and so on. The contravariant velocity is also normalized by  $|\nabla \eta|$ , and used as  $U = k_x u + k_y v + k_z w$  in the following. For the first-order-accurate computations,  $l = j$  and  $r = j + 1$ . For higher-order extensions, the MUSCL approach<sup>3,8</sup> is used.

The integral part was derived as follows for  $U \geq 0$ :

$$\int_{Q_l}^{Q_r} \frac{\partial^* F}{\partial Q} dQ = \{ F + \Delta^* F \}_r - \{ F + \Delta^* F \}_l \quad (7)$$

where  $*$  indicates local sonic values<sup>4</sup> and  $\Delta^* F = F^* - F$ . Using the local isentropic relations,  $\Delta^* F$  can be simplified in the one-dimensional case:  $\Delta^* F = \Delta^*(\rho u) e_s$ , where  $e_s = (1, u, h)^T$  is a sum of two eigenvectors of  $\Delta^* F / \Delta^* Q$ . Note  $\Delta^*(\rho u) > 0$  for  $M < 1$  and  $\Delta^*(\rho u) = 0$  for  $M = 1$ . This formula is equivalent to the FDS formula, if the flow is isentropic. If not, it is an FVS algorithm. Even in the latter case, the use of isentropic relations does not restrict the flow fields because the isentropic relation is used only locally at each grid point (or cell) to compute local sonic values in space and time. This formula can be directly extended to the three-dimensional case because of the rotated differencing along the streamwise direction:

$$\Delta^* F = \Delta^*(\rho q) e_s \quad (8)$$

with

$$(q^*)^2 = \frac{2}{\gamma + 1} (c^2 + \frac{\gamma - 1}{2} q^2)$$

$$\rho^* = \rho \left( \frac{(q^*)^2}{c^2} \right)^{\frac{1}{\gamma - 1}}$$



$$f_{l,r}^{\pm} = (\rho U)_{l,r} \{1 \pm \text{sign}(U_{l,r}) \cos^2 \theta_{l,r}\} \\ \pm s_{l,r} \Delta^* (\rho q)_{l,r} \cos^2 \theta_{l,r} \pm \rho_{l,r} |U_m| \sin^2 \theta - \Delta_1 \sin^2 \theta \\ p_{l,r}^{\pm} = p_{l,r} \{1 \pm \text{sign}(U_{l,r}) \cos^2 \theta_{l,r}\} - \Delta_2 \sin^2 \theta$$

and where  $\Delta_1 = (c_m - |U_m|) \frac{\Delta p}{2c_m^2}$  and  $\Delta_2 = (c_m - |U_m|) \frac{\rho_m \Delta U}{2}$ . The evaluation of  $f_{l,r}^{\pm}$  requires many operations, but this is not excessively expensive in computations because it is a scalar quantity.

### CD Method

To compare with the upwind formulations, the second-order-accurate CD method with the artificial dissipation terms<sup>8</sup> is shown here as

$$\hat{F}(Q_j, Q_{j+1}, S_{j+\frac{1}{2}}) = \frac{1}{2} \{ \hat{F}(Q_j, S_j) + \hat{F}(Q_{j+1}, S_{j+1}) \} \\ - \kappa \left( \frac{\sigma}{J} \right)_{j+\frac{1}{2}} \left\{ \alpha_{j+\frac{1}{2}} (Q_{j+1} - Q_j) - \frac{\delta^2 Q_{j+1} - \delta^2 Q_j}{1 + \alpha_{j+1} + \alpha_j} \right\} \quad (17)$$

where  $\kappa = 0.05$  in the present study,  $\delta^2$  is a central second-difference,  $\sigma$  is a spectral radius of the Jacobian matrix,  $A$ , and  $( )_{j+\frac{1}{2}} = \{ ( )_{j+1} + ( )_j \} / 2$ . The parameter  $\alpha$  controls the strength of the second-order dissipation:

$$\alpha_j = \left( \frac{3 + 2M_{\infty}^2}{4} \right) \left( \frac{p_{j+1} - 2p_j + p_{j-1}}{p_{j+1} + 2p_j + p_{j-1}} \right). \quad (18)$$

Note that this model uses the difference of the conservative variables directly, while the present upwind formula uses the combination of differences, such as total mass flux, pressure, and contravariant velocity.

### Results

Assuming conical flow, the computations become two-dimensional. Computations for conical flows are carried out in the following manner. The LU-ADI method,<sup>12</sup> which can be modified for the conical flow fields,<sup>9</sup> is used for three upwind algorithms and the CD method, which are computed explicitly. Laminar flow is also assumed. The third-order MUSCL scheme with Koren's differentiable limiter<sup>8</sup> is used for the two-dimensional computations.

#### 10° Cone at Zero Incidence

The first test case is the computation of flow past a 10° cone at zero incidence.<sup>2</sup> For a circular cone at zero incidence, the solutions become one-dimensional, varying only with the angle between conical ray and cone surface.

Figure 1 shows a comparison of numerical solutions on 37 grid points. The numerical fluxes are evaluated by three first-order-accurate upwind algorithms, i.e., the present formula (indicated as Goorjian-Obayashi), Roe's FDS and Steger-Warming's FVS formulas, and the CD method. The results indicate that the present formula resolves shocks and shear layers accurately in the manner of Roe's formula which has a perfect resolution in the one-dimensional case. The

CD method works fairly well for capturing the boundary layer. Steger-Warming's solution appears most dissipative, as pointed out in Ref. 2.

#### 75° Delta Wing

The second test case considers a vortical flow field in order to examine the present formula's capability for computing shear flows. Computations are done for flows past a 75° delta wing at  $M_{\infty} = 2.8$  and  $\alpha = 16^\circ$ , for which experimental data are available.<sup>13</sup> Figure 2 shows the model geometry, and the typical experimental flow field is shown in Fig. 3. For the computations, the conical assumption is used.<sup>14</sup> Three grids are used for a grid-refinement study. The coarse, medium, and fine grids use 27 (circumferential)  $\times$  51 (normal to body), 51  $\times$  51 and 99  $\times$  51 points, respectively, as shown in Fig. 4, where  $(y, z)$  corresponds to the physical coordinates, not to the conical coordinates  $(Y, Z)$ . The vertical solid lines near  $y = 0.1$  and  $0.2$  in Fig. 4 indicate the locations of the following comparisons in Figs. 7 and 8.

Computations were done with the present method, Roe's, and the CD methods. Figure 5 shows a comparison of density contour plots of three numerical solutions on the fine grids. Two shock waves can be observed. One is the bow shock wave in the windward side of the delta wing, and the other is the crossflow shock wave in the leeward side. The present and Roe's methods give similar contour plots for those shock waves, but the CD method gives smeared plots. (For the CD method, the smoothing coefficient,  $\kappa$ , was set to 0.1 in the fine-grid case instead of  $\kappa = 0.05$  in the other cases because at convergence the solution had numerical oscillations with  $\kappa = 0.05$  in the fine grid.) The low density regions at both the primary and secondary vortices also indicate that both upwind methods give similar solutions, but the CD method gives a smeared one.

A comparison of total pressure contour plots on the fine grids is shown in Fig. 6. The primary vortex appears similarly in both upwind solutions, in respect to its location and the contour level, but not in the CD solution. The primary vortex appears off from the boundary layer in both upwind solutions. But the primary vortex and the boundary layer touch each other in the CD solution. The shear-flow region separated from the leading edge also shows differences in the three solutions. The present formula gives a sharper solution than Roe's in this shear-flow region. The CD solution gives the most dissipative solution, again. To confirm these observations, solution profiles are compared at  $y = 0.1$  (approximately on the primary vortex) and  $y = 0.2$  (approximately on the secondary vortex) as indicated in Fig. 4.

Figure 7 shows comparisons of total pressure profiles at  $y = 0.1$  on the coarse, medium, and fine grids. The large gradient near  $z = 0$  corresponds to the boundary layer. In the coarse grid case, the CD solution does not have a high peak as the other upwind solutions does. This peak becomes higher and thus closer to the upwind solutions as the grids are refined. The local minimum near  $z = 0.05$  corresponds to the primary vortex. The CD method also gives a smeared profile. In Fig. 7c, the profile of the CD solution varies continuously to the primary vortex. Compared with the CD solution, both upwind solutions have a sharper gradient region, which confirms the observation in Fig. 6. Roe's solutions agree with the present solutions on the medium and fine grids but not on the coarse grid. Although not shown in this paper, plots of helicity density show that Roe's solution

- <sup>3</sup> Vatsa, V.N., Thomas, J.L. and Wedan, B.W., "Navier-Stokes Computations of Prolate Spheroids at Angle of Attack," AIAA Paper 87-2627-CP, Aug. 1987.
- <sup>4</sup> Goorjian, P.M., "Algorithm Development for the Euler Equations with Calculations of Transonic Flows," AIAA Paper 87-0536, Jan. 1987.
- <sup>5</sup> Goorjian, P.M., "A New Algorithm for the Navier-Stokes Equations Applied to Transonic Flows Over Wing," AIAA Paper 87-1121-CP, AIAA 8th Computational Fluid Dynamics Conference, Honolulu, Hawaii, June 1987.
- <sup>6</sup> Steger, J.L. and Warming, R.F., "Flux Vector Splitting of the Inviscid Gasdynamic Equations with Application to Finite-Difference Methods," *Journal of Computational Physics*, Vol. 40, 1981, pp. 263-293.
- <sup>7</sup> Goorjian, P.M., "A Streamwise Upwind Algorithm for the Euler and Navier-Stokes Equations Applied to Transonic Flows," *Numerical Methods for Fluid Dynamics III*, edited by K. W. Morton and Baines, The Institute of Mathematics and Its Applications Conference Series, New Series No. 17, Clarendon Press, Oxford, 1988. Also NASA TM 101019, Aug. 1988.
- <sup>8</sup> Obayashi, S. and Gavali, S., "Three-Dimensional Simulation of Underexpanded Plumes Using Upwind Algorithms," Supercomputing '88, Kissimmee, Florida, Nov. 1988. Proceedings will be published by IEEE.
- <sup>9</sup> Fujii, K. and Obayashi, S., "Evaluation of Euler and Navier-Stokes Solutions for Leading-Edge and Shock-Induced Separations," AIAA Paper 85-1563, June 1985.
- <sup>10</sup> Liu, Y. and Vinokur, M., "Upwind Algorithms for General Thermo-Chemical Nonequilibrium Flows," AIAA Paper 89-0201, Jan. 1989.
- <sup>11</sup> Goorjian, P.M. and Obayashi S., NASA TM to be published.
- <sup>12</sup> Obayashi, S., "Numerical Simulation of Underexpanded Plumes Using Upwind Algorithms," AIAA Paper 88-4360-CP, Aug. 1988.
- <sup>13</sup> Miller, D.S. and Wood, R.M., "Lee-Side Flow Over Delta Wings at Supersonic Speeds," NASA TP-2430, June 1985.
- <sup>14</sup> McMillin, S.N., Thomas, J.L. and Murman, E.M., "Euler and Navier-Stokes Solutions for the Leaside Flow Over Delta Wings at Supersonic Speeds," AIAA Paper 87-2270-CP, Aug. 1987.

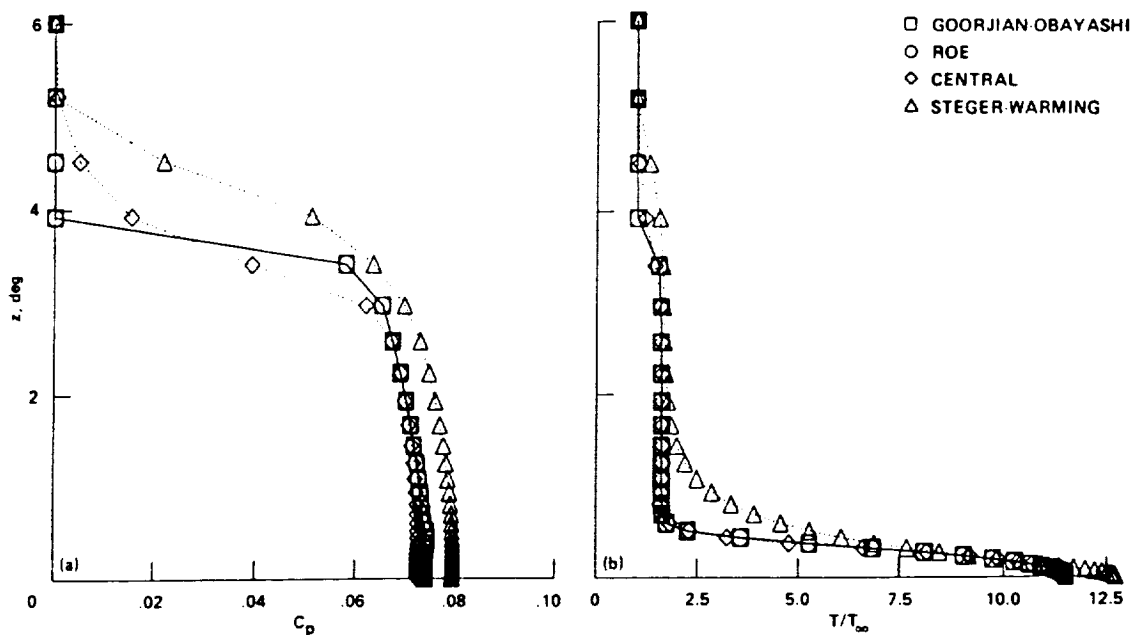


Fig. 1 Comparison of axisymmetric solutions over  $10^\circ$  cone;  $M_\infty = 7.95$ ,  $Re = 0.42 \times 10^6$ ,  $Pr = 0.72$ . a)  $C_p$  distributions; b)  $T/T_\infty$  distributions.

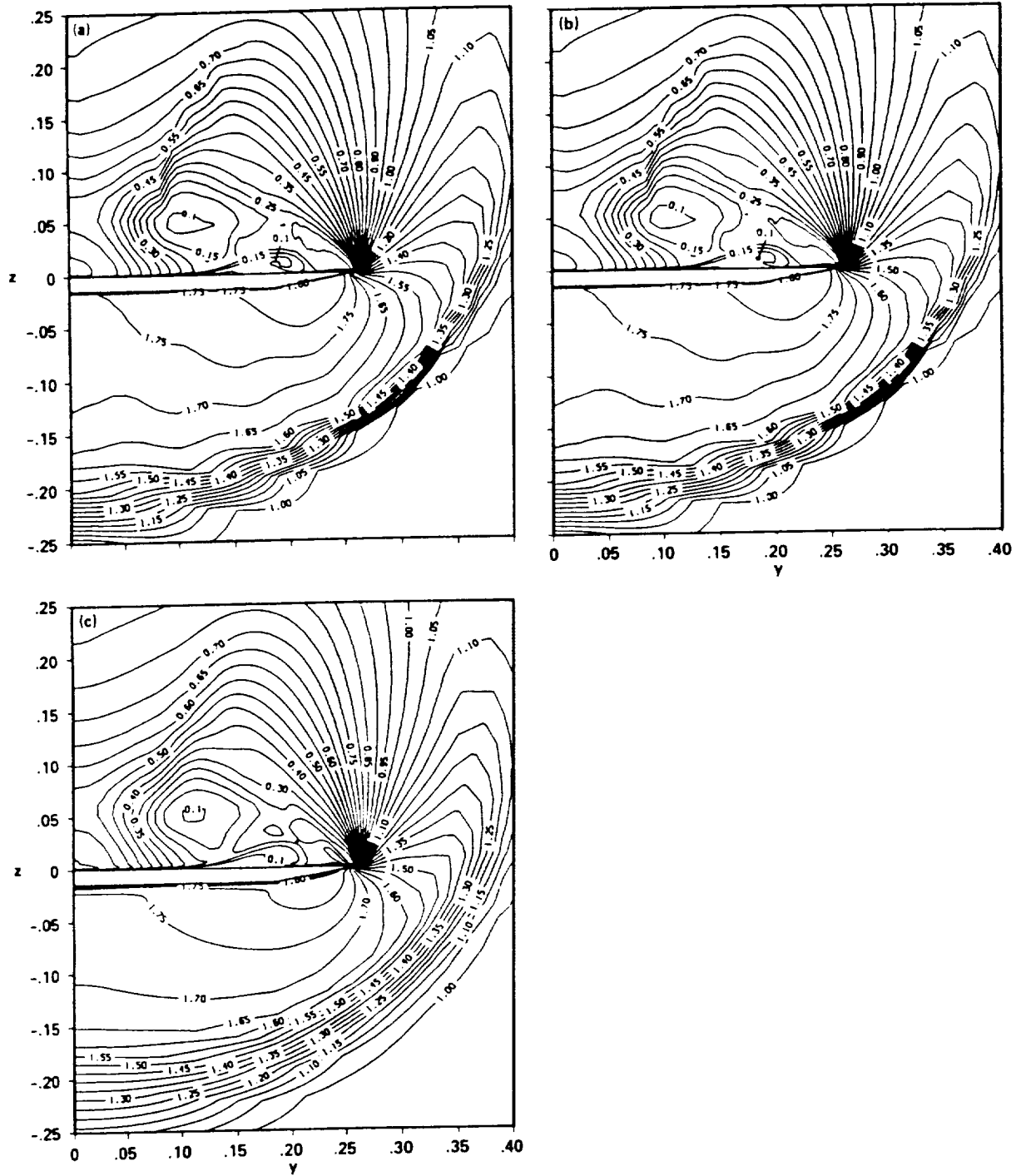


Fig. 5 Comparison of density contour plots on the fine grid;  $M_\infty = 2.8$ ,  $Re = 3.565 \times 10^6$ ,  $\alpha = 16^\circ$ . a) the present formula; b) Roe's formula; c) the central-difference method.

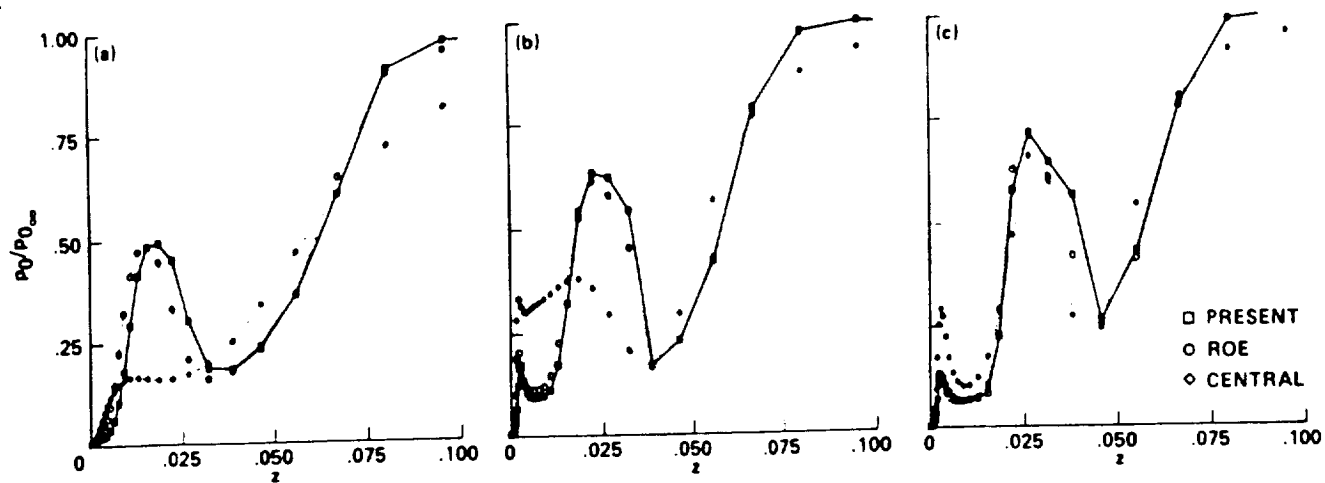


Fig. 8 Comparisons of total pressure profiles at  $y = 0.2$ . a) coarse grid; b) medium grid; c) fine grid.

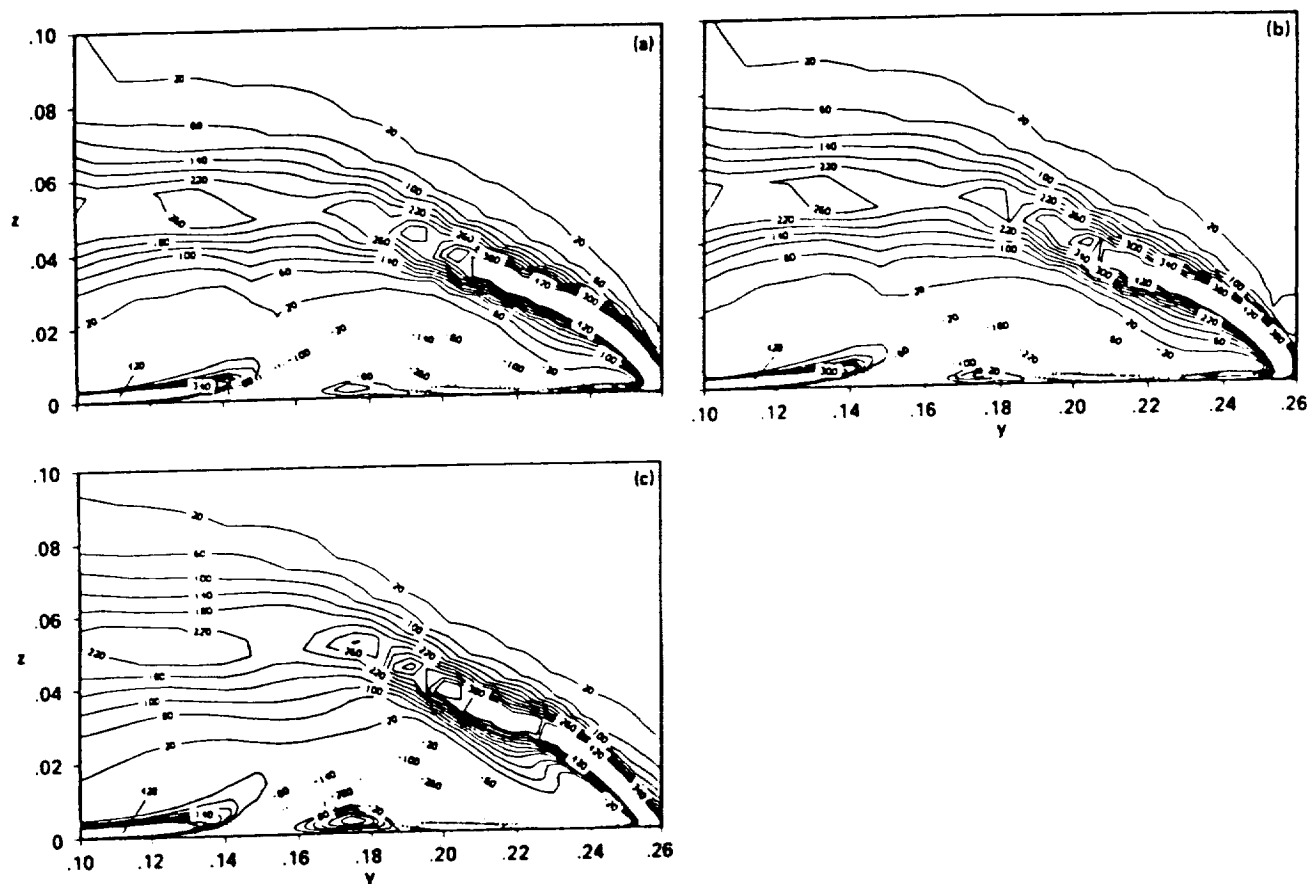


Fig. 9 Comparison of helicity density contour plots on the fine grid;  $M_\infty = 2.8$ ,  $Re = 3.565 \times 10^6$ ,  $\alpha = 16^\circ$ . a) the present formula; b) Roe's formula; c) the central-difference method.

# **APPENDIX B**

---

# **Extension of a Streamwise Upwind Algorithm to a Moving Grid System**

---

Shigeru Obayashi, Peter M. Goorjian, and  
Guru P. Guruswamy

---

April 1990

---

# Extension of a Streamwise Upwind Algorithm to a Moving Grid System

---

Shigeru Obayashi  
MCAT Institute, San Jose, California

Peter M. Goorjian and Guru P. Guruswamy  
Ames Research Center, Moffett Field, California

April 1990



National Aeronautics and  
Space Administration

**Ames Research Center**  
Moffett Field, California 94035-1000

# **EXTENSION OF A STREAMWISE UPWIND ALGORITHM TO A MOVING GRID SYSTEM**

Shigeru Obayashi,\* Peter M. Goorjian, and Guru P. Guruswamy  
Ames Research Center

## **SUMMARY**

A new streamwise upwind algorithm has been derived to compute unsteady flow fields with the use of a moving-grid system. The temporally nonconservative LU-ADI (lower-upper-factored, alternating-direction-implicit) method has been applied for time-marching computations. A comparison of the temporally nonconservative method with a time-conservative implicit upwind method indicates that the solutions are insensitive to the conservative properties of the implicit solvers when practical time-steps are used. Using this new method, computations have been made for an oscillating wing at a transonic Mach number. The computed results confirm that the present upwind scheme captures the shock motion better than the central-difference scheme based on the Beam-Warming algorithm. The new upwind option of the code allows larger time-steps and thus is more efficient, even though it requires slightly more computational time per time-step than the central-difference option.

## **INTRODUCTION**

A code, ENSAERO, is being developed at Ames using the Euler/Navier-Stokes equations for computing the unsteady aerodynamics and aeroelasticity of aircraft. The capability of the code has been demonstrated by computing vortical and transonic flows over flexible swept wings (refs. 1 and 2). The flow fields were calculated by a time-accurate, finite-difference scheme based on central differencing.

The purpose of this study is to enhance the algorithm capability of the present code. In this respect, the use of a new upwind scheme in comparison to the current central-difference (CD) scheme is investigated. The CD scheme requires an artificial dissipation to stabilize computations. Such artificial-dissipation models lead to more dissipative solutions than upwind schemes. In addition, the CD scheme is sensitive to the amount of dissipation and needs a specific dissipation coefficient for each case. On the other hand, upwind schemes do not require that any coefficient be specified.

Recently, a streamwise upwind algorithm has been developed and applied to treat steady-state problems of transonic flows over wings (ref. 3) and vortical flows over a delta wing (ref. 4) on fixed grids. The main feature of the streamwise method is the use of the local stream direction, flow velocity, and pressure gradient. The switching of flux evaluations always takes place at sonic values, where shock waves may exist. Therefore, this method follows the flow physics more closely than conventional upwind methods based

---

\* MCAT Institute, San Jose, California.



The Cartesian velocity components  $u$ ,  $v$ , and  $w$  are nondimensionalized by the free-stream speed of sound  $c_\infty$ ; the density  $\rho$  is nondimensionalized by the free-stream density  $\rho_\infty$ ; and the total energy per unit volume  $e$  is nondimensionalized by  $\rho_\infty c_\infty^2$ . The viscous flux vector  $\hat{G}^v$  is given by

$$\hat{G}^v = \frac{1}{J} \begin{bmatrix} 0 \\ \mu m_1 u_\zeta + \frac{\mu}{3} m_2 \zeta_x \\ \mu m_1 v_\zeta + \frac{\mu}{3} m_2 \zeta_y \\ \mu m_1 w_\zeta + \frac{\mu}{3} m_2 \zeta_z \\ \mu m_1 m_3 + \frac{\mu}{3} m_2 (\zeta_x u + \zeta_y v + \zeta_z w) \end{bmatrix}$$

with

$$\begin{aligned} m_1 &= \zeta_x^2 + \zeta_y^2 + \zeta_z^2 \\ m_2 &= \zeta_x u_\zeta + \zeta_y v_\zeta + \zeta_z w_\zeta \\ m_3 &= \frac{1}{2}(u^2 + v^2 + w^2)_\zeta + \frac{1}{Pr(\gamma - 1)}(c^2)_\zeta \end{aligned}$$

where  $Re$  is the Reynolds number,  $Pr$  is the Prandtl number,  $c$  is the speed of sound, and  $J$  is the transformation Jacobian. Pressure is related to the conservative flow variables  $\hat{Q}$ , through the equation of state for a perfect gas:

$$p = (\gamma - 1) \left[ e - \frac{\rho}{2}(u^2 + v^2 + w^2) \right] \quad (2)$$

where  $\rho$  is the fluid density and  $e$  is total energy per unit of volume of the fluid.

For the inviscid case, the viscous flux  $\hat{G}^v$  is replaced by 0. For the viscous case, the viscosity coefficient  $\mu$  in  $\hat{G}^v$  is computed as the sum of  $\mu_l + \mu_t$  where the laminar viscosity  $\mu_l$  is taken from the free-stream laminar viscosity, assumed to be constant for transonic flows, and the turbulent viscosity  $\mu_t$  is evaluated by the Baldwin-Lomax model.<sup>5</sup>

## NUMERICAL ALGORITHM

The space-discretized form of equation (1) can be written as

$$\partial_\tau \hat{Q} = -\frac{\hat{E}_{i+\frac{1}{2}} - \hat{E}_{i-\frac{1}{2}}}{\Delta \xi} - \frac{\hat{F}_{j+\frac{1}{2}} - \hat{F}_{j-\frac{1}{2}}}{\Delta \eta} - \frac{\hat{G}_{k+\frac{1}{2}} - \hat{G}_{k-\frac{1}{2}}}{\Delta \zeta} + \frac{1}{Re} \frac{\hat{G}_{k+\frac{1}{2}}^v - \hat{G}_{k-\frac{1}{2}}^v}{\Delta \zeta} \quad (3)$$

where a second-order central-difference evaluation is applied to the viscous term.

The evaluation of the inviscid fluxes is based on the finite-volume cell-centered scheme. To be consistent with the finite-difference scheme in ENSAERO, the metrics are defined at each grid point where the flow variables are stored. The surface vector of cell-interface, which is necessary for the finite-volume formulation, can be obtained by averaging the metrics at the adjoining points. The free-stream preservation of this metric evaluation was shown in reference 6.

Equation (4) is written in a vector form. If the formula is rewritten in component form, the present algorithm can be summarized with a surface vector  $\mathbf{S}$  and a motion of its centroid,  $\mathbf{x}_t = (x_t, y_t, z_t)$ , as

$$\hat{F}(Q_l, Q_r, \mathbf{S}_{j+\frac{1}{2}}, \mathbf{x}_{tj+\frac{1}{2}}) = \frac{1}{2} \frac{|\nabla \eta|}{J} \{ F_l^+ + F_r^- \} \quad (5)$$

where

$$F_{l,r}^\pm = \begin{bmatrix} f_{l,r}^\pm \\ f_{l,r}^\pm u_{l,r} + k_x p_{l,r}^\pm \\ f_{l,r}^\pm v_{l,r} + k_y p_{l,r}^\pm \\ f_{l,r}^\pm w_{l,r} + k_z p_{l,r}^\pm \\ f_{l,r}^\pm H_{l,r} - k_t p_{l,r}^\pm + (|\tilde{V}_m| \Delta p - \tilde{V}_m \Delta_2) \sin^2 \theta \end{bmatrix}$$

$$\begin{aligned} f_{l,r}^\pm &= (\rho \tilde{V})_{l,r} [1 \pm \text{sign}(\tilde{V}_{l,r}) \cos^2 \theta_{l,r}] \\ &\quad \pm s_{l,r} \Delta^*(\rho \tilde{q})_{l,r} \cos^2 \theta_{l,r} \pm \rho_{l,r} |\tilde{V}_m| \sin^2 \theta - \frac{1}{2} \Delta_1 \sin^2 \theta \\ p_{l,r}^\pm &= p_{l,r} [1 \pm \text{sign}(\tilde{V}_{l,r}) \cos^2 \theta_{l,r}] - \frac{1}{2} \Delta_2 \sin^2 \theta \end{aligned}$$

where  $\tilde{q}$  and  $\tilde{V}$  are defined above, and where  $\Delta_1 = (c_m - |\tilde{V}_m|) \frac{\Delta p}{c_m^2}$ ,  $\Delta_2 = (c_m - |\tilde{V}_m|) \rho_m \Delta V$ , and  $k_t = -k_x x_t - k_y y_t - k_z z_t$ . The averaged state ( $m$ ) is defined for  $\rho$ ,  $u$ ,  $v$ ,  $w$ , and  $H$  by the arithmetic average of the left ( $l$ ) and right ( $r$ ) states.

The switches  $s_l$  and  $s_r$  are defined in the manner of Godunov's method as follows. For  $\tilde{V} \geq 0$ ,

$$\begin{aligned} s_l &= 1 - \epsilon_l \epsilon_m \\ s_r &= (1 - \epsilon_m)(1 - \epsilon_r) \end{aligned} \quad (6)$$

where

$$\epsilon_{l,m,r} = \frac{1}{2} [1 + \text{sign}(M_{l,m,r}^2 - 1)]$$

and  $M = \tilde{q}/c$ .

A simple way to evaluate the rotation angle is to use  $\cos \theta = \tilde{V}/\tilde{q}$ . In supersonic flow fields, however, it is important to detect whether the velocity projected to the grid line is beyond the Mach cone. Thus,  $\tilde{V}/\tilde{q}$  is replaced by  $M \cdot \tilde{V}/\tilde{q} = \tilde{V}/c$ . If  $\tilde{V}/c$  becomes larger than one,  $\cos \theta$  is set to one. To avoid expansion shocks, the rotation angle is determined by a mixture of averaged ( $m$ ) and pointwise ( $l, r$ ) values:

$$\cos^2 \theta_{l,r} = \min \left[ (1 - \phi) \frac{\tilde{V}_m^2}{c_m^2} + \phi \frac{\tilde{V}_{l,r}^2}{c_{l,r}^2}, 1 \right] \quad (7)$$

## Approximate Block ADI Method

The LU-ADI method described in the previous section is nonconservative in time owing to the diagonalization. To investigate the significance of this temporal nonconservativeness, an alternative approach is considered here. A time-conservative method can be constructed using a block-tridiagonal solver similar to the Beam-Warming method. Since true Jacobians of the numerical fluxes of the present upwind algorithm are expensive to compute, approximate Jacobians are used here.

To construct an implicit method for the present upwind algorithm, it is easier to start from the vector form (eq. (4)) rather than from the component form (eq. (5)). From equation (4), the first-order-accurate flux can be rewritten as

$$\begin{aligned}\hat{F}_j^\pm = & \frac{1}{2} \frac{|\nabla \eta|_{j\pm\frac{1}{2}}}{J_{j\pm\frac{1}{2}}} \left\{ F_j [1 \pm \text{sign}(\tilde{V}_j) \cos^2 \theta_j] \pm s_j \Delta^*(\rho \tilde{q})_j \cos^2 \theta_j \mathbf{e}_{sj} \right. \\ & \pm |\tilde{V}_{j\pm\frac{1}{2}}| \sin^2 \theta Q_j \pm \frac{c_{j\pm\frac{1}{2}} - |\tilde{V}_{j\pm\frac{1}{2}}|}{c_{j\pm\frac{1}{2}}^2} \sin^2 \theta \mathbf{e}_{sj\pm\frac{1}{2}} p_j \\ & \left. \pm \rho_{j\pm\frac{1}{2}} (c_{j\pm\frac{1}{2}} - |\tilde{V}_{j\pm\frac{1}{2}}|) \sin^2 \theta \mathbf{e}_{dj\pm\frac{1}{2}} V_j \right\}\end{aligned}\quad (13)$$

To simplify the formula further, the  $\mathbf{e}_{sj\pm\frac{1}{2}}$  term in the second line of the above formula is replaced by  $\mathbf{e}_{sj}$ . Then, the Jacobian  $\partial \hat{F}^\pm / \partial \hat{Q}$  can be approximated as

$$\begin{aligned}\tilde{B}_j^\pm = & \frac{J_j}{2} \frac{|\nabla \eta|_{j\pm\frac{1}{2}}}{J_{j\pm\frac{1}{2}}} \left\{ B_j [1 \pm \text{sign}(\tilde{V}_j) \cos^2 \theta_j] \right. \\ & \pm [s_j \Delta^*(\rho \tilde{q})_j \cos^2 \theta_j + \frac{c_{j\pm\frac{1}{2}} - |\tilde{V}_{j\pm\frac{1}{2}}|}{c_{j\pm\frac{1}{2}}^2} p_j \sin^2 \theta] M_j \\ & \left. \pm |\tilde{V}_{j\pm\frac{1}{2}}| \sin^2 \theta I \pm \frac{\rho_{j\pm\frac{1}{2}} (c_{j\pm\frac{1}{2}} - |\tilde{V}_{j\pm\frac{1}{2}}|) \sin^2 \theta}{\rho_j} N_{j\pm\frac{1}{2}} \right\}\end{aligned}\quad (14)$$

where  $B = \partial F / \partial Q$ ,  $I$  is the identity matrix,

$$M = \frac{1}{\rho} \frac{\partial \rho \mathbf{e}_s}{\partial Q} = \frac{1}{\rho} \begin{pmatrix} 1 & 0 & 0 & 0 & 0 \\ 0 & 1 & 0 & 0 & 0 \\ 0 & 0 & 1 & 0 & 0 \\ 0 & 0 & 0 & 1 & 0 \\ \frac{\gamma-1}{2}(u^2 + v^2 + w^2) & -(\gamma-1)u & -(\gamma-1)v & -(\gamma-1)w & \gamma \end{pmatrix}$$

$$N = \mathbf{e}_d \cdot (0, k_x, k_y, k_z, 0) = \begin{pmatrix} 0 & 0 & 0 & 0 & 0 \\ 0 & k_x^2 & k_x k_y & k_x k_z & 0 \\ 0 & k_y k_x & k_y^2 & k_y k_z & 0 \\ 0 & k_z k_x & k_z k_y & k_z^2 & 0 \\ 0 & V^f k_x & V^f k_y & V^f k_z & 0 \end{pmatrix}$$

noticed in the unsteady results. The convergence of the unsteady computations to a periodic flow is verified by comparing the results between cycles. For all cases considered here, the results for the third cycle give pressure profiles that are identical to those of the second-cycle results. Thus, the numerical transient is confirmed to disappear within two cycles.

The present upwind results are also compared with the results obtained by using the existing CD method. Reference 13 discusses the CD results obtained from the same test case. The CD method uses the diagonal inversions of the Beam-Warming method (ref. 9), and thus it is first-order accurate but non-conservative in time. Its artificial dissipation model consists of second- and fourth-order dissipation terms controlled by the amount of the second-difference of pressure.

### Inviscid Solutions

First, the inviscid coarse-grid ( $91 \times 25 \times 25$  points) solutions are presented. Figure 1 compares the computed and measured unsteady, upper-surface pressure coefficients for the real and imaginary parts of the first Fourier component. Pressure coefficients are shown for various span locations. The computations were done by using the upwind algorithm with the LU-ADI method (UP-LU). The solid, dashed, and dotted lines in the figure indicate the results obtained using 1440, 720, and 360 time-steps per cycle of oscillation (steps/cycle), respectively. (The time-steps per cycle rate of 1440 corresponds to  $\Delta t \simeq 0.02$ .) The solution profiles obtained using 1800 steps/cycle coincided with those using 1440 steps/cycle. Thus, the unsteady pressure profiles converged with respect to time-step sizes at 1440 steps/cycle. In addition, because the differences between the results with 720 and 1440 steps/cycle are not critical when making comparisons with experimental data, the computation with 720 steps/cycle is acceptable for numerical efficiency.

Figure 2 shows the analogous CD results. In this case, the second- and fourth-order dissipation coefficients are fixed at 0.25 and 0.01, respectively (denoted as CD(0.01)). These coefficients are the values that were used in references 1, 2, 9 and 13. The CD results show less dependence on time-step size than do the UP-LU results, although the profiles are smeared out at the large-gradient region near the shock wave and leading-edge regions. In order to check the dependence of the CD method on the amount of numerical dissipation, computations were tried with half the amount of dissipation coefficients (0.125, 0.005). At 360 steps/cycle, the computation became unstable with these coefficients. At 720 and 1440 steps/cycle, the computations were stable, but the resulting unsteady pressure profiles were still smeared out.

Figure 3 shows the results using the approximate block ADI method applied to the present upwind algorithm (UP-BL). The UP-BL method was not stable for computations using 360 and 720 steps/cycle, and thus the computations were done using 1080, 2160, and 3600 steps/cycle. The solution profiles obtained with 3600 steps/cycle finally showed good agreement with the UP-LU result converged at 1440 steps/cycle.

Figure 4 compares the three methods, UP-LU, UP-BL, and CD(0.01), fixing the number of time-steps per cycle at 1440. Both UP-LU and UP-BL results give similar profiles at the shock motion, although the UP-LU method is nonconservative in time. Both upwind methods give better agreement with the experimental data in the region of the shock motion than the CD method.

shown by oscillations in the pressure profiles of CD(0.01). However, the UP-LU result shows that the UP-LU method relaxes this stability requirement. Thus, time-step sizes for the UP-LU method are not limited by stability considerations even for the viscous case.

Figure 7 shows the corresponding results with 1440 steps/cycle. This is the time-step rate suggested in reference 13. Here, the CD(0.01) solution becomes stable and agrees reasonably well with the experimental data. To check whether the amount of dissipation is reasonable, the dissipation coefficients were reduced by half, as was done for the inviscid case, but the CD(0.005) computation diverged for the viscous case. In figure 7, and analogous to the inviscid results shown in figure 5, the CD solutions approach the UP-LU solution as the dissipation coefficients are reduced. Again the UP-LU method is confirmed to give a less-dissipative and thus more accurate solution than the CD method. The viscous solutions in figure 7 are similar to the inviscid solutions in shown in figure 5 because the experimental flow field does not contain strong viscous effect (ref. 12).

These results also indicate that the CD method is sensitive to both time-step size and to the amount of artificial dissipation added. Therefore, users of the CD method are required to find an adequate combination of time-step size and dissipation coefficients on a case-by-case basis. In contrast, the UP-LU method is robust, and users do not have to find any dissipation coefficient.

For the viscous case, the UP-LU computation requires 18.9  $\mu$ sec per grid point per time step at a speed of 141 MFLOPS on a CRAY-YMP computer using a single processor, and the CD computation requires 17.1  $\mu$ sec at a speed of 132 MFLOPS. There is 11% increase of CPU time when the upwind option of the code is used.

## CONCLUSIONS

A new streamwise upwind algorithm has been derived to compute unsteady flow fields with a moving grid system. The temporally nonconservative lower-upper-factored, alternating-direction-implicit (LU-ADI) method has been applied to compute flow over an oscillating wing at a transonic Mach number. A comparison of the temporally nonconservative method with a time-conservative version of the upwind scheme indicates that the solutions are insensitive to the time-conservativeness of the implicit solvers when practical time-step sizes are used. The temporally nonconservative upwind method was found to be more stable and twice as efficient as the time-conservative block ADI scheme, even though the block ADI scheme employed an approximate form of the Jacobians. Comparisons have been made between results obtained with both upwind schemes, with experimental measurements, and with computed results obtained using the existing central-difference method.

Comparisons with experimental data show that the upwind algorithm predicts the shock motion better than the central-difference (CD) method. The CD solutions are also found to be sensitive to the amount of numerical dissipation, and as a result, the dissipation coefficients must be specified case by case. In comparison, the present upwind method does not require a dissipation coefficient. Thus, the method that combines the streamwise upwind and LU-ADI methods is proposed for practical computations. This new upwind method is incorporated in the aeroelastic code ENSAERO. The new upwind option of the code allows larger time-steps and thus is more efficient, even though it requires slightly more computational time per time-step than the CD option.

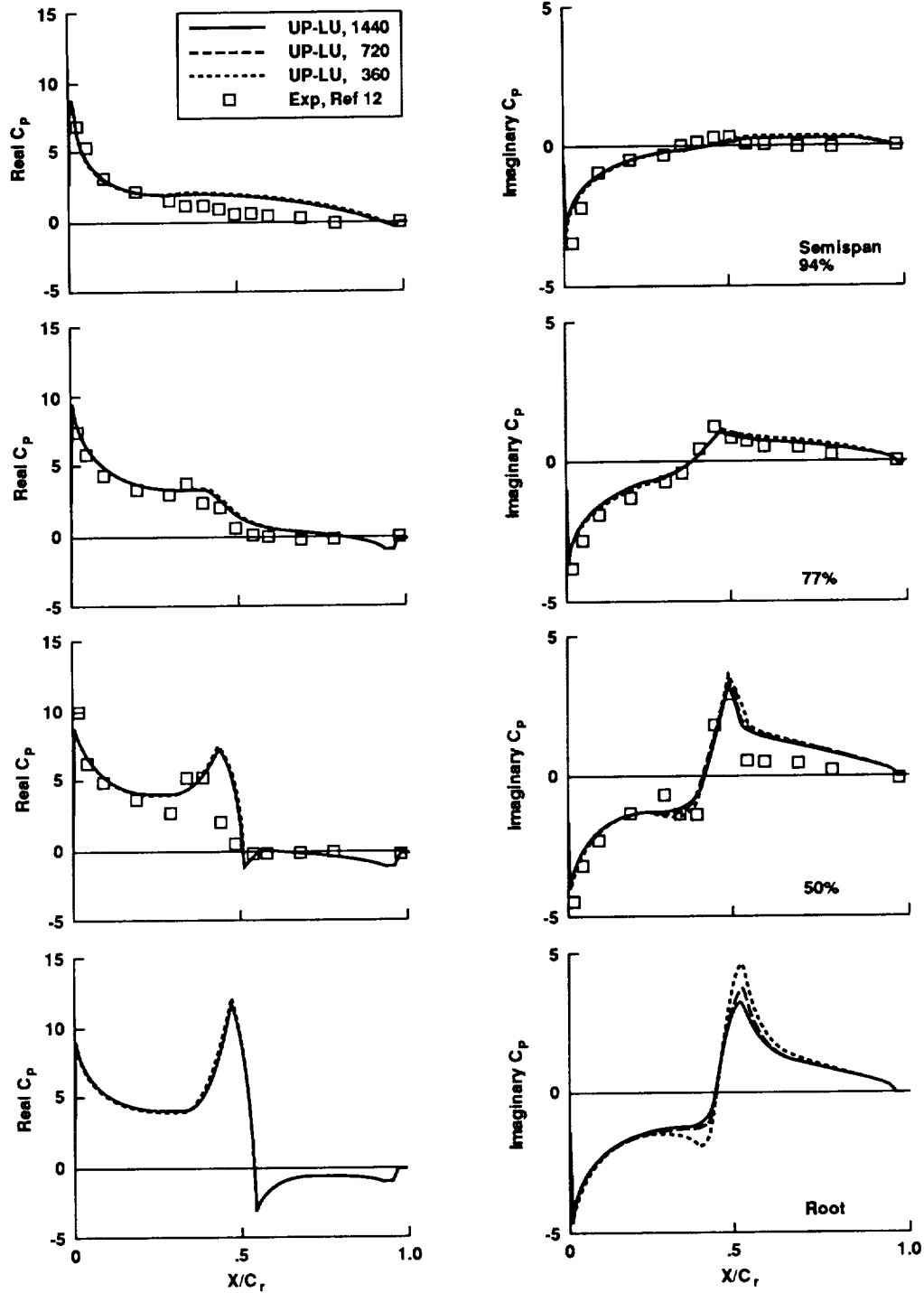


Figure 1. Effect of time-step sizes on inviscid upper-surface unsteady pressures for the rectangular wing computed by using the upwind LU-ADI method:  $91 \times 25 \times 25$  grid,  $M_\infty = 0.8$ ,  $\alpha_m = 0^\circ$ ,  $k = 0.27$ , and  $\alpha_0 = 1^\circ$ .

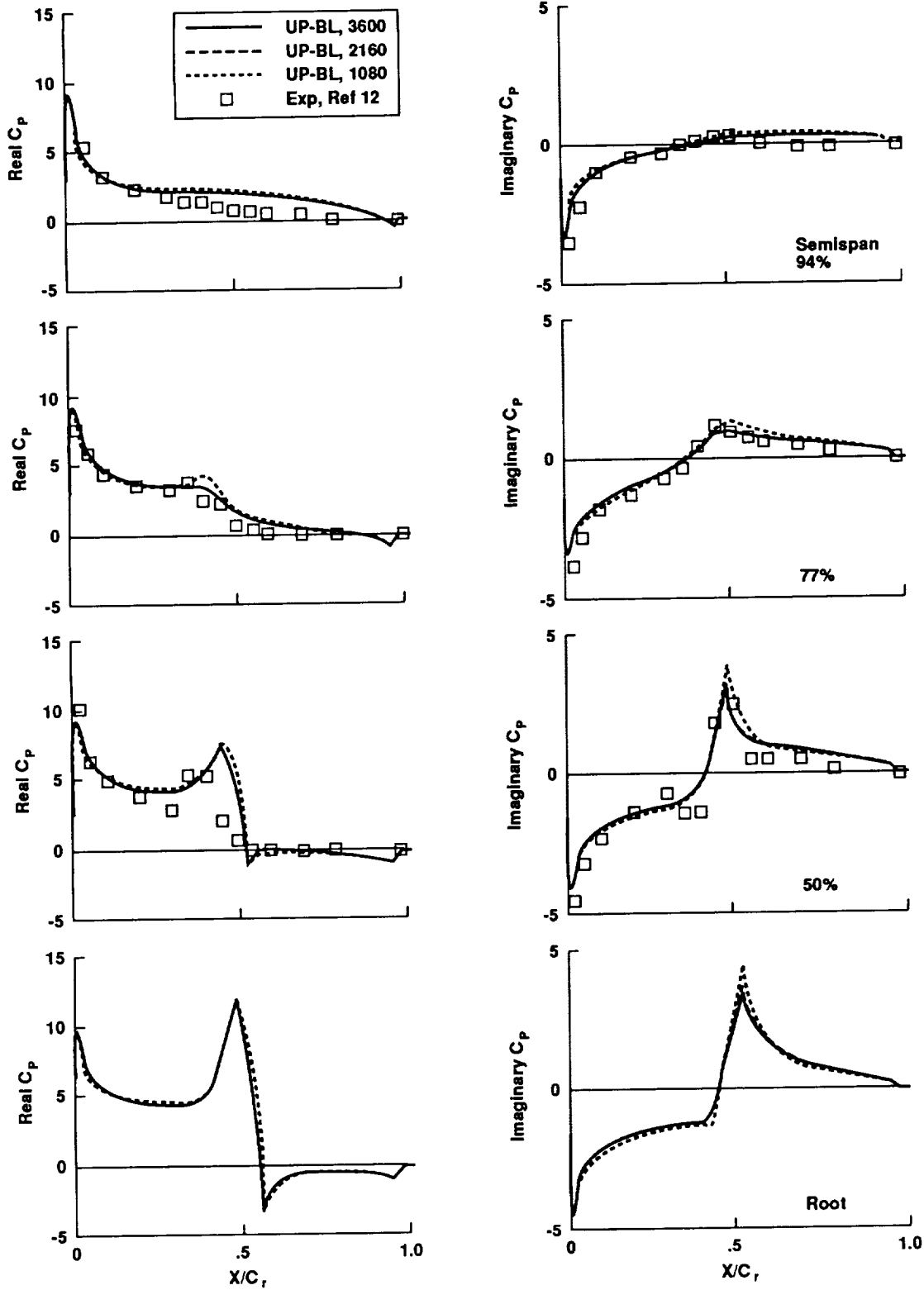


Figure 3. Effect of time-step sizes on inviscid upper-surface unsteady pressures for the rectangular wing computed by using the upwind block ADI method:  $91 \times 25 \times 25$  grid,  $M_\infty = 0.8$ ,  $\alpha_m = 0^\circ$ ,  $k = 0.27$ , and  $\alpha_0 = 1^\circ$ .

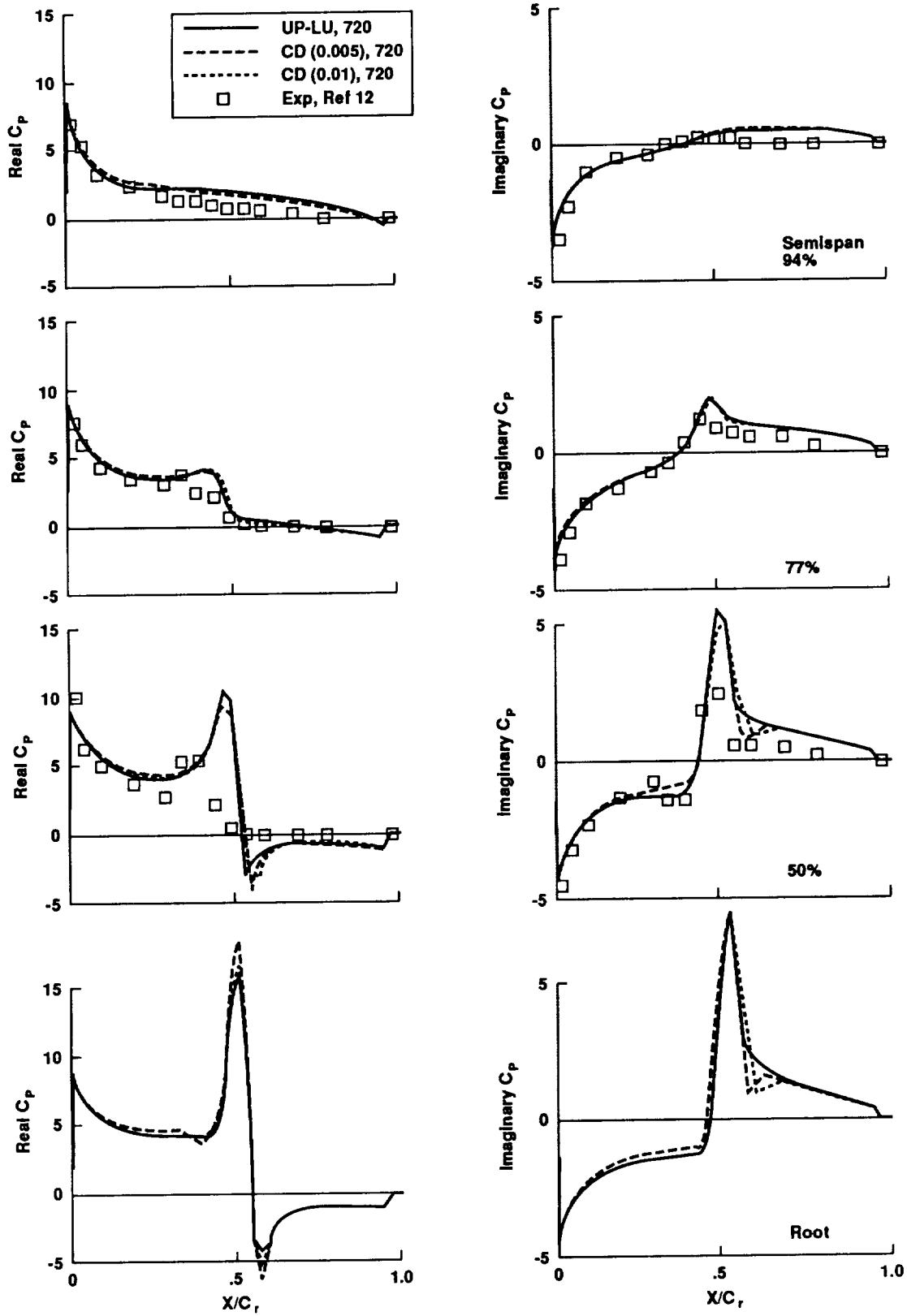


Figure 5. Comparison of inviscid upper-surface unsteady pressures computed by using the upwind LU-ADI method and the central-difference method with two sets of dissipation coefficients:  $151 \times 25 \times 34$  grid,  $M_\infty = 0.8$ ,  $\alpha_m = 0^\circ$ ,  $k = 0.27$ , and  $\alpha_0 = 1^\circ$ .



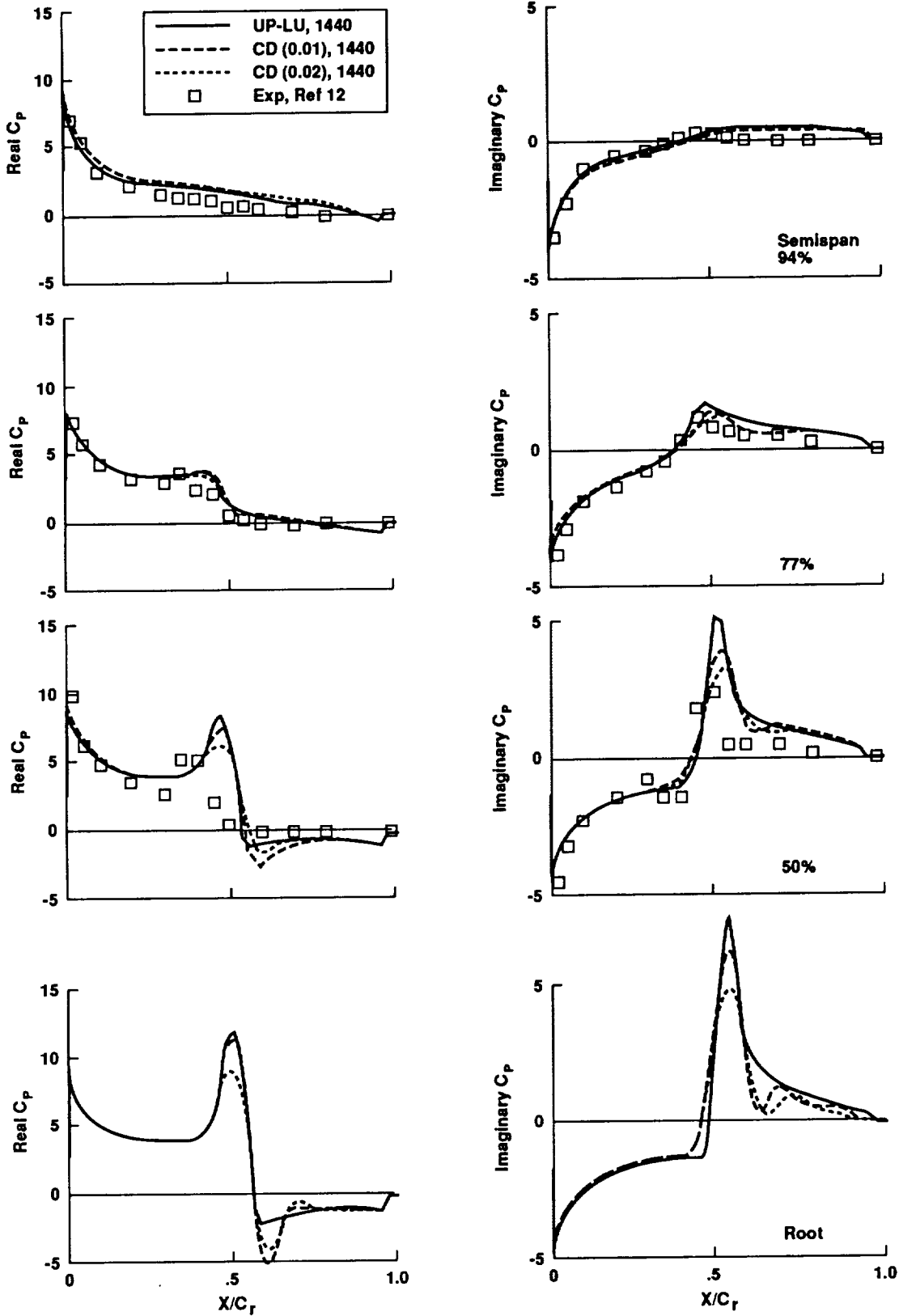


Figure 7. Comparison of viscous upper-surface unsteady pressures computed by using 1440 time-steps/cycle:  $151 \times 25 \times 34$  grid,  $Re = 2 \times 10^6$ ,  $M_\infty = 0.8$ ,  $\alpha_m = 0^\circ$ ,  $k = 0.27$ , and  $\alpha_0 = 1^\circ$ .



# **APPENDIX C**



90A 45915

**AIAA-90-3103 Application of a Streamwise  
Upwind Algorithm for Unsteady Transonic  
Computations Over Oscillating Wings**

S. Obayashi, G. Guruswamy and P. Goorjian,  
NASA-Ames, Moffett Field, CA

**AIAA 8th Applied Aerodynamics Conference**

August 20-22, 1990 / Portland, OR

## Application of a Streamwise Upwind Algorithm for Unsteady Transonic Computations over Oscillating Wings

Shigeru Obayashi,\* Guru P. Guruswamy,\*\* and Peter M. Goorjian\*\*

NASA Ames Research Center, Moffett Field, California

### Abstract

A new streamwise upwind algorithm has been derived to compute unsteady flows with a moving grid system and applied to compute flows over oscillating wings at transonic Mach numbers. Comparisons have been made between results obtained from this upwind algorithm, using both temporally nonconservative- and conservative-implicit methods, with the results obtained from a central-difference method, and also with experimental data. The results show (1) the efficiency and practicality of the temporally nonconservative implicit solver and (2) the robustness and accuracy of the upwind method for unsteady computations compared to the central-difference method.

### Introduction

In the last two decades, there have been extensive developments in computational aerodynamics, which constitutes a major part of the general area of computational fluid dynamics. Such developments are essential to advance the understanding of the physics of complex flows, to complement expensive wind-tunnel tests, and to reduce the overall design cost of an aircraft, particularly in the area of aeroelasticity.

Aeroelasticity plays an important role in the design and development of aircraft, particularly modern aircraft, which tend to be more flexible. Several phenomena that can be dangerous and limit the performance of an aircraft occur because of the interaction of the flow with flexible components. For example, an aircraft with highly swept wings may experience vortex-induced aeroelastic oscillations.<sup>1</sup> Also, undesirable aeroelastic phenomena due to the presence and movement of shock waves occur in the transonic range. Aeroelastically critical phenomena, such as a low transonic

flutter speed, have been known to occur through limited wind-tunnel tests and flight tests.

Aeroelastic tests require extensive cost and risk. An aeroelastic wind-tunnel experiment is an order of magnitude more expensive than a parallel experiment involving only aerodynamics. By complementing the wind-tunnel experiments with numerical simulations, the overall cost of the development of aircraft can be considerably reduced. In order to accurately compute aeroelastic phenomenon it is necessary to solve the unsteady Euler/Navier-Stokes equations simultaneously with the structural equations of motion.

At Ames a code, ENSAERO, is being developed for computing the unsteady aerodynamics and aeroelasticity of aircraft and it solves the Euler/Navier-Stokes equations. The capability of the code has been demonstrated by computing vortical and transonic flows over flexible swept wings.<sup>2,3</sup> The flow fields were calculated by a time-accurate, finite-difference scheme based on central differencing.

The motivation of this study is to enhance the algorithm capability of the present code. Toward this goal, the use of a new upwind scheme in comparison to the current central-difference (CD) scheme is investigated in this paper. The CD scheme requires artificial dissipation to stabilize computations. In general, such artificial dissipation models lead to more dissipative, and thus less accurate, solutions than upwind schemes. In addition, the CD scheme is sensitive to the amount of dissipation and it is necessary to specify a dissipation coefficient on a case by case basis. On the other hand, upwind schemes do not require any coefficient to be specified.

Among upwind algorithms, a streamwise upwind algorithm has recently been developed and applied to steady-state problems of transonic flows over wings<sup>4</sup> and vortical flows over a delta wing<sup>5</sup> on fixed grids. Most multidimensional upwind algorithms are first constructed in one dimension and then extended to multidimensions by applying the one-dimensional procedure in each coordinate direction. By comparison, the present method uses the local stream direction, flow velocity, and pressure gradient to construct the upwinding. The switching of flux evaluations always takes place at sonic values, where transonic shock waves may be located. Therefore, this method follows the flow physics more closely than the coordinate upwind methods. The computed results confirmed the higher resolution of the present algorithm over the CD method as well as over other upwind

\*Research Scientist, MCAT Institute, member AIAA

\*\*Research Scientist, AIAA Associate Fellow

Copyright © 1990 by the American Institute of Aeronautics and Astronautics, Inc. No copyright is asserted in the United States under Title 17, U.S. Code. The U.S. Government has a royalty-free license to exercise all rights under the copyright claimed herein for Governmental purposes. All other rights are reserved by the copyright owner.

For a moving system,

$$\begin{aligned}\hat{V}_{moving} &= \eta_t + \eta_x u + \eta_y v + \eta_z w \\ &= \eta_x(u - x_t) + \eta_y(v - y_t) + \eta_z(w - z_t) \\ &= \nabla \eta \cdot \tilde{q}\end{aligned}$$

where  $\eta_t = -\eta_x x_t - \eta_y y_t - \eta_z z_t$ . Then the formulas for a fixed system can be rewritten for a moving system. Note that the present algorithm uses  $x_t$ ,  $y_t$ , and  $z_t$  to obtain the flow velocity for upwinding in the streamwise direction, instead of  $\xi_t$ ,  $\eta_t$ , and  $\zeta_t$  to compute the contravariant velocity for upwinding in the coordinate direction.

The present algorithm can be summarized with a surface vector  $S = \frac{\nabla \eta}{J}$  and a motion of its centroid,  $\mathbf{x}_t = (x_t, y_t, z_t)$ , as

$$\hat{F}(Q_l, Q_r, S_{j+\frac{1}{2}}, \mathbf{x}_{t,j+\frac{1}{2}}) = \frac{|\nabla \eta|}{J} \left( \frac{1}{2} [F_l^+ + F_r^-] - k_t Q_\infty \right) \quad (4)$$

where

$$F_{l,r}^\pm = \begin{bmatrix} f_{l,r}^\pm \\ f_{l,r}^\pm u_{l,r} + k_x p_{l,r}^\pm \\ f_{l,r}^\pm v_{l,r} + k_y p_{l,r}^\pm \\ f_{l,r}^\pm w_{l,r} + k_z p_{l,r}^\pm \\ f_{l,r}^\pm H_{l,r} - k_t p_{l,r}^\pm + (|\tilde{V}_m| \Delta p - \tilde{V}_m \Delta_2) \sin^2 \theta \end{bmatrix}$$

$$\begin{aligned}f_{l,r}^\pm &= (\rho \tilde{V})_{l,r} \{ 1 \pm \text{sign}(\tilde{V}_{l,r}) \cos^2 \theta_{l,r} \} \\ &\quad \pm s_{l,r} \Delta^*(\rho \tilde{q})_{l,r} \cos^2 \theta_{l,r} \pm \rho_{l,r} |\tilde{V}_m| \sin^2 \theta \\ &\quad - \frac{1}{2} \Delta_1 \sin^2 \theta\end{aligned}$$

$$p_{l,r}^\pm = p_{l,r} \{ 1 \pm \text{sign}(\tilde{V}_{l,r}) \cos^2 \theta_{l,r} \} - \frac{1}{2} \Delta_2 \sin^2 \theta$$

$$\begin{aligned}\tilde{V}_{l,m,r} &= k_x(u_{l,m,r} - x_t) + k_y(v_{l,m,r} - y_t) \\ &\quad + k_z(w_{l,m,r} - z_t)\end{aligned}$$

where  $\tilde{q}^2 = (u - x_t)^2 + (v - y_t)^2 + (w - z_t)^2$  and  $\Delta^*(\rho \tilde{q}) = \rho^* \tilde{q}^* - \rho \tilde{q}$  with local sonic values,

$$(\tilde{q}^*)^2 = \frac{2}{\gamma + 1} (a^2 + \frac{\gamma - 1}{2} \tilde{q}^2)$$

$$\rho^* = \rho \left( \frac{(\tilde{q}^*)^2}{a^2} \right)^{\frac{1}{\gamma - 1}}$$

and where

$$\Delta_1 = (a_m - |\tilde{V}_m|) \frac{\Delta p}{a_m^2}$$

$$\Delta_2 = (a_m - |\tilde{V}_m|) \rho_m \Delta V$$

with  $\Delta \cdot = \cdot_r - \cdot_l$ ,  $V = k_x u + k_y v + k_z w$ ,  $k_t = -k_x x_t - k_y y_t - k_z z_t$ ,  $k_x = \eta_x / |\nabla \eta|$ , and so on. The subscripts  $l$ ,  $m$  and  $r$  denote the left, averaged and right state of the flow variables. The averaged state is defined for  $\rho$ ,  $u$ ,  $v$ ,  $w$ , and  $H$  by the arithmetic average of the left and right states. The basic scheme is first-order accurate with  $l = j$  and  $r = j + 1$ . The term,  $k_t Q_\infty$ , subtracts the free-stream for time-metrics.

The switches  $s_l$  and  $s_r$  are defined in the manner of Goudonov's method as follows. For  $\tilde{V} \geq 0$ ,

$$\begin{aligned}s_l &= 1 - \varepsilon_l \varepsilon_m \\ s_r &= (1 - \varepsilon_m)(1 - \varepsilon_r)\end{aligned} \quad (5)$$

where

$$\varepsilon_{l,m,r} = \frac{1}{2} \{ 1 + \text{sign}(M_{l,m,r}^2 - 1) \}$$

and  $M = \tilde{q}/a$ .

A simple way to evaluate the rotation angle is to use  $\cos \theta = \tilde{V}/\tilde{q}$ . In supersonic flow fields, however, it is important to detect whether the velocity projected to the grid line is beyond the Mach cone. Thus,  $\tilde{V}/\tilde{q}$  is replaced by  $M \cdot \tilde{V}/\tilde{q} = \tilde{V}/a$ . If  $\tilde{V}/a$  becomes larger than one,  $\cos \theta$  is set to one. To avoid expansion shocks,<sup>5</sup> the rotation angle is determined by a mixture of averaged ( $m$ ) and pointwise ( $l, r$ ) values:

$$\cos^2 \theta_{l,r} = \min \left[ (1 - \phi) \frac{\tilde{V}_m^2}{a_m^2} + \phi \frac{\tilde{V}_{l,r}^2}{a_{l,r}^2}, 1 \right] \quad (6)$$

The following relation is used for evaluating  $\phi \in [0, 1]$  in this paper because of the smoothness:

$$\phi = \max \left[ \frac{2\gamma}{\gamma + 1} \left( 1 - \frac{1}{2\gamma} \{ \gamma - 1 + (\gamma + 1) \frac{p_2}{p_1} \} \right), 0 \right] \quad (7)$$

where  $p_1$  and  $p_2$  denote upstream and downstream pressures, respectively. The sine is determined by an arithmetic average of the cosines:  $\sin^2 \theta = 1 - \frac{1}{2} (\cos^2 \theta_l + \cos^2 \theta_r)$ .

Higher-order schemes are constructed from a one-parameter family,  $\kappa$ , of interpolations of the primitive variables,  $\rho$ ,  $u$ ,  $v$ ,  $w$ , and  $p$ . For example,

$$p_l = \{ 1 + \frac{\psi_j}{4} [(1 - \kappa) \nabla + (1 + \kappa) \Delta] \} p_j$$

$$p_r = \{ 1 - \frac{\psi_{j+1}}{4} [(1 + \kappa) \nabla + (1 - \kappa) \Delta] \} p_{j+1} \quad (8)$$

where  $\nabla$  and  $\Delta$  are backward and forward difference operators, respectively.<sup>9</sup> For the third-order scheme,  $\kappa = \frac{1}{3}$ , Koren's differentiable limiter<sup>10</sup> is used in this paper. The limiter  $\psi$  is calculated as

$$\psi_j = \frac{3 \nabla p_j \Delta p_j + \epsilon}{2(\Delta p_j - \nabla p_j)^2 + 3 \nabla p_j \Delta p_j + \epsilon} \quad (9)$$

where a small constant  $\epsilon$ ,  $\epsilon = 10^{-6}$  typically, is added to prevent the division by zero. The same formulas are used for the other primitive variables.

## LU-ADI Method

The time marching method used for the present upwind scheme is the LU-ADI factorization method proposed by one of the present authors.<sup>7</sup> The LU-ADI method is a compromise of ADI and LU factorization. This method applied to Eq. (3) is written as

$$\begin{aligned}(T_\xi L_A D_A U_A T_\xi^{-1})(T_\eta L_B D_B U_B T_\eta^{-1}) \\ (T_\zeta L_C D_C U_C T_\zeta^{-1}) = \Delta t R.^\# \end{aligned} \quad (10)$$

Unsteady computations are started from the corresponding steady-state solution. The convergence of the unsteady computations to a periodic flow is verified by comparing the results between cycles. For all cases presented here, the third-cycle results give identical pressure profiles to those of the second-cycle results. Thus the numerical transient is confirmed to disappear within two cycles.

First, the LU-ADI upwind method was applied to compute this inviscid flow on the coarse ( $91 \times 25 \times 25$  point) grid using 360, 720, 1080, 1440, and 1800 time steps per cycle of oscillation (steps/cycle). The unsteady pressure profiles on the wing surface that were obtained using 1800 steps/cycle coincided with those using 1440 steps/cycle. The computation converged with respect to time-step sizes at 1440 steps/cycle. Except for the result using 360 steps/cycle, differences between the other results were small. Thus, 720 steps/cycle is acceptable for practical computations.

The CD method showed less dependence on time-step sizes than the LU-ADI upwind method. The CD computation converged at 720 steps/cycle. The block-ADI upwind method showed more dependence on time-step size. The solution profiles obtained with 3600 steps/cycle finally gave a good agreement with the LU-ADI upwind result obtained at 1440 steps/cycle. The block-ADI computations were not stable for 360 and 720 steps/cycle.

Figure 1 shows the comparison of real and imaginary parts of the first Fourier component between the computed and measured unsteady upper-surface pressure coefficients of the wing at various spanwise locations, using the three methods with 1440 steps/cycle. Both upwind results give similar profiles of the shock motion, although the LU-ADI upwind method is nonconservative in time. Both upwind results give crisper profiles (narrower peaks) at the region of the shock motion than the CD result.

These results indicate that the temporally nonconservative LU-ADI method can be used for unsteady computations even with moving shock waves when a large enough number of time steps (*i.e.*, small  $\Delta t$ ) is used per cycle. In the present case, any number greater than 720 will give practical results. The CD method also uses the temporally nonconservative diagonal form. However, the result differs from both upwind results. This indicates that the solution depends on the numerical dissipation more than the time-conservative properties of the methods. The block-ADI method requires twice as much CPU time as the LU-ADI method, but its accuracy does not appear to compensate for the increased computational time. Thus, the block-ADI method will be dropped in the following computations.

Next, the inviscid computations were repeated on a finer ( $151 \times 25 \times 34$  point) grid to check the grid dependency. Figure 2 shows the comparison of unsteady pressures using the LU-ADI upwind and CD methods. Both computations use 720 steps/cycle, as suggested in the coarse-grid case. Compared with the coarse-grid solution in Fig. 1, the CD solution tends to converge to the upwind solution due to the grid refinement, although the profiles are still slightly

smeared at the peak. Therefore, the upwind method is confirmed to give a less dissipative and thus more accurate solution than the CD method.

## F-5 Wing

The second test considers unsteady viscous flows over an F-5 wing which has an aspect ratio of 2.98, a taper ratio of 0.31 and a leading edge sweep angle of  $31.92^\circ$ . Computations were made using two grids: the coarse and fine grids containing  $121 \times 25 \times 25$  points and  $151 \times 25 \times 30$  points, respectively. Figure 3 shows the F-5 wing and the grid distributions at the root section of the fine grid. Figure 4 illustrates the motion used in the experiment conducted at the National Aerospace Laboratory of the Netherlands.<sup>16</sup> The wing is pitching about an axis located at the 50% root chord, and the pitching axis is normal to the wing root. Reference 3 discusses the CD results applied to the same test case.

The test cases are chosen at  $M_\infty = 0.896$  and 1.328 where the measured steady and unsteady data are given in Ref. 16. All F-5 wing cases are computed at  $Re = 9 \times 10^6$  based on the root chord. At these flow conditions, the coarse-grid solution gave  $y^+ \leq 13.3$  at the first shell of points above the wing surface. For both the steady and unsteady cases, the mean angle of attack  $\alpha_m$  is  $0^\circ$ . The unsteady flows are computed at a reduced frequency  $k = 0.550$  and a pitch amplitude  $\bar{\alpha} = 0.11^\circ$  for  $M_\infty = 0.896$ . Similarly,  $k = 0.396$  and  $\bar{\alpha} = 0.22^\circ$  for  $M_\infty = 1.328$ . The Baldwin-Lomax eddy-viscosity model is used to compute the turbulent viscosity coefficient.

The time-step dependency of the upwind method was checked on both the coarse and fine grids at  $M_\infty = 0.896$ . The unsteady pressure profiles converged with respect to time-step sizes at 1800 steps/cycle for the coarse grid and 2160 steps/cycle for the fine grid. For computational efficiency, 1440 and 1800 steps/cycle are deemed acceptable for the coarse and fine grids, respectively. All results shown here were computed with 1800 steps/cycle.

### $M_\infty = 0.896$

Figures 5 and 6 show the comparisons of the computed steady and unsteady pressures with the experimental data at  $M_\infty = 0.896$  using the upwind and CD methods on the coarse ( $121 \times 25 \times 25$  point) grid. For the steady case, both numerical solutions show shock-free profiles in agreement with the measured data (note that  $C_p^* = -0.196$  for  $M_\infty = 0.896$ ). For the oscillatory case, unsteady pressure peaks of the upwind solution indicates that the unsteady motion of the wing produces a shock wave. The measured data also show the peaks except at the 20% semispan location. In contrast, the unsteady pressure peaks of the CD solution are smeared out and the resulting profiles agree less favorably with the experiment except at the 20% semispan location. The computation assumes symmetry at the wing root instead of a side wall which may affect the experimental data at the

- <sup>6</sup> Baldwin, B.S. and Lomax, H., "Thin Layer Approximation and Algebraic Model for Separated Turbulent Flows," AIAA Paper 78-257, Jan. 1978.
- <sup>7</sup> Obayashi, S., "Numerical Simulation of Underexpanded Plumes Using Upwind Algorithms," AIAA Paper 88-4360-CP, Aug. 1988.
- <sup>8</sup> Vinokur, M., "An Analysis of Finite-Difference and Finite-Volume Formulations of Conservation Laws," *J. Comp. Phys.*, Vol.81, pp.1-52, 1989.
- <sup>9</sup> Anderson, W.K., Thomas, J.L. and van Leer, B., "A Comparison of Finite Volume Flux Vector Splittings for the Euler Equations," AIAA Paper 85-0122, Jan. 1985.
- <sup>10</sup> Koren B., "Upwind Schemes, Multigrid and Defect Correction for the Steady Navier-Stokes Equations," Proceedings of 11th International Conference on Numerical Methods in Fluid dynamics, June, 1988.
- <sup>11</sup> Pulliam, T. H. and Steger, J. L., "Recent Improvement in Efficiency, Accuracy, and Convergence for Implicit Approximate Factorization Algorithms," AIAA Paper 85-360, Jan. 1985.
- <sup>12</sup> Steger, J. L. and Warming, R. F., "Flux Vector Splitting of the Inviscid Gasdynamic Equations with Application to Finite-Difference Methods," *J. Comp. Phys.*, Vol.40, pp.263-293, 1981.
- <sup>13</sup> Obayashi, S., Goorjian, P.M. and Guruswamy, G. P., "Extension of a Streamwise Upwind Algorithm to a Moving Grid System," NASA TM No. 102800, Apr. 1990.
- <sup>14</sup> Chaderjian, N. M. and Guruswamy, G. P., "Unsteady Transonic Navier-Stokes Computations for an Oscillating Wing Using Single and Multiple Zones," AIAA Paper 90-0313, Jan. 1990.
- <sup>15</sup> Mabey, D.G., Welsh, B.L. and Pyne, C.R., "A Summary of Measurements of Steady and Oscillatory Pressures on a Rectangular Wing," *The Aeronautical Journal of the Royal Aeronautical Society*, Jan. 1988.
- <sup>16</sup> Tijdeman, J. *et al.*, "Transonic Wind Tunnel Tests on an Oscillating Wing with External Stores; Part II — The Clean Wing," AFFDL-TR-78-194, March 1979.



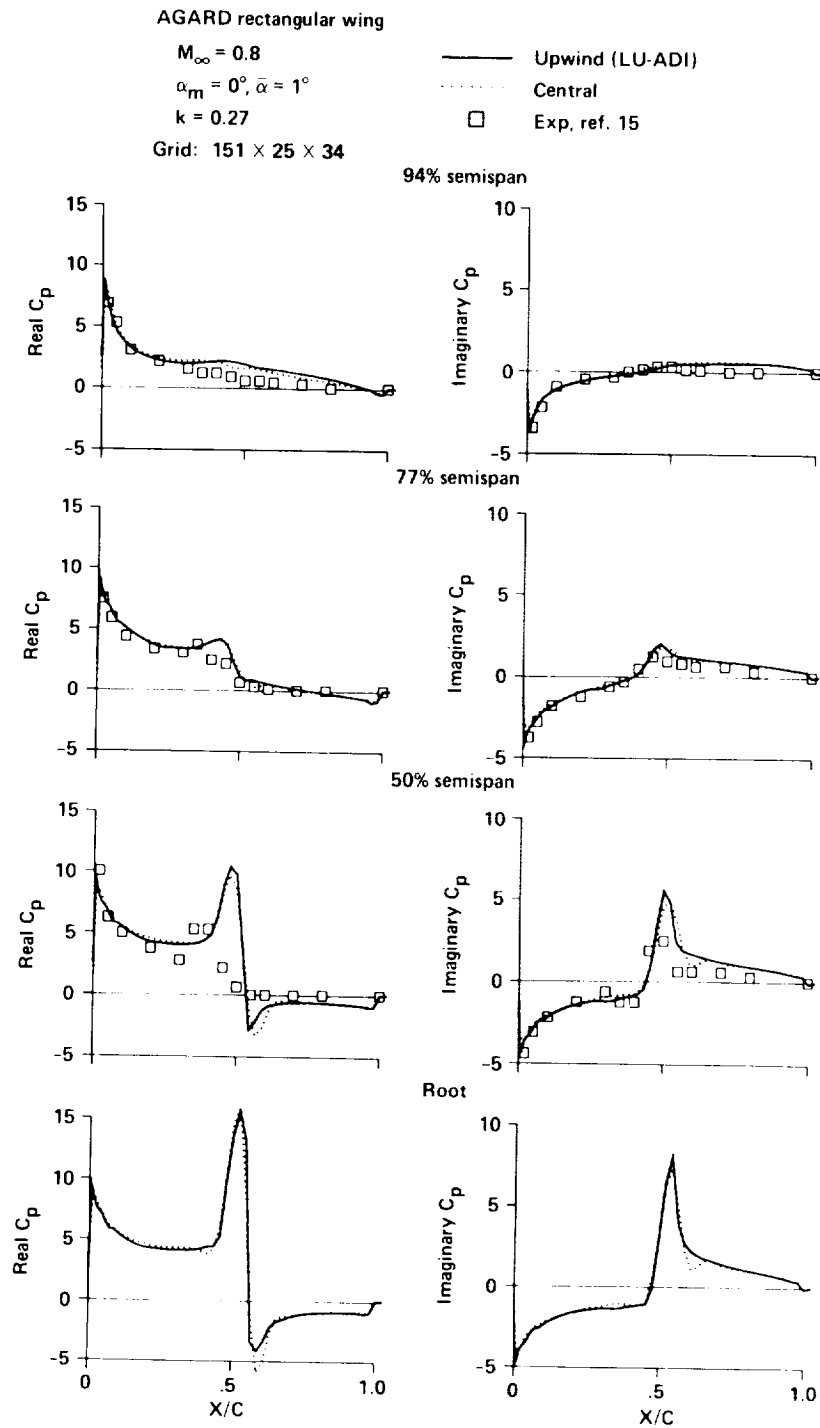


Fig. 2 Comparison of computed inviscid upper surface unsteady pressures between the LU-ADI upwind and central-difference method over the rectangular wing with the fine grid.

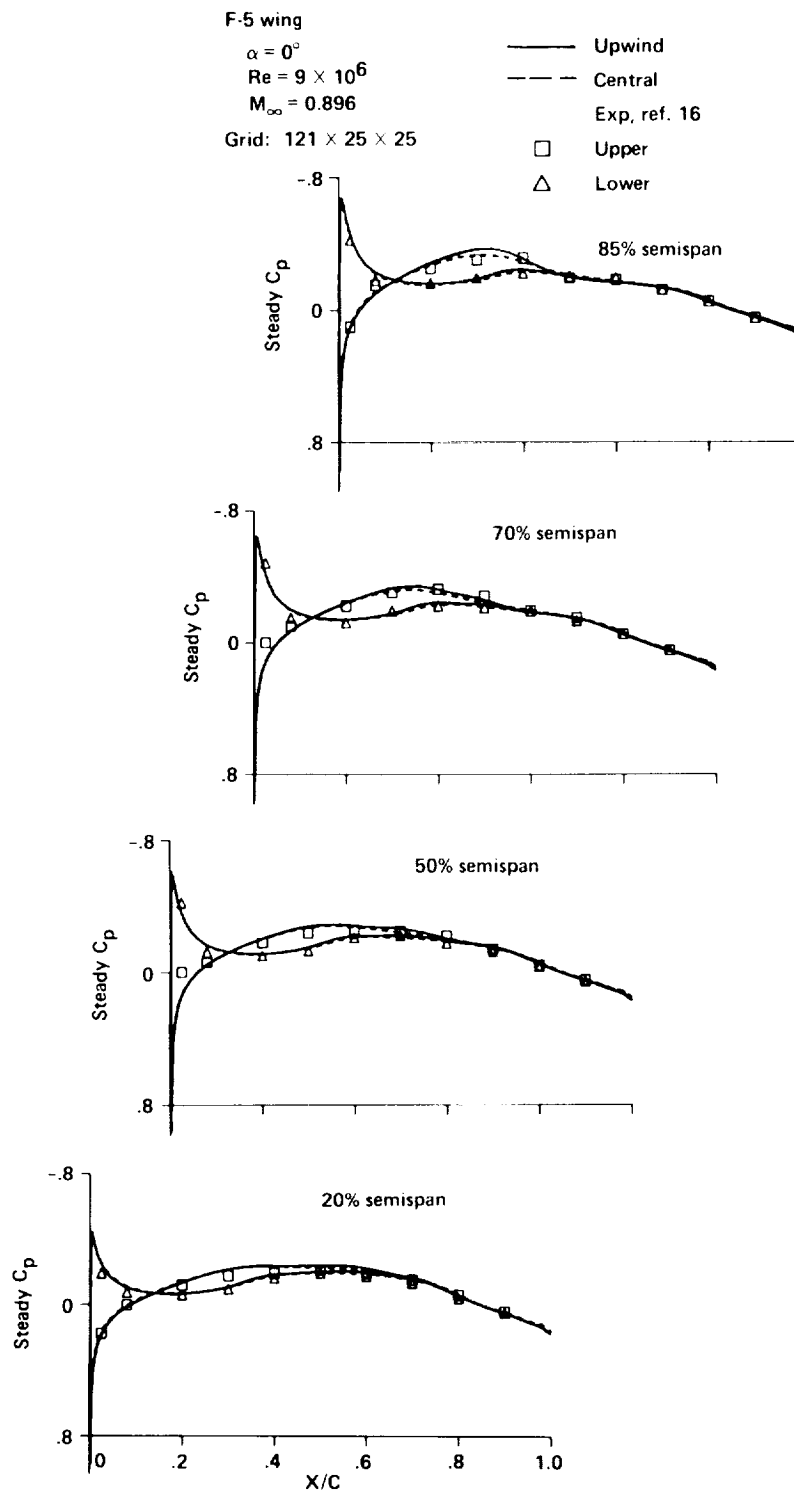


Fig. 5 Comparison of computed viscous steady pressures between the upwind and central-difference methods at  $M_\infty = 0.896$  over the F-5 wing with the coarse grid.

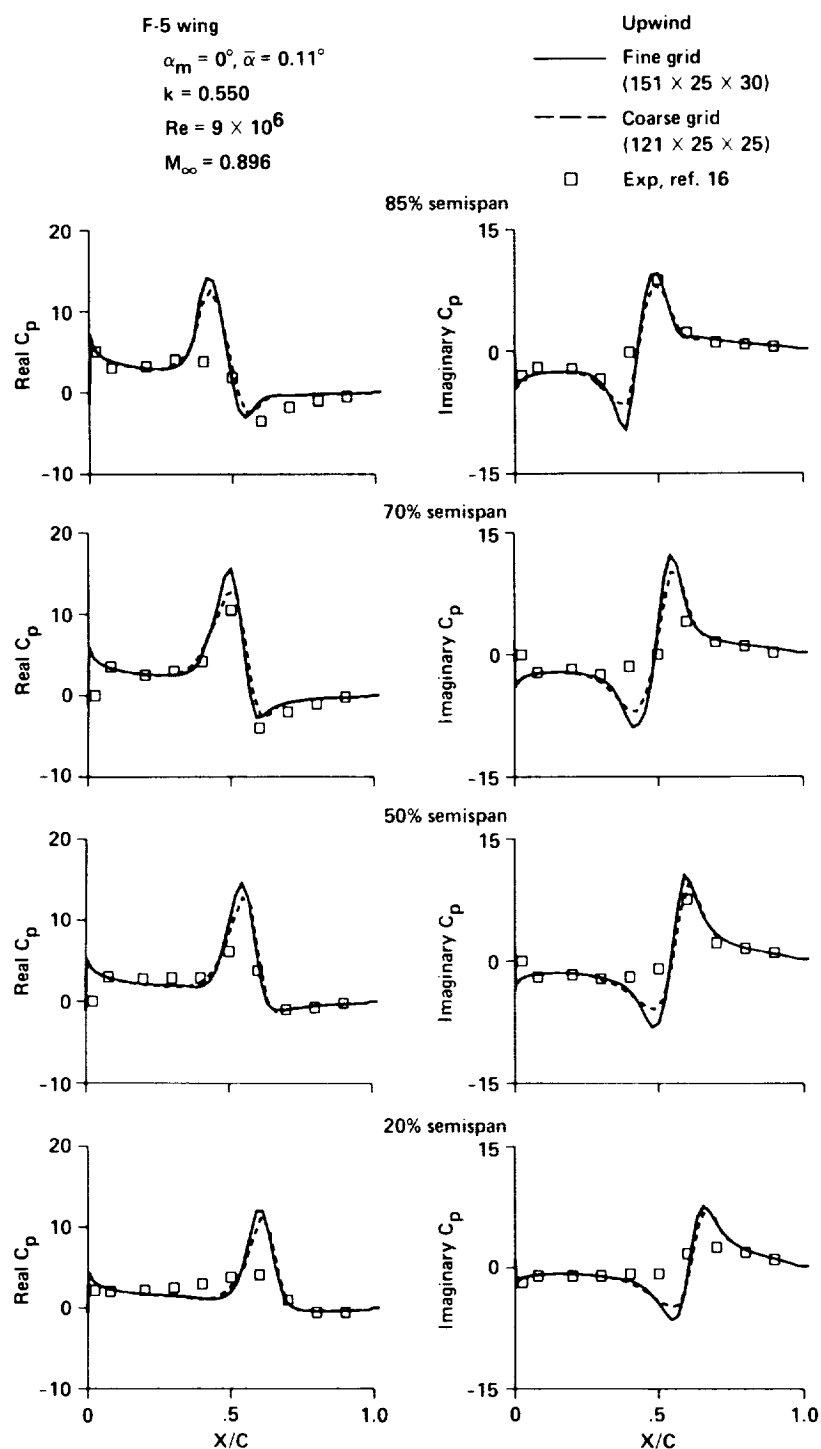


Fig. 7 Comparison of computed viscous unsteady pressures between the coarse- and fine-grid solutions at  $M_\infty = 0.896$  over the F-5 wing using the upwind method.

F-5 wing

$M_\infty = 0.896$

$\alpha = 0^\circ$  (pitching down)

$k = 0.550$

$Re = 9 \times 10^6$

Grid:  $151 \times 25 \times 30$

70% semispan

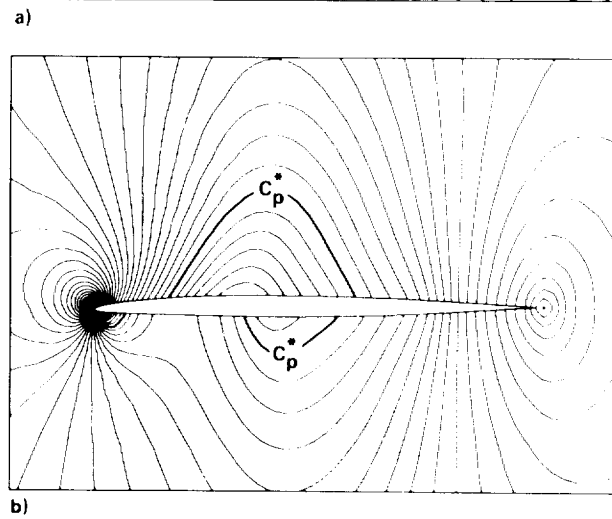
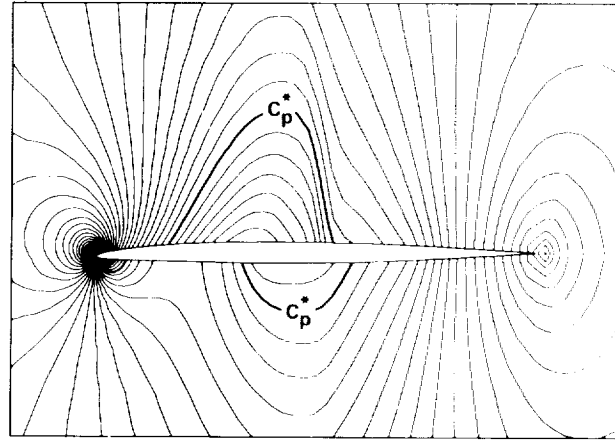


Fig. 9 Comparison of computed instantaneous pressure contours between the upwind and central-difference methods at  $M_\infty = 0.896$  over the F-5 wing with the fine grid. a) Upwind result. b) central-difference result

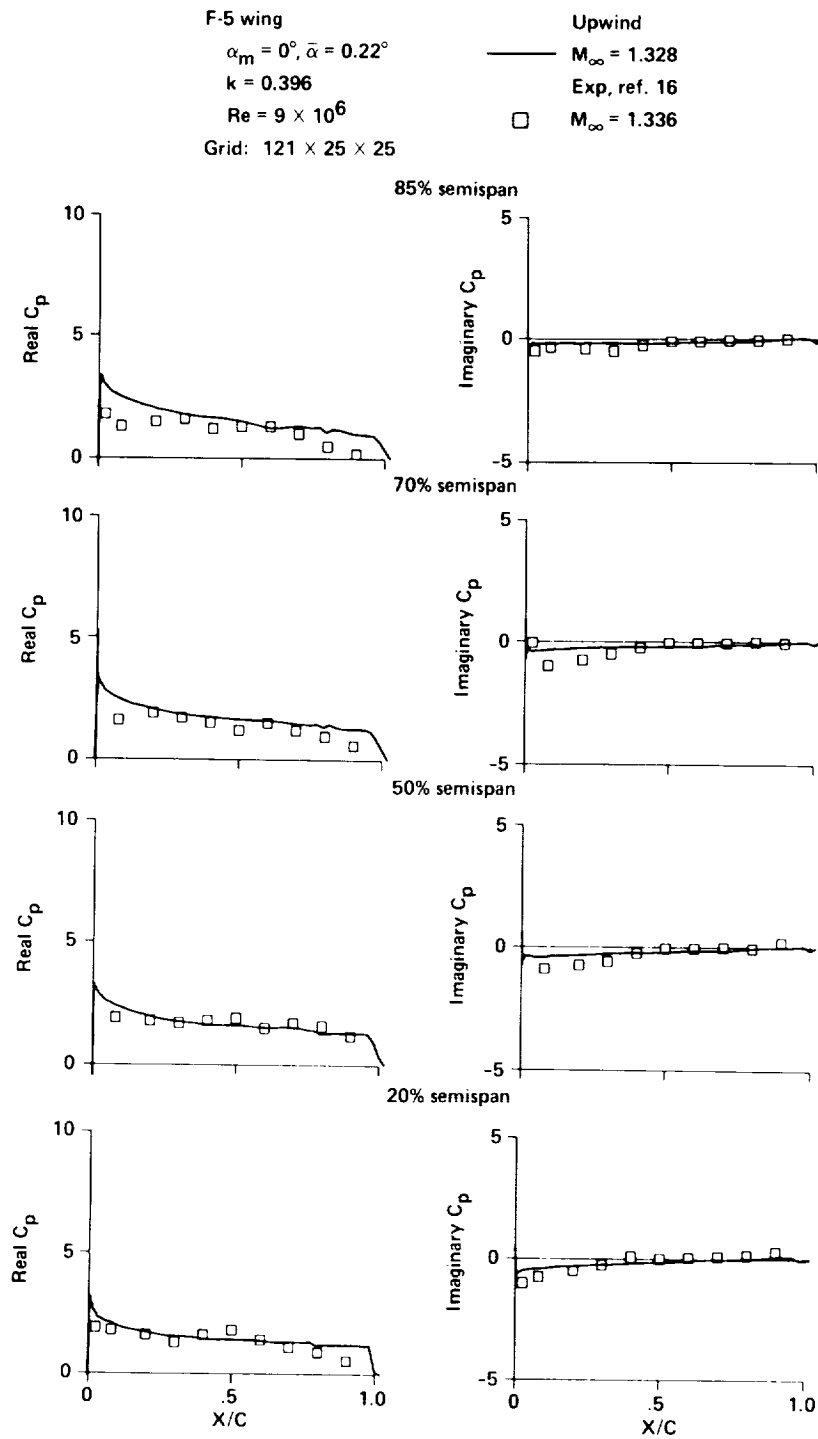


Fig. 11 Comparison of computed viscous unsteady pressures with experiment at  $M_\infty = 1.336$  over the F-5 wing with the coarse grid using the upwind method.

# APPENDIX D

91N 12157

NASA Contractor Report 177572

# **Free-Stream Capturing in Fluid Conservation Law for Moving Coordinates in Three Dimensions**

Shigeru Obayashi

Contract Number NCC2-605  
January 1991

**NASA**  
National Aeronautics and  
Space Administration

# **Free-Stream Capturing in Fluid Conservation Law for Moving Coordinates in Three Dimensions**

Shigeru Obayashi  
MCAT Institute  
San Jose, California

Prepared for  
Ames Research Center  
Contract Number NCC2-605  
January 1991



National Aeronautics and  
Space Administration

**Ames Research Center**  
Moffett Field, California 94035-1000



# **Free-Stream Capturing for Moving Coordinates in Three Dimensions**

Shigeru Obayashi\*

NASA Ames Research Center, Moffett Field, California

## **Introduction**

Body-conforming coordinates transformation of a fluid conservation-law form is generally used in computational fluid dynamics. The metrics associated with the coordinates transformation are required to satisfy certain geometric identities to maintain the free stream.<sup>1</sup> These metrics are called free-stream capturing (or preserving) metrics. So far, numerical techniques are known to capture the free-stream on stationary grids.<sup>2-4</sup> However, the extension of the free-stream capturing metrics to moving grids is not straightforward. The error introduced by the time metrics has been overlooked because it is negligible in most cases, but it can be significant in certain applications such as helicopter rotor flow fields.<sup>5</sup>

Rigorous formulations to avoid this error were suggested in Ref. 1, and demonstrated, for example, in Ref. 6. Based on the work in Ref. 1, the present study describes detailed formulas for constructing the free-stream capturing metrics in space and time on both the finite-volume (FV) and finite-difference (FD) framework. The error introduced by the inconsistent time-metric term is also evaluated.

---

\*Research Scientist, Applied Computational Fluids Branch, MCAT Institute, San Jose, California 95127.

Using Eqs. (4) and (6), one obtains

$$\oint_S \mathbf{r} \times \mathbf{n} dS = 0 \quad (7)$$

The conservation of volume for a time-varying cell is given by

$$V(t_2) - V(t_1) = \int_{t_1}^{t_2} \oint_{S(t)} \mathbf{n} \cdot \mathbf{v}_c dS dt \quad (8)$$

The free-stream preservation due to these geometric identities can be demonstrated by substituting  $Q_\infty$ ,  $\mathbf{F}_{st\infty}$  and Eqs. (2) to (4) to Eq. (1):

$$\begin{aligned} Q_\infty[V(t_2) - V(t_1)] = & - \int_{t_1}^{t_2} [\mathbf{F}_{st\infty} \cdot (\oint_S \mathbf{n} dS) - Q_\infty(\mathbf{v}_0 - \Omega \times \mathbf{r}_0) \cdot (\oint_S \mathbf{n} dS) \\ & - Q_\infty \Omega \cdot (\oint_S \mathbf{r} \times \mathbf{n} dS) - Q_\infty (\oint_S \mathbf{n} \cdot \mathbf{v}_c dS)] dt \end{aligned} \quad (9)$$

The geometric identity, Eq. (5), suffices to capture the free stream in a fixed coordinate system, where most of steady-state computations are carried out, and in a moving coordinate system without rotation ( $\Omega = 0$ ). When the grid is moving with rotation ( $\Omega \neq 0$ ), the second geometric identity, Eq. (7), is to be satisfied. For the general motion of grid with changing cell volume, the third geometric identity, Eq. (8), is also required.

The geometric identity, Eq. (5), preserves the free stream at any instance  $t$  when  $\mathbf{v} = 0$ . Thus, the time-differential form of Eq. (1) is often used in the FV formulation. However, if the grid moves, the geometric identities have to be satisfied correctly in the integral form.

### Free-Stream Capturing in the Inertial Frame

To preserve the free-stream perfectly with a moving grid, Ref. 1 suggests to consider the rigorous FV formulations in space and time. One of the rigorous FV formulations with a grid velocity expressed in the inertial frame is shown here in detail.

Assuming that  $\mathbf{v}$  is given and then by substituting  $Q_\infty$  and  $\mathbf{F}_{st\infty}$  to Eq. (1), one obtains

$$Q_\infty[V(t_2) - V(t_1)] = -\mathbf{F}_{st\infty} \cdot \int_{t_1}^{t_2} \oint_S \mathbf{n} dS dt + Q_\infty \int_{t_1}^{t_2} \oint_S \mathbf{n} \cdot \mathbf{v} dS dt \quad (10)$$

where  $\mathbf{S}_{11',5'5}$  and  $\mathbf{S}_{122',1'}$  are the surface vectors in space and time domain. Note that this formula requires only the difference of the positions of grid points between  $t_1$  and  $t_2$ , not the grid velocity  $\mathbf{v}$  itself. Then, instead of Eqs. (6) and (8), one obtains

$$\Delta V = \sum_{cell} V_S \quad (18)$$

This identity does not mean to satisfy Eq. (7) but does satisfy Eq. (6) in the time-integral form. Therefore, Eq. (18) leads to the perfect free-stream capturing with the use of Eq. (11).

### Free-Stream Capturing in the Non-Inertial Frame

It is convenient to use the non-inertial frame for certain applications. Thus, the FV formulation with a grid velocity expressed in the non-inertial frame is shown next. The analysis also provides a deep insight for the free-stream capturing because it considers three types of motion given in Eqs. (3) and (4) separately. The discretized forms of the geometric identities in the FV method can be expressed as

$$\sum_{cell} S \mathbf{n} = 0 \quad (19)$$

$$\sum_{cell} S \mathbf{r} \times \mathbf{n} = 0 \quad (20)$$

$$\Delta V = \sum_{cell} V_{Sc} \quad (21)$$

where  $V_{Sc}$  is obtained from Eq. (16) by replacing  $\mathbf{v}$  with  $\mathbf{v}_c$  (see Ref. 1 for more details).

Reference 1 introduces the area moment  $\mathbf{M} = \int_S \mathbf{r} \times \mathbf{n} dS$  so as to satisfy the discretized geometric identity, Eq. (7), on the hexahedron:

$$\mathbf{M}_{1562} = \mathbf{r}_{165} \times \mathbf{S}_{165} + \mathbf{r}_{126} \times \mathbf{S}_{126} \quad (22)$$

where  $\mathbf{r}_{165} = \frac{1}{3}(\mathbf{r}_1 + \mathbf{r}_6 + \mathbf{r}_5)$ ,  $\mathbf{S}_{165} = \frac{1}{2}(\mathbf{r}_6 - \mathbf{r}_1) \times (\mathbf{r}_5 - \mathbf{r}_1)$ , and so on. Note that  $\mathbf{M}_{1562} \neq \mathbf{r}_{1562} \times \mathbf{S}_{1562}$ . The expression,  $\mathbf{r}_{1562} \times \mathbf{S}_{1562}$ , is not well-defined for computing area moment. In contrast, Eq. (22) is well-defined. To see these, let  $\mathbf{r}_\diamond$ ,  $\mathbf{r}_\Delta$ ,  $\mathbf{S}_\diamond$  and  $\mathbf{S}_\Delta$  be  $\mathbf{r}_{1562}$ ,  $\mathbf{r}_{165}$ ,  $|\mathbf{S}_{1562}|\mathbf{n}$  and  $|\mathbf{S}_{165}|\mathbf{n}$ , respectively. After simple algebraic manipulation, one

The other conceptually different way is to use  $\mathbf{S}_\Delta$  always; that is, to regard the hexahedral cell as dodecahedron or to divide the hexahedral cell into tetrahedron. Then, instead of Eq. (14), one will obtain

$$\sum_{cell} \mathbf{S}_\Delta = 0 \quad (28)$$

for either dodecahedron or tetrahedron in addition to Eq. (24). The resulting metric terms will preserve the free stream. The use of the tetrahedral cell allows the most compact and consistent metric formulation. Note, however, that the use of the tetrahedron results in unstructured-grid formulations.

## Finite-Difference Formulation

### Geometric Identities in the Finite-Difference Formulation

The analysis of the FD method can be simplified with the aid of the above discussion of the FV method. The FD formulation has to be derived from the integral form, Eq. (1). Again from Ref. 1, the differential form for Eq. (1) can be written with a generalized coordinate transformation,

$$\mathbf{r} = \mathbf{r}(\xi, \eta, \zeta, \tau), \quad t = \tau \quad (29)$$

as follows:

$$\hat{Q}_\tau + \hat{E}_\xi + \hat{F}_\eta + \hat{G}_\zeta = 0 \quad (30)$$

where subscripts indicate partial differentiation,

$$\hat{Q} = QV, \quad \hat{E} = \mathbf{S}^\xi \cdot \mathbf{F}, \quad \hat{F} = \mathbf{S}^\eta \cdot \mathbf{F}, \quad \hat{G} = \mathbf{S}^\zeta \cdot \mathbf{F}$$

and where

$$\mathbf{S}^\xi = \mathbf{r}_\eta \times \mathbf{r}_\zeta, \quad \mathbf{S}^\eta = \mathbf{r}_\zeta \times \mathbf{r}_\xi, \quad \mathbf{S}^\zeta = \mathbf{r}_\xi \times \mathbf{r}_\eta \quad (31)$$

and

$$V = \mathbf{r}_\xi \cdot \mathbf{r}_\eta \times \mathbf{r}_\zeta \quad (32)$$

where  $\delta$  denotes the difference operator. After scaling by one-fourth to adjust the area from double-sized to regular cell, the first component of the above expression can be written as

$$\frac{\xi_x}{J} = (\mu_\zeta \delta_\eta y)(\mu_\eta \delta_\zeta z) - (\mu_\zeta \delta_\eta z)(\mu_\eta \delta_\zeta y) \quad (38)$$

where  $\mu$  denotes the arithmetic averaging operator. Thus, Eq. (12) is equivalent to the consistently differenced metrics in Ref. 3 that are based on the averaging procedure so as to satisfy the differential chain rules numerically.

The main discrepancy between the FV and FD formulations appears in the definition of cell volume. The cell volume defined by Eq. (13) is different from the one defined by the discretized form of Eq. (32) because the FD method does not use the cell concept. Nevertheless, Eq. (13) can be applied to the FD method with a scaling factor of one-eighth instead of Eq. (32). Then, the FV space metrics on the double-sized cell become identical to the FD ones.

The FD time-metric evaluation is also considered from the FV point of view. It is easily found that the time-metric evaluation, Eq. (34), will not maintain the free stream even with the use of the free-stream capturing metrics, Eqs. (11) or (12), in case of a rotating frame because of Eq. (23). Also, it can be shown that such inconsistent time metrics do not satisfy GCL. The discretized form of GCL can be written as

$$\Delta V = \Delta \tau [\delta_\xi (\mathbf{S}^\xi \cdot \mathbf{r}_\tau) + \delta_\eta (\mathbf{S}^\eta \cdot \mathbf{r}_\tau) + \delta_\zeta (\mathbf{S}^\zeta \cdot \mathbf{r}_\tau)] \quad (39)$$

Let the grid move in the rigid rotation, that is,  $V_\tau = 0$  and  $\mathbf{r}_\tau = \boldsymbol{\Omega} \times \mathbf{r}$ . Then the left-hand side of Eq. (39) is zero. But the right-hand side results in  $\delta_\xi (\mathbf{r} \times \mathbf{S}^\xi) + \delta_\eta (\mathbf{r} \times \mathbf{S}^\eta) + \delta_\zeta (\mathbf{r} \times \mathbf{S}^\zeta) \neq 0$  (Eq. (23) appears again). This indicates that the use of the GCL condition, Eq. (39), for computing  $\Delta V$  can be erroneous. In other words, the GCL condition, Eq. (39), is necessary to preserve the free stream, but not sufficient to construct consistent metrics in space and time.

It is easily found that the time integration of Eq. (39) from  $t_1$  to  $t_2$  results in Eq. (18) and thus both equations are equivalent. Therefore, the consistent time metrics

## References

- <sup>1</sup>Vinokur, M., "An Analysis of Finite-Difference and Finite-Volume Formulations of Conservation Laws," *J. Comput. Phys.*, Vol. 81, No. 1, Mar. 1989, pp. 1-52.
- <sup>2</sup>Pulliam, T. H. and Steger, J. L., "On Implicit Finite-Difference Simulations of Three-Dimensional Flow," AIAA Paper 78-10, Jan. 1978.
- <sup>3</sup>Chaderjian, N. M., "Transonic Navier-Stokes Wing Solutions Using a Zonal Approach," NASA TM-88248, Apr. 1986.
- <sup>4</sup>Buning, P. G., Chiu, I. T., Obayashi, S., Rizk, Y. M., and Steger, J. L., "Numerical Simulation of the Integrated Space Shuttle Vehicle in Ascent," AIAA Paper 88-4359-CP, Aug. 1988.
- <sup>5</sup>Srinivasan, G. R., Baeder, J. D., Obayashi, S., and McCroskey, W. J., "Flowfield of a Lifting Hovering Rotor – A Navier-Stokes Simulation," Paper No. I.3.5, 16th European Rotorcraft Forum, Glasgow, Scotland, U.K., Sept. 18-21, 1990.
- <sup>6</sup>Chen, C. L. and McCroskey, W. J., "Numerical Simulation of Helicopter Multi-Bladed Rotor Flow," AIAA Paper 88-0046, Jan. 1988.
- <sup>7</sup>Thomas, P. D. and Lombard, C. K., "Geometric Conservation Law and Its Application to Flow Computations on Moving Grids," *AIAA J.*, Vol. 17, No. 10, Oct. 1979, pp. 1030-1037.

## Report Documentation Page

1. Report No. NASA CR-177572		2. Government Accession No.		3. Recipient's Catalog No.	
4. Title and Subtitle  Free-Stream Capturing in Fluid Conservation Law for Moving Coordinates in Three Dimensions				5. Report Date  January 1991	
				6. Performing Organization Code	
7. Author(s)  Shigeru Obayashi				8. Performing Organization Report No.  A-91022	
				10. Work Unit No.  505-60	
9. Performing Organization Name and Address  MCAT Institute San Jose, CA 95127				11. Contract or Grant No.  NCC2-605	
				13. Type of Report and Period Covered  Contractor Report	
12. Sponsoring Agency Name and Address  National Aeronautics and Space Administration Washington, DC 20546-0001				14. Sponsoring Agency Code	
15. Supplementary Notes  Point of Contact: Peter M. Goorjian, Ames Research Center, MS 258-1 Moffett Field, CA 94035-1000 (415) 604-5547 or FTS 464-5547					
16. Abstract  This report summarizes the free-stream capturing technique for both the finite-volume (FV) and finite-difference (FD) framework. For an arbitrary motion of the grid, the FV analysis shows that volumes swept by all six surfaces of the cell have to be computed correctly. This means that the free-stream capturing time-metric terms should be calculated not only from a surface vector of a cell at a single time level, but also from a volume swept by the cell surface in space and time. The FV free-stream capturing formulation is applicable to the FD formulation by proper translation from an FV cell to an FD mesh.					
17. Key Words (Suggested by Author(s))  Conservation law, Moving coordinates, Finite-volume method, Finite-difference method			18. Distribution Statement  Unclassified-Unlimited  Subject Category - 02		
19. Security Classif. (of this report)  Unclassified		20. Security Classif. (of this page)  Unclassified		21. No. of Pages  16	
				22. Price  A02	





# **APPENDIX E**



71A 32024

**AIAA-91-1109**

**UNSTEADY SHOCK-VORTEX INTERACTION ON  
A FLEXIBLE DELTA WING**

S. Obayashi and G. P. Guruswamy  
NASA Ames Research Center  
Moffett Field, CA

**32nd AIAA/ASME/ASCE/AHS/ASC Structures,  
Structural Dynamics and Materials Conference  
April 8-10, 1991/Baltimore, MD**

# Unsteady Shock-Vortex Interaction on a Flexible Delta Wing

Shigeru Obayashi\* and Guru P. Guruswamy\*\*

NASA Ames Research Center, 258-1

Moffett Field, California 94035

## Abstract

Unsteady Navier-Stokes computations have been carried out for simulating transonic flows over a clipped delta wing undergoing oscillatory and ramp motions, including flexibility. The implicit upwind algorithm has been validated by comparing the solutions with experimental data for the oscillatory pitching motion cases. The numerical and experimental results agree well at moderate angles of attack, where a leading-edge vortex develops. The ramp motion cases have demonstrated the effects of unsteadiness of the flow field and structural flexibility on the wing responses. For the  $10^\circ$  ramp motion, a vortex breakdown is observed. The interaction with the shock wave plays an essential role in the process of the breakdown observed in the present calculation.

## Introduction

In the last decade, there have been extensive developments in computational fluid dynamics toward the prediction of the three-dimensional flow field about complex geometries at moderate and high angles of attack. Among the characteristics of flows over aircraft, the behavior of the flow over delta wings is of strong interest for high-speed aircraft because of the nonlinear lift increase due to the leading-edge vortex. Effects

of flexibility can further influence the nature of flows on such wings. Steady-state flow problems associated with delta wings have been widely investigated computationally (for example, Refs. 1 to 3). Several advanced studies have also been performed for unsteady vortical calculations at subsonic and supersonic Mach numbers. For example, Ref. 4 presented a conical flow computation on a rigid wing and Ref. 5 presented a subsonic three-dimensional computation on a flexible wing, both involving vortical flows.

Numerical methods can play an important role in complementing expensive wind tunnel tests, particularly in the area of aeroelasticity. An aeroelastic wind tunnel experiment is an order of magnitude more expensive than a similar rigid-body experiment involving only aerodynamics. By complementing the experiments with numerical simulations, the overall cost of the development of aircraft can be considerably reduced. Thus development of a numerical method is desired for simulating aeroelastic phenomenon. To accurately compute aeroelastic phenomenon it is necessary to solve the unsteady Euler/Navier-Stokes equations simultaneously with the structural equations of motion.

Recently a code, ENSAERO, was developed to compute aeroelastic responses by simultaneously integrating the Euler/Navier-Stokes equations and the modal structural equations of motion using aeroelastically adaptive dynamic grids.<sup>6,7</sup> An upwind algorithm was implemented into the code and the resulting code was successfully applied to compute transonic flows over a typical fighter-type wing undergoing oscillatory motion.<sup>8</sup>

The purpose of this paper is to examine the capability of the present numerical method by simulating unsteady transonic flows on a clipped delta wing, which contain a leading-edge separation. So far, unsteady

\*Research Scientist, MCAT Institute, member AIAA.

\*\*Research Scientist, AIAA Associate Fellow.

Copyright © 1991 by the American Institute of Aeronautics and Astronautics, Inc. No copyright is asserted in the United States under Title 17, U.S. Code. The U.S. Government has a royalty-free license to exercise all rights under the copyright claimed herein for Governmental purposes. All other rights are reserved by the copyright owner.

physics more closely than the coordinate upwind methods. The computed results confirmed the higher resolution of the present algorithm over the central-difference method as well as over other upwind methods.<sup>13</sup> In this work, the streamwise upwind algorithm is applied to compute the inviscid cell-interface fluxes. A second-order central-difference evaluation is applied to the viscous term. The complete algorithm can be found in Refs. 8 and 13.

An implicit method is used for the time integration because the computational efficiency of the method is critical for expensive unsteady viscous calculations. The method chosen here is the LU-ADI (lower-upper factored, alternating direction implicit) method<sup>14</sup> because it requires only scalar bidiagonal matrix inversions. See Refs. 15 and 16 for additional details.

### Aeroelastic Equations of Motion

The governing aeroelastic equations of motion of a flexible wing are solved using the Rayleigh-Ritz method. In this method, the resulting aeroelastic displacements at any time are expressed as a function of a finite set of assumed modes. The contribution of each assumed mode to the total motion is derived by Lagrange's equation. Furthermore, it is assumed that the deformation of the continuous wing structure can be represented by deflections at a set of discrete points. This assumption facilitates the use of discrete structural data, such as the modal vector, the modal stiffness matrix, and the modal mass matrix. These can be generated from a finite-element analysis or from experimental influence-coefficient measurements. In this study, the finite-element method is used to obtain the modal data.

It is assumed that the deformed shape of the wing can be represented by a set of discrete displacements at selected nodes. From the modal analysis, the displacement vector  $\{d\}$  can be expressed as

$$\{d\} = [\phi]\{q\} \quad (4)$$

where  $[\phi]$  is the modal matrix and  $\{q\}$  is the generalized displacement vector. The final matrix form of the aeroelastic equations of motion is

$$[M]\{\ddot{q}\} + [G]\{\dot{q}\} + [K]\{q\} = \{F\} \quad (5)$$

where  $[M]$ ,  $[G]$ , and  $[K]$  are modal mass, damping, and stiffness matrices, respectively.  $\{F\}$  is the aerodynamic force vector defined as  $(\frac{1}{2})\rho U_\infty^2 [\phi]^T [A] \{\Delta C_p\}$  and  $[A]$  is the diagonal area matrix of the aerodynamic control points.

The aeroelastic equation of motion (Eq. (5)) is solved by a numerical integration technique based on the linear acceleration method.<sup>17</sup>

### Aeroelastic Configuration Adaptive Grids

One of the major deficiencies in computational aerodynamics using the Navier-Stokes equations lies in the area of grid generation. For steady flows, the advanced techniques such as zonal grids<sup>18</sup> are being used. Grid generation techniques for aeroelastic calculations, which involve moving components, are in early stages of development. In Ref. 7, aeroelastic configuration adaptive dynamic grids were successfully used for computing time-accurate aeroelastic responses of swept wings. In this work, a similar technique is used.

### Results

Numerical schemes used for flow calculations in aeroelasticity must guarantee the correct calculation of amplitude and phase of unsteady pressures. To verify the accuracy of the present code for simulating the complicated flow field containing a leading-edge vortex and a shock wave, test cases are chosen from the experiment on a clipped delta wing undergoing prescribed pitching motion.<sup>9</sup> Since the experiment was conducted using a Freon test medium, the ratio of specific heats  $\gamma$  is set to 1.135 in the following computations.

#### Steady Pressures

Steady-state calculations have been performed to examine the validity of the numerical procedure and the computational grid. The model planform geometry is shown in Fig. 1. The wing has a leading-edge sweep angle of 50.4° and a 6%-thick circular-arc airfoil section. The lines, A, B, and C, indicate the spanwise locations of the pressure orifices in the experiment. Figure 2 shows the grid generated algebraically in the C-H topology. The  $\xi$ ,  $\eta$ , and  $\zeta$  coordinates represent the chordwise, spanwise, and normal (to the wing surface) directions, respectively. The grid contains  $151 \times 25 \times 34$  points.

The present grid is fairly coarse compared with the grids used in the typical steady-state computations.<sup>1-3</sup> The number of grid points was determined to compromise the accuracy and the total computational time. Unsteady computations require more computational time than the steady-state computations. With the present grid, a typical unsteady case can be computed within 5 hr by using a Cray YMP computer with a single processor. (The code requires about 19  $\mu\text{sec}$  per

at the 68% section in Fig. 8 shows no effect due to the leading-edge vortex, it is inconsistent with the other data. Overall, the numerical results show fairly good agreement with the experimental data. Again, the difference of shock motion due to the Mach numbers and the difference of the vortex motion due to the angles of attack are successfully captured.

Figure 12 shows the comparison of unsteady pressures between the modified and unmodified Baldwin-Lomax turbulence models for the fourth case (Fig. 11). To see the difference clearly, the unsteady pressures are plotted in the magnitude and phase angle here. The improvements due to the modification of the turbulence model are seen in both magnitude and phase angle where the leading-edge vortex exists. The results also confirm that the present grid has reasonable resolution for the present unsteady flow fields, even though the grid is fairly coarse. Further improvements and grid refinements will be needed to achieve a better agreement at the outboard sections.

## Rigid and Flexible Ramp Motions

In maneuvering, aircraft often undergo rapid ramp motions. During such motions, flow unsteadiness and wing flexibility play important roles. In this section, the applicability of the present development to computing such flow fields is demonstrated.

Computations are performed for rigid and flexible wings in ramp motion. Structural properties of the wing were selected to represent a typical fighter wing. Figure 13 shows the mode shapes and the frequencies of the first four normal modes for the clipped delta wing used in the following computations. The dynamic pressure is set to be 1.0 psi. Test cases consider 4 and 10° ramp motions for both rigid and flexible wings.

### 4° Ramp Motion

Figure 14 shows the comparisons of the sectional lift responses between the rigid and flexible wings at  $M_\infty = 0.9$  and  $Re_c = 15 \times 10^6$  for the wing ramping up to 4° with a pitch rate of  $A = 0.04$ . The pitch rate  $A$  is defined as  $\dot{\alpha}c/U_\infty$ . The data are plotted at 34%, 54%, 68%, and 90% semispan sections. The unsteady computations are started from the converged steady-state solution at 0° angle of attack.

In the rigid-wing case, the lift responses at the inboard sections settle down quickly after the ramp motion stops, and the flow approaches the steady-state values. At the 90% section, however, the lift continues to increase for a short period after the ramp motion stops. This corresponds to the movement of the leading-edge vortex as indicated in the corresponding

pressure history shown in Fig. 15. In Fig. 15, the pressure distributions are plotted every 100 time steps. The ramp motion ends at 600 time steps ( $t \approx 0.04$  sec), which corresponds to the sixth plot from the bottom. At the 90% section in Fig. 15d, a leading-edge vortex is formed and lifts off from the wing surface. This results in the increase and then a decrease of the sectional lift shown in Fig. 14. At the other inboard sections in Fig. 15, the pressure distributions become similar to those in Fig. 6, i.e., the leading-edge vortex remains without interacting with the shock wave. Thus, the corresponding sectional lift stays nearly steady with minor fluctuations due to the movement of the vortex, as seen in Fig. 15a.

In contrast to the rigid-wing case, Fig. 14 shows that the sectional lift responses of the flexible wing are oscillatory. The primary effect of the flexibility is the reduction of the lift at most of the spanwise sections due to the reduced angles of attack. Figure 16 shows the corresponding pressure history plots. The plots in Fig. 16c and d show the shedding of the leading-edge vortex in comparison to the plots of the rigid wing in Fig. 15c and d. In addition, Fig. 14 shows that the 90% sectional lift response of the flexible wing has the low-frequency primary oscillation perturbed by a high-frequency vortex shedding. The low-frequency primary oscillation corresponds to the structural oscillation as shown later. The high-frequency perturbation corresponds to the shedding of the vortex that can be seen in the pressure plots of Fig. 16d.

Computations (not shown) were also carried out for the flexible-wing ramping from 0° to 3° and from 0° to 5° at the same pitch rate as the 4° case. The 4° case shows the largest high-frequency perturbation. In the 3° case, the vortex is not strong enough to disturb the lift response. The vortex shedding is found only at the 90% section. In the 5° case, the vortex lifts off from the wing surface so that the structural oscillation does not cause the perturbation seen at the lower angles of attack. The 10° case discussed in the next section does not show the perturbation either.

An aeroelastic reduction of the local angle of attack results in a delay of the lift increase of the flexible wing for a short period after the ramp motion stops (about  $0.04 < t < 0.11$  in Fig. 14). Figure 17 shows the instantaneous density contour plots of the 90% spanwise section at 800 time steps ( $t \approx 0.05$  sec). The contours are plotted at intervals of 0.02 (bold line indicates free-stream density, 1.0). The plots show that the leading-edge vortex on the flexible wing is weaker than that on the rigid wing. Figure 18 shows the corresponding deformation of the flexible wing. The solid lines indicate the corresponding surface of the rigid wing. The actual displacement of the leading edge at the wing tip

## Concluding Remarks

In this paper, a computational procedure for computing the unsteady transonic flows associated with the leading-edge vortex on a clipped delta wing, including flexibility, has been presented. The procedure is based on a time-accurate computational method combined with the use of aeroelastically adaptive dynamic grids. The flow is modeled using the Navier-Stokes equations. The flow equations are coupled with the structural equations to account for the flexibility. The numerical procedure has been verified through the comparisons with the experiment for the unsteady pitching cases on the rigid clipped delta wing. The main flow structures are successfully captured using a fairly coarse grid.

The ramp motion cases have demonstrated the effects of unsteadiness of the flow field and flexibility of the wing. The primary effect of the flexibility is the reduction of the lift due to the deformation of the wing. Interaction of the leading-edge vortex with the shock wave has significant effects on the wing responses. For the 4° ramp motion, the vortex shedding occurs at the wing tip due to the flexibility. For the 10° ramp motion, a possible vortex breakdown is observed. The interaction with the shock wave plays an essential role in the process of the breakdown observed in the present calculation. A further grid-refinement study will assess the validity of the present observations.

## References

- <sup>1</sup>Fujii, K. and Schiff, L. B., "Numerical Simulation of Vortical Flows over a Strake-Delta Wing," *AIAA Journal*, Vol. 27, No. 9, Sept. 1990, pp. 1153-1162.
- <sup>2</sup>Taylor, S. L., Kjølgaard, S. O., Weston, R. P., Thomas, J. L., and Sellers, W. L., III, "Experimental and Computational Study of the Subsonic Flow About a 75° Swept Delta Wing," *AIAA Paper 87-2425*, Aug. 1987.
- <sup>3</sup>Ekaterinaris, J. A. and Schiff, L. B., "Numerical Simulation of the Effects of Variation of Angle of Attack and Sweep Angle on Vortex Breakdown over Delta Wings," *AIAA Paper 90-3000-CP*, Aug. 1990.
- <sup>4</sup>Kandil, O. A. and Chuang, H. A., "Computation of Vortex-Dominated Flow for a Delta Wing Undergoing Pitching Oscillation," *AIAA Journal*, Vol. 28, No. 9, Sept. 1990, pp. 1589-1595.
- <sup>5</sup>Guruswamy, G. P., "Vortical Flow Computations on Swept Flexible Wings Using Navier-Stokes Equations," *AIAA Paper 89-1183*, Apr. 1989.
- <sup>6</sup>Guruswamy, G. P., "Unsteady Aerodynamic and Aeroelastic Calculations of Wings Using Euler Equations," *AIAA Journal*, Vol. 28, Mar. 1990, pp. 461-469.
- <sup>7</sup>Guruswamy, G. P., "Navier-Stokes Computations on Swept-Tapered Wings, Including Flexibility," *AIAA Paper 90-1152*, Apr. 1990.
- <sup>8</sup>Obayashi, S., Guruswamy, G. P., and Goorjian, P. M., "Application of a Streamwise Upwind Algorithm for Unsteady Transonic Computations over Oscillating Wings," *AIAA Paper 90-3103*, Aug. 1990.
- <sup>9</sup>Hess, R. W., Cazier, F. W., Jr., and Wynne, E. C., "Steady and Unsteady Transonic Pressure Measurements on a Clipped Delta Wing for Pitching and Control-Surface Oscillations," *NASA TP-2594*, Oct. 1986.
- <sup>10</sup>Baldwin, B. S. and Lomax, H., "Thin-Layer Approximation and Algebraic Model for Separated Turbulent Flows," *AIAA Paper 78-257*, Jan. 1978.
- <sup>11</sup>Degani, D. and Schiff, L. B., "Computations of Turbulence Supersonic Flows Around Pointed Bodies Having Crossflow Separation," *J. Computational Physics*, Vol. 66, No. 1, Sept. 1986, pp. 173-196.
- <sup>12</sup>Goorjian, P. M., "A New Algorithm for the Navier-Stokes Equations Applied to Transonic Flows Over Wing," *AIAA Paper 87-1121-CP*, June 1987.
- <sup>13</sup>Obayashi, S. and Goorjian, P. M., "Improvements and Applications of a Streamwise Upwind Algorithm," *AIAA Paper 89-1957-CP*, June 1989.
- <sup>14</sup>Obayashi, S., "Numerical Simulation of Under-expanded Plumes Using Upwind Algorithms," *AIAA Paper 88-4360-CP*, Aug. 1988.
- <sup>15</sup>Obayashi, S., Goorjian, P. M., and Guruswamy, G. P., "Extension of a Streamwise Upwind Algorithm to a Moving Grid System," *NASA TM-102800*, Apr. 1990.
- <sup>16</sup>Obayashi, S., Matsushima, K., Fujii, K., and Kuwahara, K., "Improvements in Efficiency and Reliability for Navier-Stokes Computations Using the LU-ADI Factorization Algorithm," *AIAA Paper 86-0338*, Jan. 1986.
- <sup>17</sup>Guruswamy, P. and Yang, T. Y., "Aeroelastic Time Response Analysis of Thin Airfoils by Transonic Code LTRAN2," *Computers and Fluids*, Vol. 9, No. 4, Dec. 1980, pp. 409-425.
- <sup>18</sup>Flores, J., "Simulation of Transonic Viscous Wing and Wing-Fuselage Flows Using Zonal Methods," *NASA TM-89421*, Mar. 1987.
- <sup>19</sup>Tu, E. L., "Navier-Stokes Simulation of a Close-Coupled Canard-Wing-Body Configuration," *AIAA Paper 91-0070*, Jan. 1991.

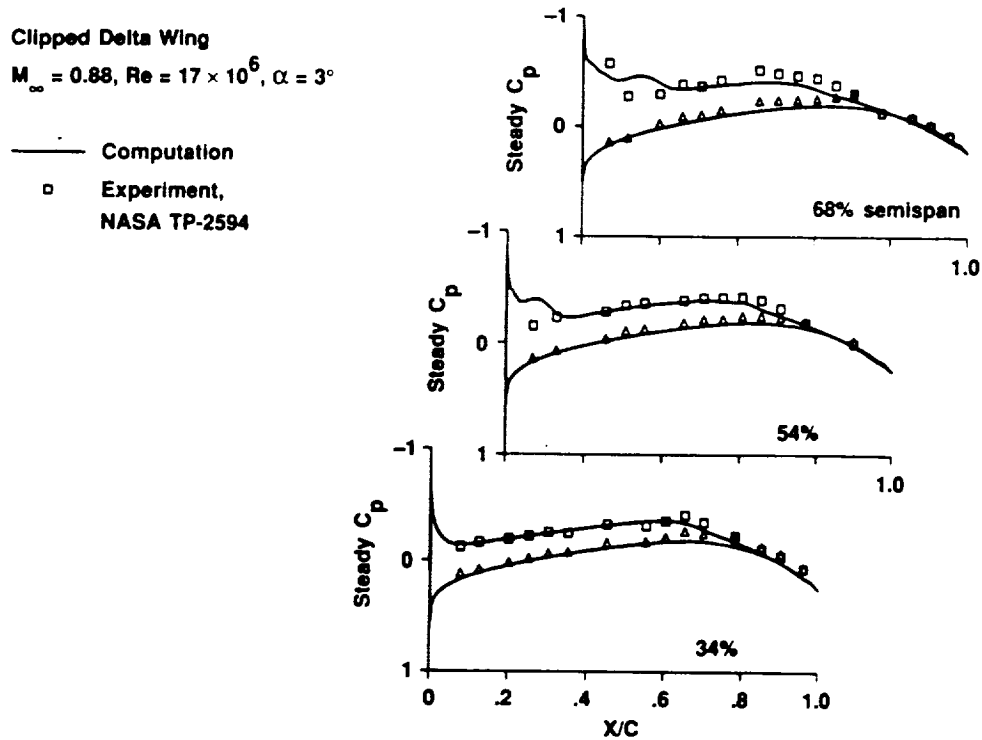


Fig. 3 Comparison of steady pressures with experiment,  $M_\infty = 0.88$ ,  $\alpha = 3.04$ ,  $Re_c = 17.2 \times 10^6$ .

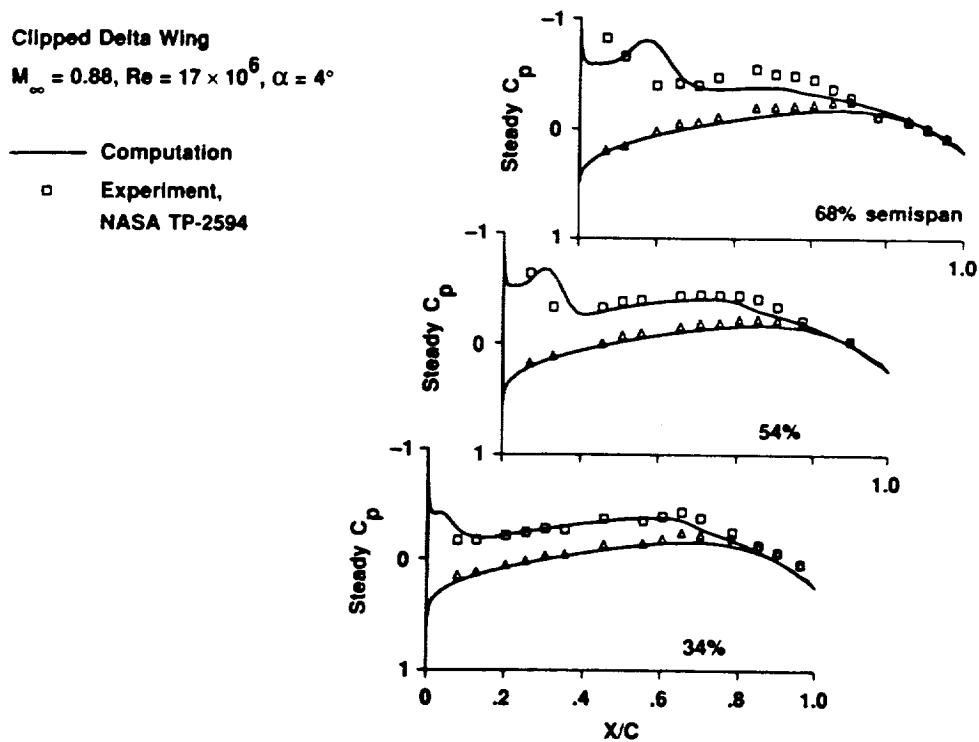


Fig. 4 Comparison of steady pressures with experiment,  $M_\infty = 0.88$ ,  $\alpha = 4.03$ ,  $Re_c = 17.3 \times 10^6$ .

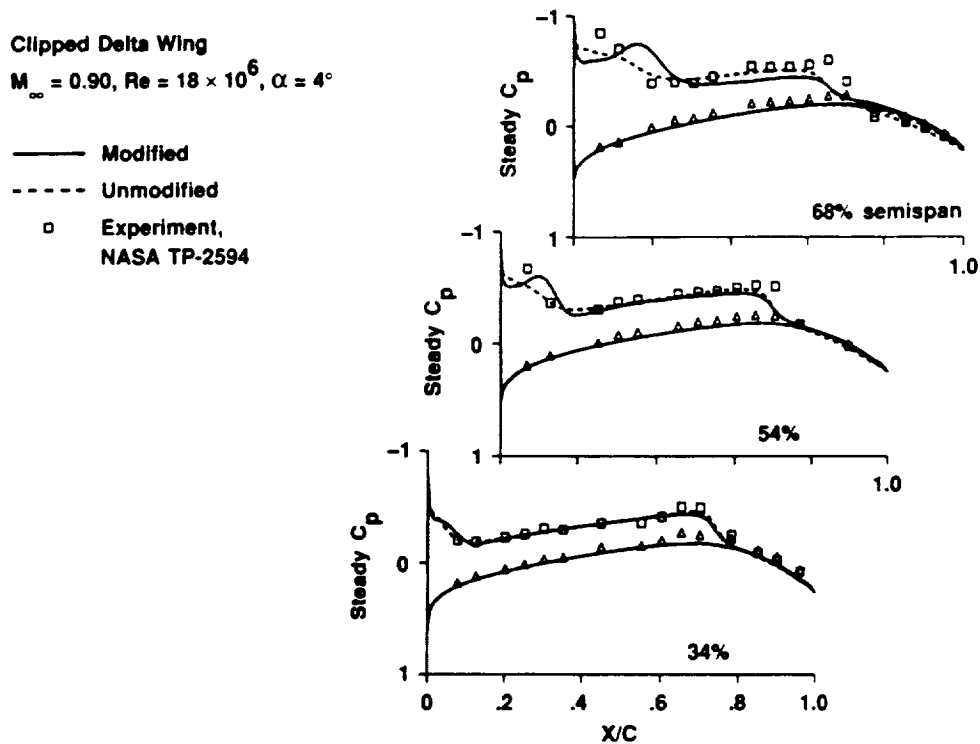


Fig. 7 Comparison of steady pressures between the standard and modified Baldwin-Lomax turbulence models,  $M_\infty = 0.90$ ,  $\alpha = 3.97$ ,  $Re_c = 17.6 \times 10^6$ .

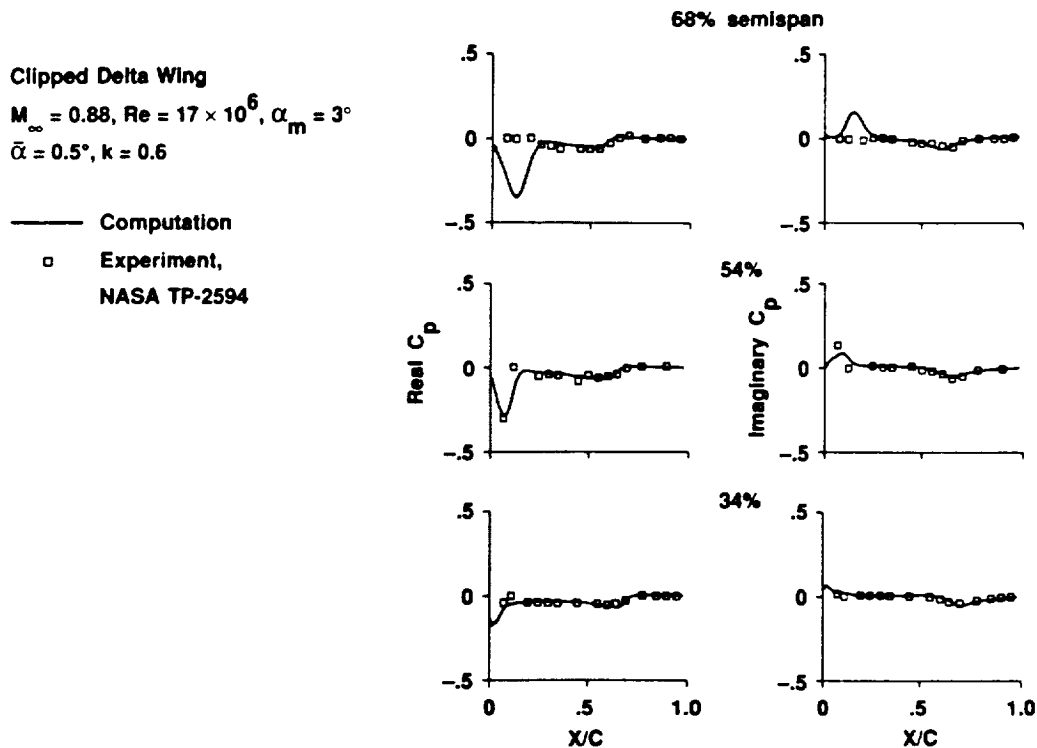


Fig. 8 Comparison of unsteady pressures with experiment,  $M_\infty = 0.88$ ,  $\alpha_m = 3.04$ ,  $\bar{\alpha} = 0.48$ ,  $Re_c = 17.2 \times 10^6$ ,  $k = 0.6059$ .



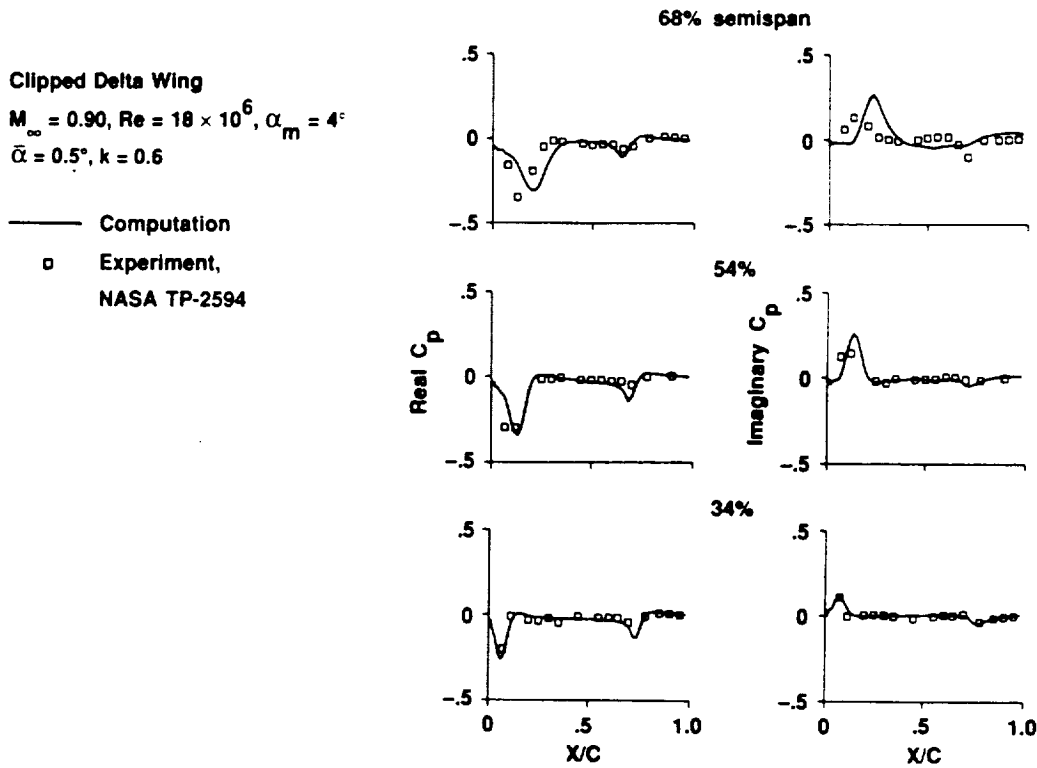


Fig. 11 Comparison of unsteady pressures with experiment,  $M_\infty = 0.90$ ,  $\alpha_m = 3.97$ ,  $\bar{\alpha} = 0.46$ ,  $Re_c = 17.6 \times 10^6$ ,  $k = 0.5919$ .

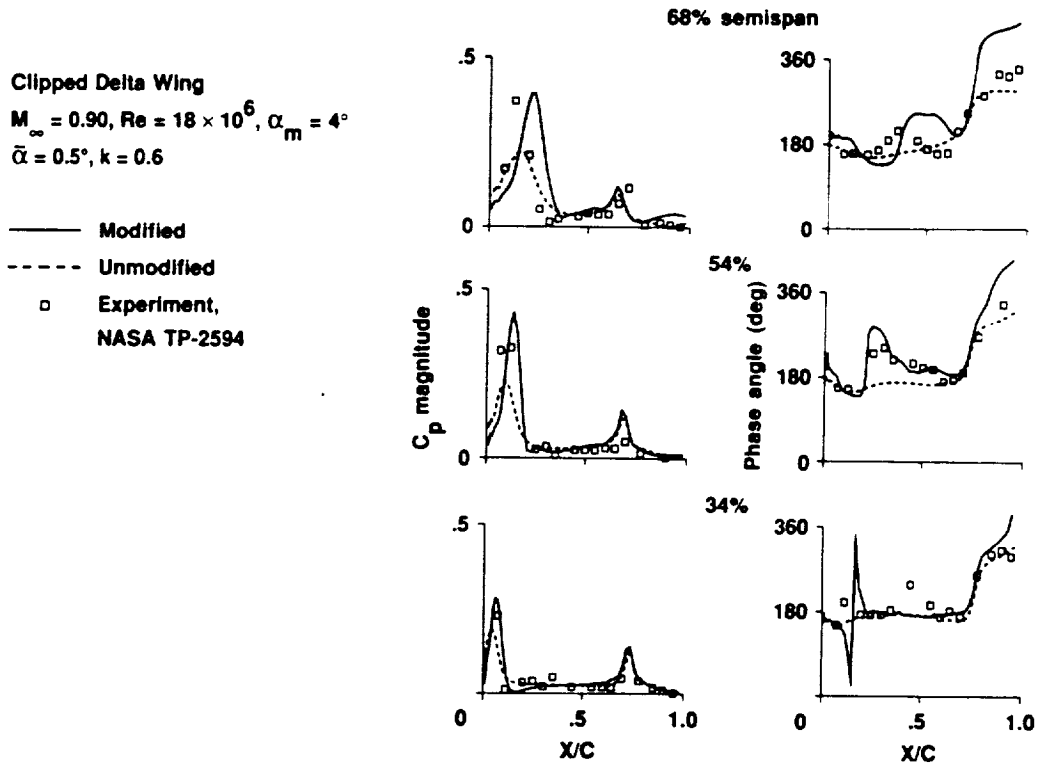


Fig. 12 Comparison of unsteady pressures between the standard and modified Baldwin-Lomax turbulence models,  $M_\infty = 0.90$ ,  $\alpha_m = 3.97$ ,  $\bar{\alpha} = 0.46$ ,  $Re_c = 17.6 \times 10^6$ ,  $k = 0.5919$ .

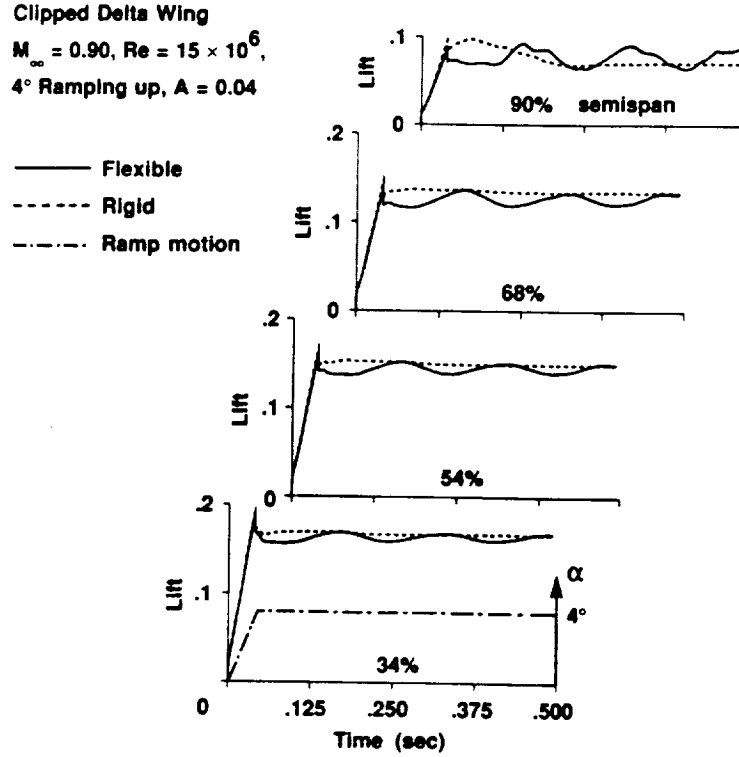


Fig. 14 Comparison of sectional lift responses between rigid and flexible wings,  $M_\infty = 0.90$ ,  $4^\circ$  ramping up,  $Re_c = 15.0 \times 10^6$ ,  $A = 0.04$ .

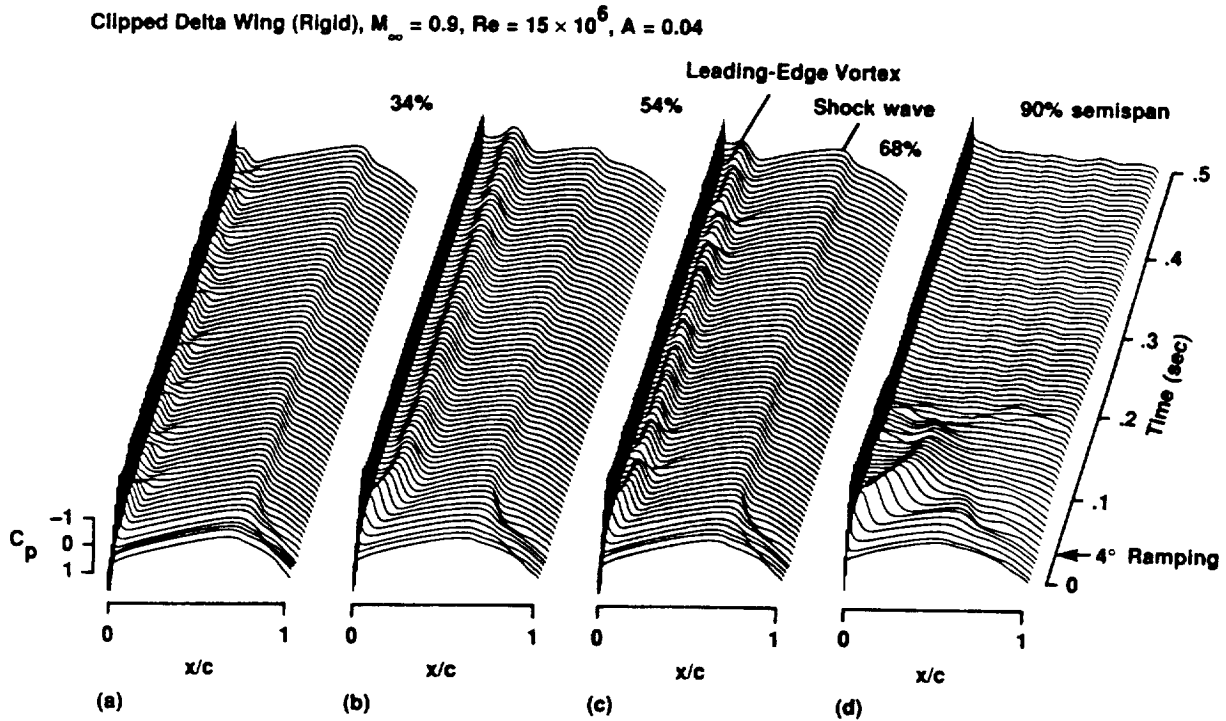


Fig. 15 Unsteady upper surface pressure responses of rigid wing,  $M_\infty = 0.90$ ,  $4^\circ$  ramping up,  $Re_c = 15.0 \times 10^6$ ,  $A = 0.04$ . a) 34% section; b) 54% section; c) 68% section; d) 90% section.

# Clipped Delta Wing

$M_\infty = 0.9$ ,  $Re = 15 \times 10^6$ ,

$4^\circ$  Ramping,  $A = 0.04$ ,  $t = 0.053$  sec

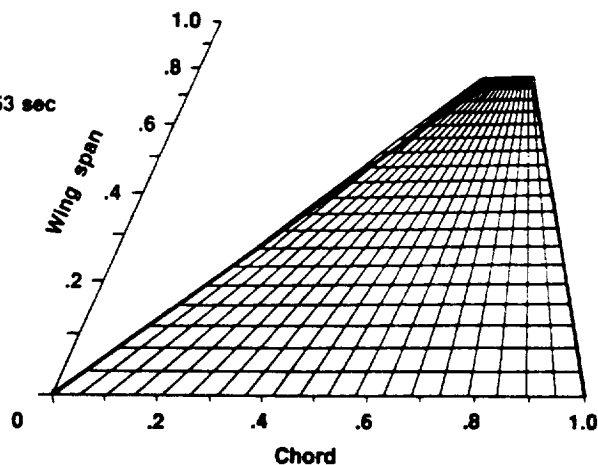


Fig. 18 Deformation of flexible wing in comparison to rigid wing at 800 time steps,  $M_\infty = 0.90$ ,  $4^\circ$  ramping up,  $Re_c = 15.0 \times 10^6$ ,  $A = 0.04$ .

# Clipped Delta Wing (Flexible)

$M_\infty = 0.9$ ,  $Re = 15 \times 10^6$ ,

$4^\circ$  Ramping,  $A = 0.04$

— Lift  
 - -  $\alpha$   
 (Rigid + Elastic)

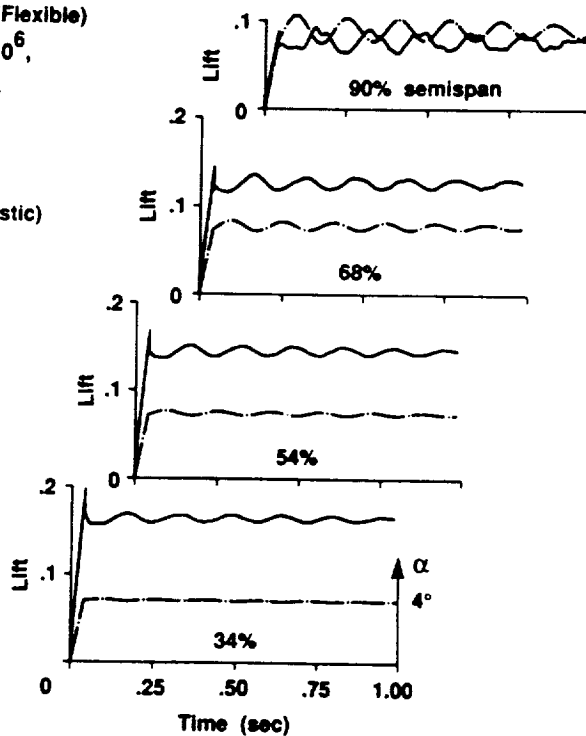


Fig. 19 Responses of sectional lift and elastic angle of attack for flexible wing,  $M_\infty = 0.90$ ,  $4^\circ$  ramping up,  $Re_c = 15.0 \times 10^6$ ,  $A = 0.04$ .

Clipped Delta Wing (Rigid),  $M_\infty = 0.9$ ,  $Re = 15 \times 10^6$ ,  $A = 0.04$

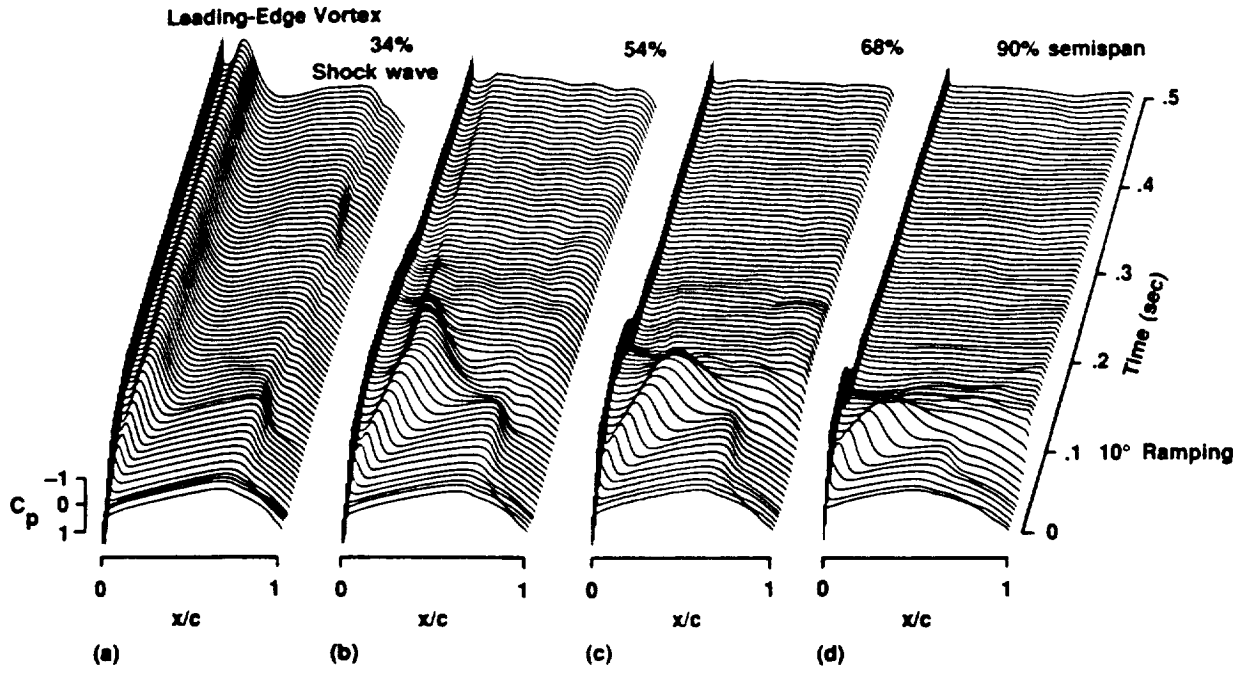


Fig. 23 Unsteady upper surface pressure responses of rigid wing,  $M_\infty = 0.90$ ,  $10^\circ$  ramping up,  $Re_c = 15.0 \times 10^6$ ,  $A = 0.04$ . a) 34% section; b) 54% section; c) 68% section; d) 90% section.

Clipped Delta Wing (Flexible),  $M_\infty = 0.9$ ,  $Re = 15 \times 10^6$ ,  $A = 0.04$

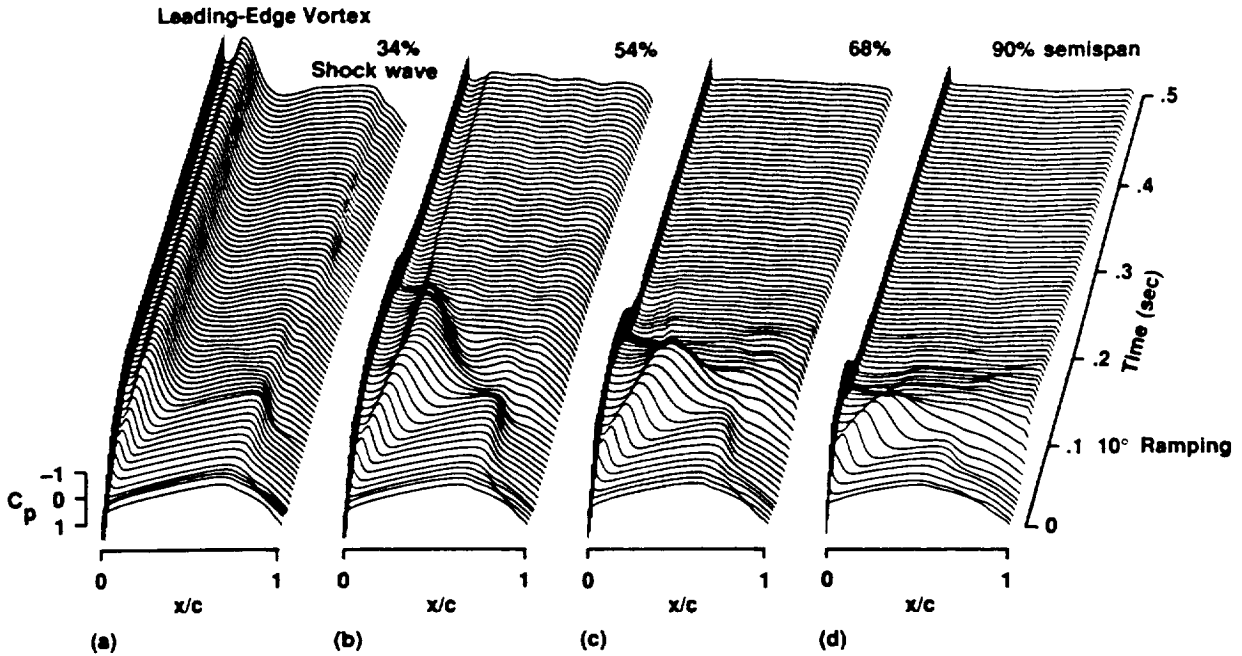


Fig. 24 Unsteady upper surface pressure responses of flexible wing,  $M_\infty = 0.90$ ,  $10^\circ$  ramping up,  $Re_c = 15.0 \times 10^6$ ,  $A = 0.04$ . a) 34% section; b) 54% section; c) 68% section; d) 90% section.

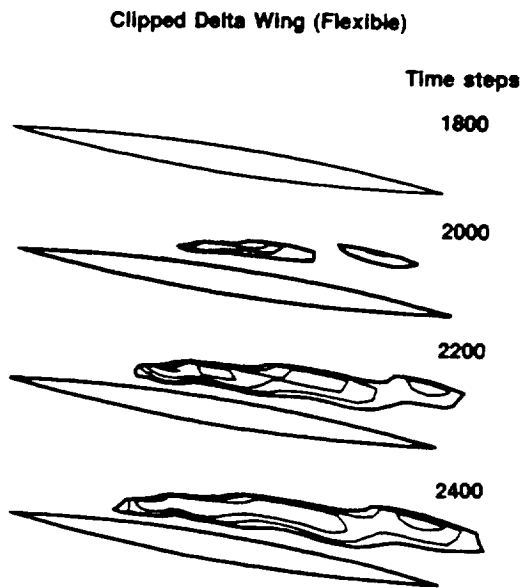


Fig. 26 Instantaneous negative- $u$ -velocity contour plots at 68% semispan section,  $M_\infty = 0.90$ ,  $10^\circ$  ramping up,  $Re_c = 15.0 \times 10^6$ ,  $A = 0.04$ .

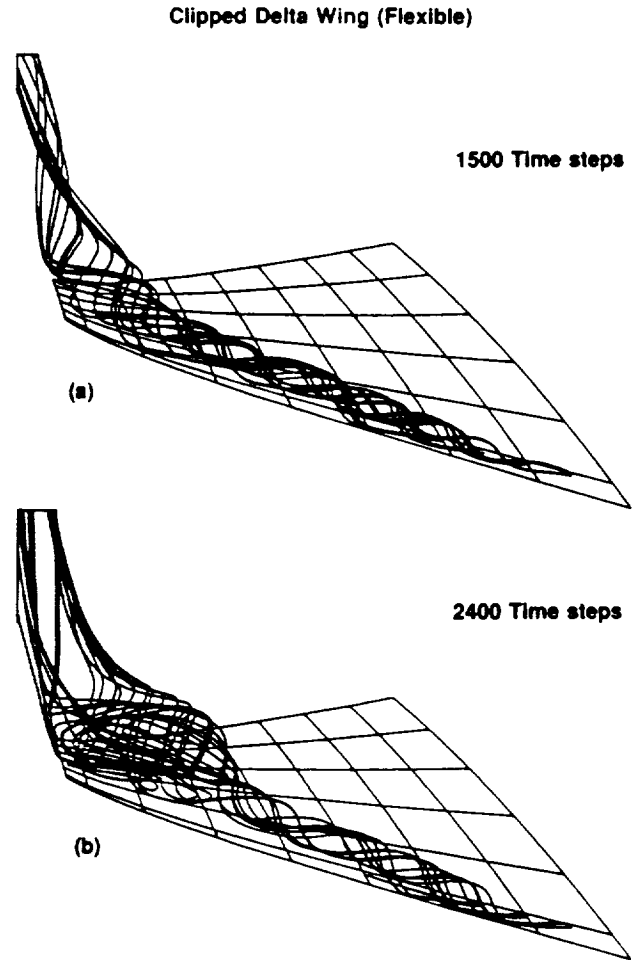


Fig. 27 Streamline pattern over the upper surface of flexible wing,  $M_\infty = 0.90$ ,  $10^\circ$  ramping up,  $Re_c = 15.0 \times 10^6$ ,  $A = 0.04$ . a) 1500 time steps; b) 2400 time steps.

# APPENDIX F

0111

Abstract of a proposed paper for the presentation at AIAA Atmospheric Flight Mechanics Conference, August 19-21, 1991, New Orleans, Louisiana.

## Unsteady Navier-Stokes Computations on a Wing-Body Configuration in Ramp Motions

Shigeru Obayashi,\* Guru P. Guruswamy\*\* and Eugene L. Tu\*\*\*

NASA Ames Research Center, Moffett Field, California

### Summary

Unsteady Navier-Stokes computations have been carried out for simulating transonic flows over a wing-body configuration undergoing prescribed pitching and ramp motions, including flexible modes. The unsteady Navier-Stokes code used in this study has been validated by comparing the numerical solutions with experimental data for pitching motion cases about wings in transonic flow-fields from a small angle-of-attack to a relatively high angle-of-attack, where a leading-edge vortex develops. In this work, the method has been extended to handle wing-body configurations. Steady and unsteady results at transonic Mach numbers will be shown for the wing-body model and comparisons are made with the available experimental and numerical data. The ramp motion covers angles of attack where a vortex breakdown is observed in the experiment. The effects of unsteadiness will be discussed in detail.

### Introduction

In the last two decades, there have been extensive developments in computational aerodynamics, which constitutes a major part of the general area of computa-

---

\* Research Scientist, MCAT Institute, San Jose, California. Member AIAA.

\*\* Research Scientist. AIAA Associate Fellow.

\*\*\* Research Scientist. Member AIAA.

viscosity is carefully evaluated to capture the leading-edge separation.

In this abstract, the steady and unsteady results for the ramp motion are presented for the rigid wing-body model. In addition, code validation results from previous studies<sup>2,4,7</sup> are shown here. Further detailed results including forced flexibility will be presented in the full paper. All of the results to be presented in the full paper are new and have not been submitted to any other meetings or publications.

### **Governing Aerodynamic Equations and Approximations**

The governing equations used in this study is the thin-layer Navier-Stokes equations written in conservation-law form in a generalized body-conforming curvilinear coordinate system. Several numerical schemes have been developed to solve these equations. The present code has two different schemes; the central-difference and upwind schemes. Detailed formulas will be given in the full paper.

The viscosity coefficient in the thin-layer viscous term is computed as the sum of  $\mu_l + \mu_t$  where the laminar viscosity,  $\mu_l$ , is taken from the freestream laminar viscosity, assumed to be constant for transonic flows. The turbulent viscosity,  $\mu_t$ , is originally evaluated by the Baldwin-Lomax algebraic eddy-viscosity model.<sup>10</sup> The modification of the turbulence model originally developed for crossflow separation by Degani and Schiff<sup>11</sup> is applied to evaluate the turbulent viscosity of flow-fields containing a leading-edge vortex. However, for this geometry, this modification has difficulty in locating the boundary-layer edge, especially at low angles-of-attack where the leading-edge vortex lies near the wing surface. Thus, the Johnson-King model<sup>12,13</sup> is also applied for comparison and the results will be discussed in the full paper.

## **Results**

### **1. Code Calibration on Wings**



pressures at the outboard section show that the peaks near the leading edge in the computed profiles are located more downstream than in the experimental data. This indicates that the computed leading-edge vortex location is more inboard than was found in the experiment. This discrepancy between computed and measured data is widely seen in other numerical results including Ref. 15. Although the Degani-Schiff correction<sup>11</sup> is used here, there are problems such as the lack of transition modeling in the Baldwin-Lomax model. Nevertheless, the computed results show good qualitative agreement with the experiment even for the unsteady cases.

Next, the ramp motion of the same clipped delta wing was investigated.<sup>4</sup> Figure 2 shows pressure histories at  $M_\infty = 0.9$  for the wing ramping up to 5 degrees with a pitch rate of  $A = 0.01$ . The pitch rate,  $A$ , is defined as  $\dot{\alpha}c/U_\infty$ . The unsteady computations are started from the converged steady-state solution at  $\alpha = 0.0^\circ$ . The results show the dynamics of vortex and shock development. The corresponding sectional lift curves are plotted in Fig. 3. Stall can be seen at 90% semispan section.

The third example is a comparison of ramp motions of a typical fighter wing with different pitch rates.<sup>2</sup> It is well known that the dynamic lift for airfoils can be increased by increasing pitch rates. Because dynamic lift is an unsteady phenomenon, and is associated with the presence of vortices, it is important to model it accurately. In this computation, the Mach number is subsonic and the angle-of-attack varies from  $0^\circ$  to  $30^\circ$ . Figure 4 shows contour plots of the velocity magnitude at various spanwise locations. The plots indicate the presence of the leading-edge vortex.

To see the effects of increasing pitch rates, computations were made for the three pitch rates of 0.025, 0.05 and 0.1. The unsteady sectional lift coefficients are plotted against time in Fig. 5. For all three pitch rates, the stall occurs at the wing-tip before it occurs at the root section. These plots confirm the increase in the dynamic lift at higher pitch rates for this fighter wing case except for the inboard sections.

Results in this section verify the validation of the present code to accurately

of-attack is shown in Fig. 7. Comparisons with the experimental data are given at wing-span stations of 35, 45, 55 and 85%. The results generally show good agreement except at the 85% wing-span where the discrepancies are most likely due to the modeling of the wing-tip. Since detailed geometry data was unavailable for the wing-tip of the wind-tunnel model, the tip is assumed to be rounded in this study.

At the inboard spanwise locations, the suction peaks due to the leading-edge vortex appear to be slightly underpredicted. This discrepancy becomes worse as angle-of-attack increases. However, grid refinement was found to improve the prediction significantly.<sup>7</sup> In addition, the turbulence model affects the formation of the leading-edge vortex. The performance of the Johnson-King model<sup>12,13</sup> is currently being investigated. In the full paper, these additional numerical issues will be addressed.

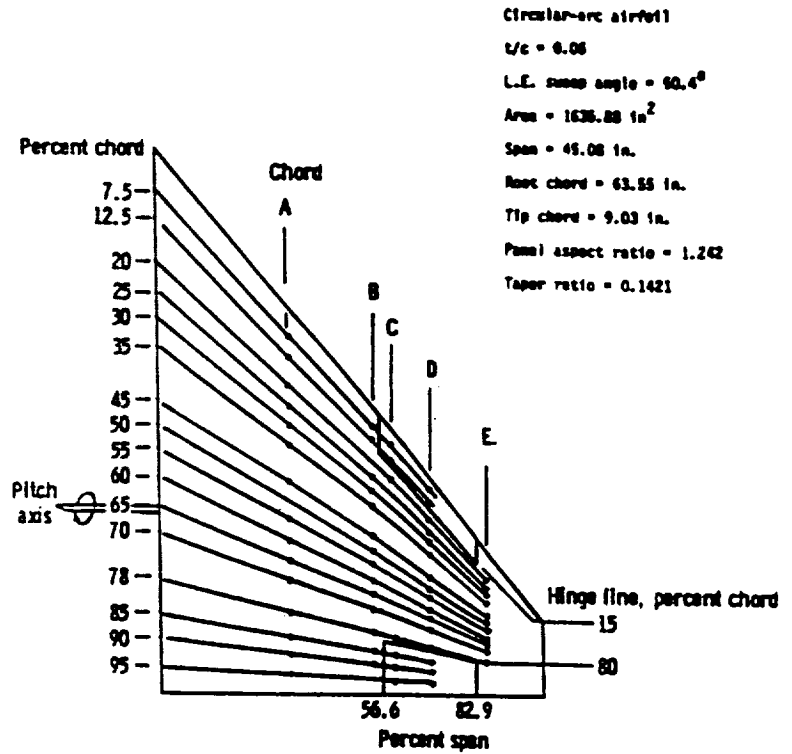
### c. Unsteady Results

In this abstract, the ramp motion case is shown as a sample result. The computation was started from the steady-state solution at  $4.09^\circ$  angle-of-attack. Then, the model was ramped up 5 degrees with a pitch rate of  $A = 0.1$ . After the angle-of-attack reached  $9.09^\circ$ , the model was held stationary. Figure 8 shows the grid and pressure contours on the upper surface of the wing-body model at various angles-of-attack. Figures 8.a thru 8.d show the grid, pressure contours at  $\alpha = 4.09^\circ$  (steady-state),  $\alpha = 7.59^\circ$  (unsteady) and  $\alpha = 9.09^\circ$  (unsteady at maximum  $\alpha$ ), respectively.

Figure 9 shows a time history of pressure responses at the 35, 55 and 85% wing span locations. The plots show the dynamics of the leading-edge vortex development. The corresponding total lift curve during ramp-up is plotted in Fig. 10. The dynamic lift increase is clearly shown. After reaching the maximum angle-of-attack, the lift coefficient is observed to decrease slowly to the steady-state value. A complete ramp motion from 0 to 12 degrees is being performed and will be presented in the full paper. In the steady-state results,<sup>7,16</sup> a vortex breakdown was observed at about  $12^\circ$  angle-of-attack. The effects of unsteadiness will be discussed in detail.

## References

- <sup>1</sup> Guruswamy, G. P., "Time-Accurate Unsteady Aerodynamic and Aeroelastic Calculations of Wings Using Euler Equations," AIAA Paper 88-2281, Williamsburg, VA, April 1988.
- <sup>2</sup> Guruswamy, G. P., "Navier-Stokes Computations on Swept-Tapered Wings, Including Flexibility," AIAA-90-1152, Long Beach, CA, April 1990.
- <sup>3</sup> Obayashi, S., Guruswamy, G. P. and Goorjian, P. M., "Application of a Streamwise Upwind Algorithm for Unsteady Transonic Computations over Oscillating Wings," AIAA Paper 90-3103, Portland, OR, August 1990.
- <sup>4</sup> Obayashi, S. and Guruswamy, G. P., "Transonic Flow Simulation on a Clipped Delta Wing with Pitching and Ramp Motions, Including Flexibility," submitted to 32nd AIAA/ASME/ASCE/AHS/ASC Structures, Structural Dynamics and Materials Conference, Baltimore, MD, April 8-10, 1991.
- <sup>5</sup> Flores, J. "Simulation of Transonic Viscous Wing and Wing-Fuselage Flows Using Zonal Methods," NASA TM 89421, Mar. 1987.
- <sup>6</sup> Chaderjian, N. M. and Guruswamy, G. P., "Unsteady Transonic Navier-Stokes Computations for an Oscillating Wing Using Single and Multiple Zones," AIAA Paper 90-0313, Reno, NV, January 1990.
- <sup>7</sup> Tu, E. L., "Navier-Stokes Simulation of a Close-Coupled Canard-Wing-Body Configuration," AIAA Paper 91-0070, to be presented at Reno, NV, January 1991.
- <sup>8</sup> Guruswamy, G. P. and Goorjian, P. M., "Unsteady Transonic Flow Simulation on a Full-Span-Wing-Body Configuration," AIAA Journal, Vol. 26, No. 12, December 1988, pp. 1450-1456.
- <sup>9</sup> Batina, J. T., "Unsteady Euler Algorithm with Unstructured Dynamic Mesh for Complex-Aircraft Aeroelastic Analysis," AIAA Paper 89-1189, April 1989.
- <sup>10</sup> Baldwin, B. S. and Lomax, H., "Thin-Layer Approximation and Algebraic Model



Planform geometry of clipped delta wing.

— Present

$\triangle$ ,  $\square$  Exp., Ref. 14.

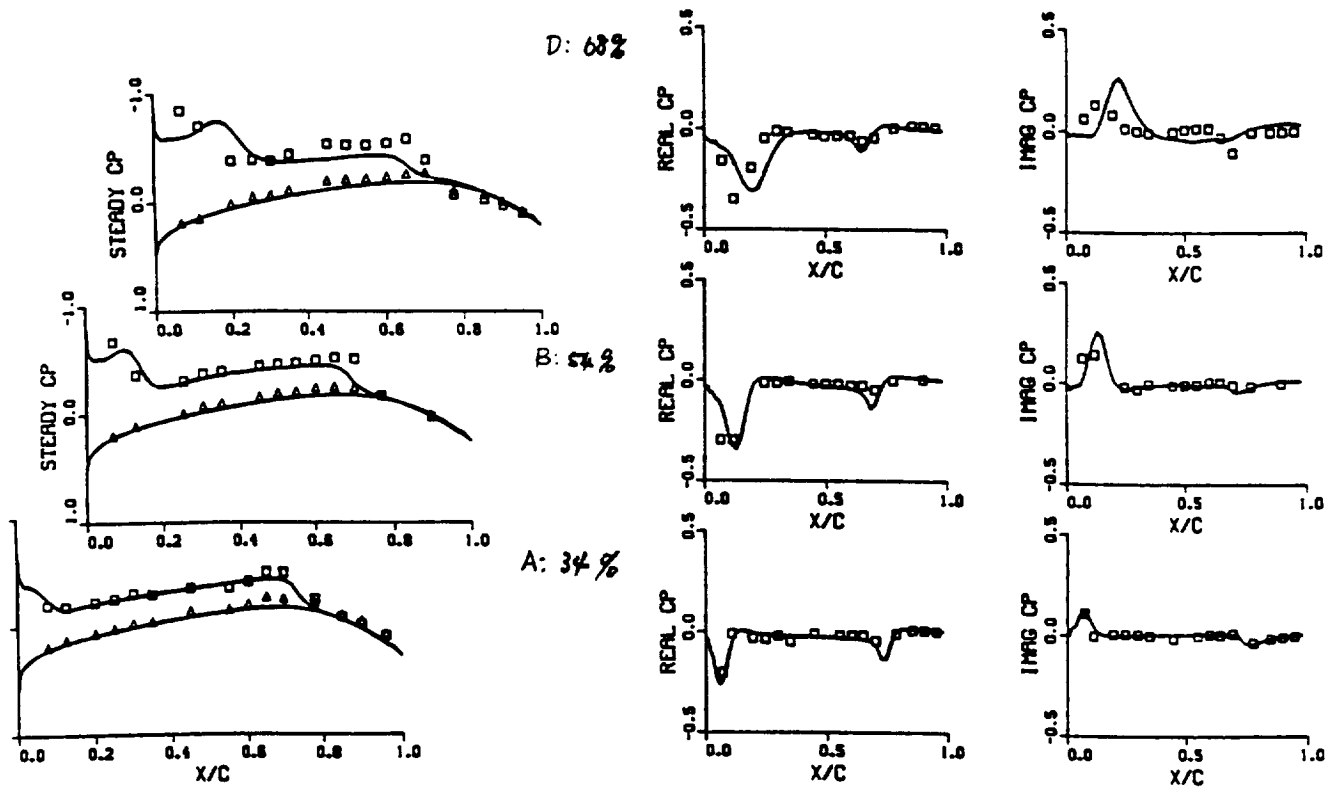


Fig. 1 Comparison of steady and unsteady pressures with experiment;  $M_\infty = 0.90$ ,  
 $\alpha_m = 3.97$ ,  $\bar{\alpha} = 0.46$ ,  $Re_c = 17.6 \times 10^6$ ,  $k = 0.5919$ .

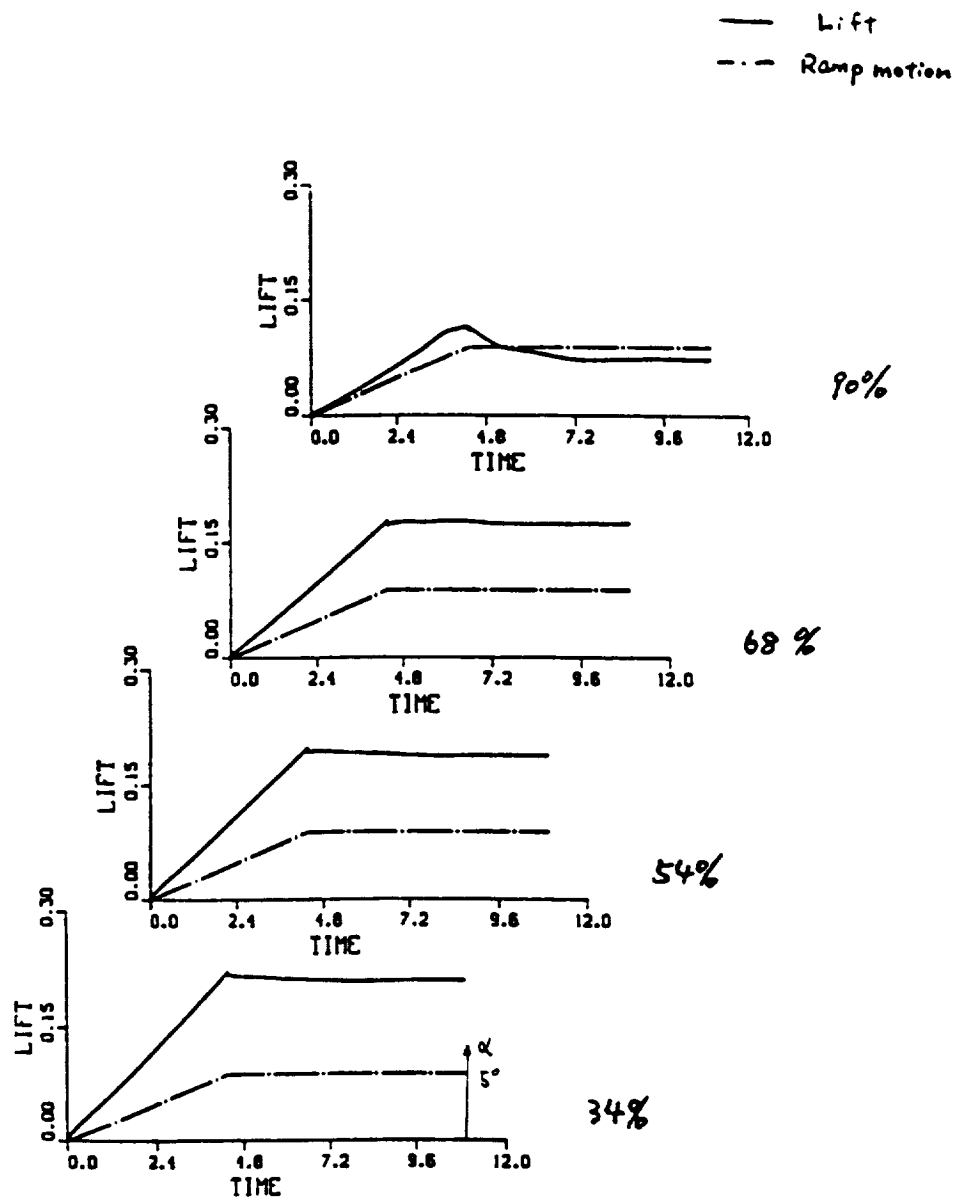


Fig. 3 Sectional lift responses in ramp motion;  $M_\infty = 0.90$ ,  $0^\circ \sim 5^\circ$  ramping up,  $Re_c = 15.0 \times 10^6$ ,  $A = 0.01$ .

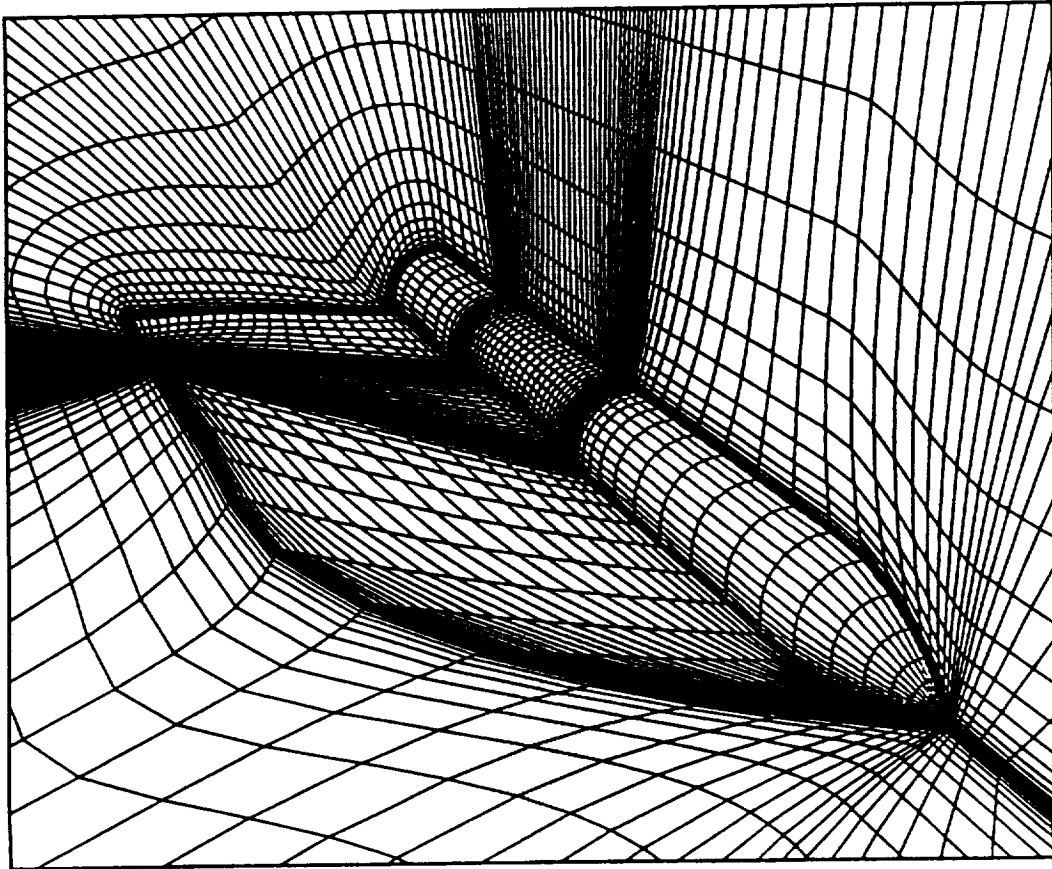
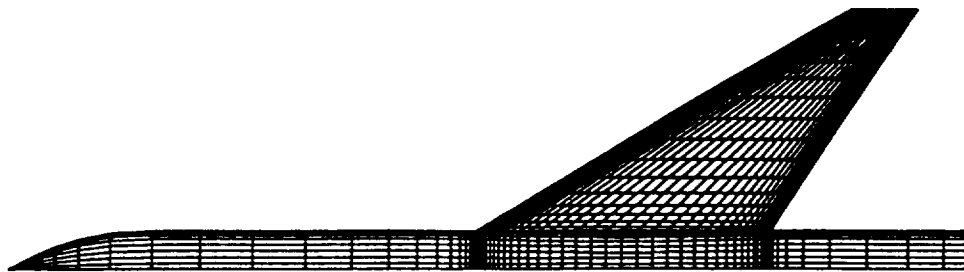
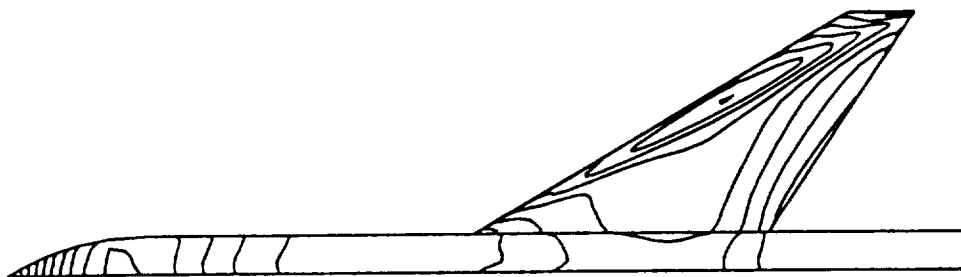


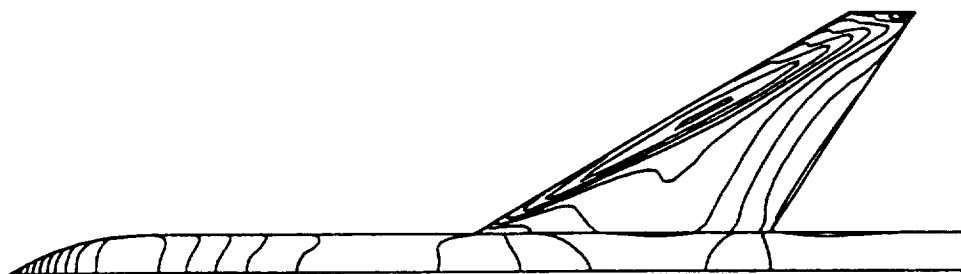
Fig. 6 Close-up view of wing-body grid.



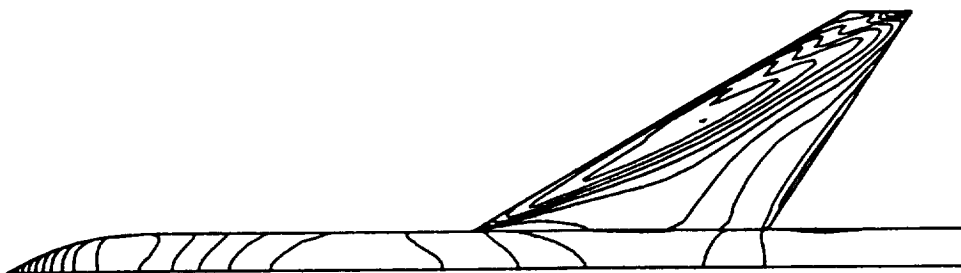
a) Grid.



b)  $\alpha = 4.09^\circ$ , steady-state solution.



c)  $\alpha = 7.59^\circ$ , unsteady solution with pitch rate 0.1.



d)  $\alpha = 9.09^\circ$ , unsteady solution at maximum angle-of-attack with pitch rate 0.1.

Fig. 8 Instantaneous pressure contours on the upper surface of a wing-body model in ramp motion from  $4^\circ$  to  $9^\circ$  angle-of-attack.

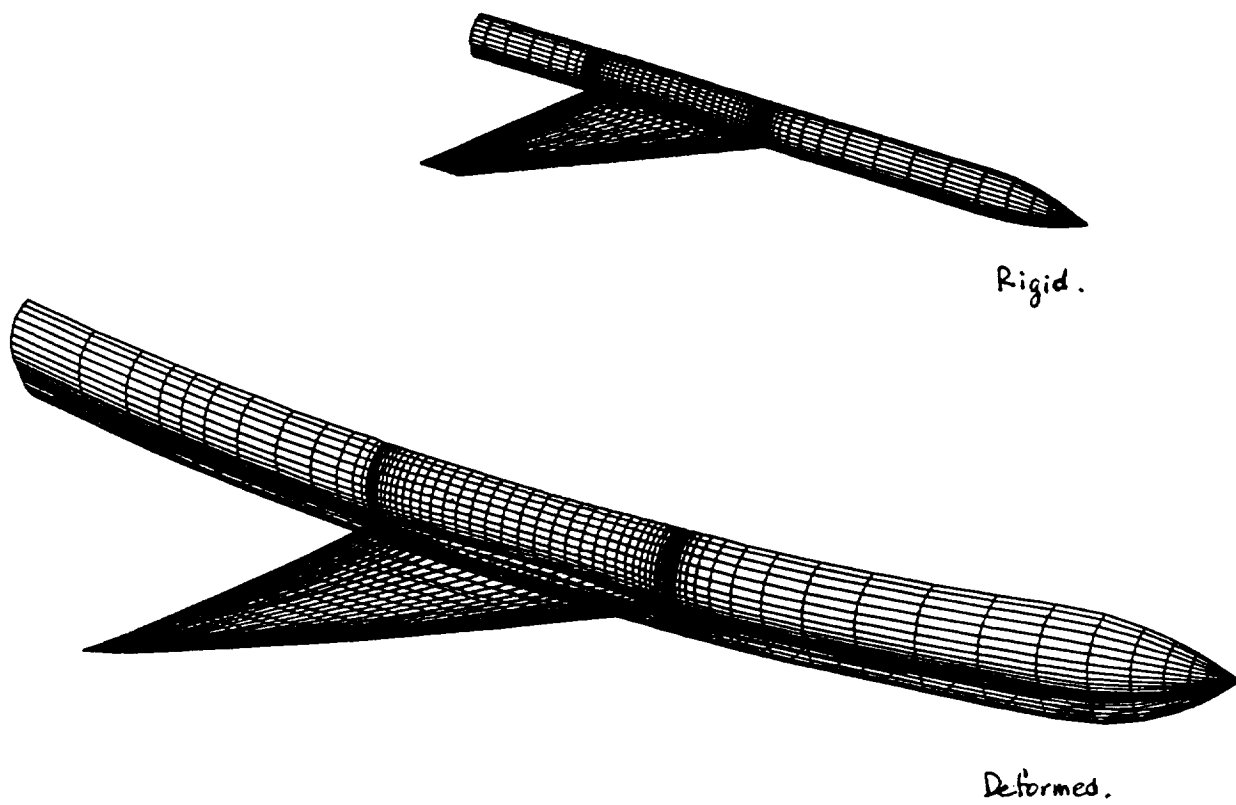


Fig. 11 Example of forced elasticity of a wing-body model.